AN ABSTRACT OF THE THESIS OF

Ira Jewell for the degree of Master of Science in Electrical and Computer Engineering presented on May 25, 2010.

Title: Electrical Characterization of Thermally Reduced Graphite Oxide

Abstract approved:

____

Albrecht Jander   Pallavi Dhagat

This thesis describes the transport properties observed in thermally treated graphite oxide (GO), which holds promise as an economical route to obtaining graphene. Graphene is a material consisting of a single atomic plane of carbon atoms and was first isolated as recently as 2004. Several isolation techniques have been investigated, including mechanical exfoliation, chemical vapor deposition, and the reduction (by various methods) of chemically synthesized graphite oxide.

Two fundamental questions are pursued in this work. The first is concerned with the maximum electrical conductivity that can be achieved in atomically thin reduced graphite oxide samples (rGO). As produced, GO is insulating and of little use electronically. By heating and exposure to reducing atmospheres, however, the conductivity can be increased. Through the lithographic definition and fabrication of four-point contact structures atop microscopic samples of GO, the resistance of the sample can be monitored in situ as the reduction process takes place.

It was discovered that the resistance of few-layer GO could be decreased by an order of magnitude when heated to 200 °C and subsequently cooled back to room temperature in forming gas. Final resistivities were on the order of 0.5 Ω-cm. An ambipolar field effect was observed in the thermally treated samples, with resistance decreasing by up to 16 % under a substrate bias of ±20 V. Mobilites were inferred to

be on the order of 0.1 cm^2/V-s. It was also found that the presence of forming gas during reduction decreased the resistance of the GO samples by roughly one half.

The second question that this work begins to answer is concerned with the distance that electrons can travel in such thermally-reduced GO before spin-randomizing scattering. The answer can be elucidated with the aid of magnetoresistance measurements using ferromagnetic contacts to inject a spin-polarized current through the sample. The observation of the magnetoresistive effect with the contacts separated by a certain distance can be taken as evidence of a spin coherence length in the material of at least that distance.

Though this experiment has not yet been carried out, progress has been made toward its possibility; specifically in the fabrication and characterization of independently switchable magnetic contacts. By exploiting magnetic shape anisotropy, contact pairs have been fabricated and demonstrated to differ in magnetic coercivity by up to 8 Oe.

©Copyright by Ira Jewell
May 25, 2010
All Rights Reserved

Electrical Characterization of Thermally Reduced Graphite Oxide

by
Ira Jewell

A THESIS

submitted to

Oregon State University

in partial fulfillment of
the requirements for the
degree of

Master of Science

Presented May 25, 2010
Commencement June 2011

Master of Science thesis of Ira Jewell presented on May 25, 2010

APPROVED:

Major Professor, representing Electrical and Computer Engineering

---

Director of the School of Electrical Engineering and Computer Science

---

Dean of the Graduate School

I understand that my thesis will become part of the permanent collection of Oregon State University libraries. My signature below authorizes release of my thesis to any reader upon request.

Ira Jewell, Author

ACKNOWLEDGEMENTS

I would like to thank my advisors, Dr. Albrecht Jander and Dr. Pallavi Dhagat, for their help and support in this project and also for introducing me to the world of the magnetician. Thank you to Dr. John Conley, Chien-Chih “James” Huang, and Sean Smith (AKA Team Graphene) for many thought-provoking insights and practical assistances. A very special thanks to both Chris Tasker and Manfred Dittrich for teaching me more than I could learn in any classroom, and also to Eric Sundholm, Rick Presley, and Richard Schaffer for introducing me to the practices and protocols of the cleanroom. Thank you to all members of the magnetics group (past and present) who have sat through countless weekly presentations leading up to this result. A special thanks has to go to Ram Ravichandran and Bill Cowell (long live the SSA). Thank you to Josh Kevek for helping with AFM imaging and Wei Wang for helping with Raman spectroscopy. Last but not least thank you to Cindy Dauer, my best friend and life partner and without whose support, none of this would have been possible.

TABLE OF CONTENTS

Page

1 Introduction 1

2 Literature Review...4

2.1 Properties of Graphene...4

2.1.1 Physical Description..4

2.1.2 Interesting Quantum Mechanical Properties 7

2.1.3 Interesting Macroscopic Properties..12

2.1.4 Bilayer Graphene and Graphene Nanoribbons...18

2.2 Isolation Techniques 20

2.2.1 Micro-Mechanical Cleavage 21

2.2.2 Graphitization of SiC 22

2.2.3 Reduction of Graphite Oxide 23

2.2.4 Chemical Vapor Deposition 27

2.2.5 Graphene from Carbon Nanotubes...29

2.3 Identification Techniques...30

2.3.1 Optical Microscopy 30

2.3.2 Atomic Force Microscopy...31

2.3.3 Raman Spectroscopy 33

2.4 Applications 36

2.4.1 Transistors 37

2.4.2 Sensors 42

2.4.3 Transparent Conductors (Solar Cells) 45

TABLE OF CONTENTS (Continued)

Page

2.4.4 Supercapacitors 48

2.4.5 Other Applications 49

3 Materials and Methods..51

3.1 Fabrication Techniques..51

3.1.1 Thermal Oxidation of Silicon..51

3.1.2 GO Solution Processing 53

3.1.3 Photolithography 55

3.1.4 Thin Film Deposition 60

3.1.5 Wirebonding..64

3.2 Characterization Techniques..69

3.2.1 ProboStat™ and Tube Furnace 69

3.2.2 Semiconductor Parameter Analyzer (SPA)..72

3.2.3 BH Looper..74

4 Experimental Results 77

4.1 Thermal Reduction of Graphite Oxide..77

4.1.1 In Situ Resistance Measurements..77

4.1.2 Atomic Force Microscopy and Raman Spectroscopy 82

4.1.3 Substrate Bias..83

4.2 Independently Switchable Magnetic Contacts..86

5 Discussion of Results and Conclusion..89

TABLE OF CONTENTS (Continued)

Page

6 Recommendations for Future Work...92

Bibliography 95

Appendix A: Procedure for Synthesis of Graphite Oxide 103

Appendix B: Fabrication of Chrome Masks Using DWL 104

Appendix C: Operational Procedure for Thermal Evaporator...................................106

Appendix D: Operational Procedure for Sputter Tool 108

LIST OF FIGURES

Figure Page

1. Real-space lattice description of graphene. 5
2. Reciprocal-space description of graphene 6
3. Calculated structure of single-layer graphene.. 7
4. Hall effect in three-dimensional material 9
5. Integer quantum Hall effect 11
6. Half-integer quantum Hall effect in graphene. 12
7. Contrast of graphene on Si/SiO_2 vs. wavelength and oxide thickness 13
8. Hall coefficient of few-layer graphene vs. gate voltage 15
9. Conductivity of few-layer graphene vs. gate voltage 16
10. Bandstructure of BLG under zero bias (dotted) and with applied bias (solid) 19
11. Bandgap of GNR vs. ribbon width (length ~ 200nm) 20
12. Optical microscope image of FLG obtained by micro-mechanical cleavage 22
13. Representation of functional groups in GO 24
14. Thermal reduction of GO in vacuum 25
15. Effect of gate voltage on GO in various stages of thermal reduction......................... 26
16. Flow-chart showing CVD growth/transfer process 28
17. Graphene nanoribbon formed by chemically unrolling CNT.................................... 30
18. Atomic force microscope schematic.. 32
19. AFM image (left) and height profile (right) of GO flake 33
20. Comparison of Raman spectra in graphene and bulk graphite 35
21. Detailed evolution of Raman 2D peak from graphene to bulk graphite..................... 36
22. Ideal MOSFET output curves 38

LIST OF FIGURES (Continued)

Figure Page

23. Top-gated GFET 39
24. Typical GFET behavior 41
25. Resistivity change in graphene upon exposure to various gasses.............................. 42
26. Conventional spin valve sensor 44
27. Resistance of spin valve vs. magnetic field 45
28. Basic solar cell design.. 47
29. Transmittance of various solar cell electrode materials.. 47
30. GO flakes on 90 nm SiO_2 (left) and on 300 nm SiO_2 (right).................................... 52
31. GO paper.. 53
32. One Liter of dispersed GO (left) and 2 oz spray bottle (right) 54
33. Photoresist used in “wet-etch” process to pattern metal layer.................................. 56
34. Karl Suss manual aligner 57
35. Photoresist patterned for four-point resistance structure 59
36. Thermal evaporator.. 61
37. Gold electrodes overlapping GO flake 63
38. Westbond model 747677E wirebonder.. 65
39. Ball bonds connect one 4-pt structure to four perimeter pads 67
40. SEM image of two-step metallization process... 68
41. SEM image showing epoxy and wire connecting to resistance structure.................. 68
42. ProboStat^{TM} with alumina shell (left) and with shell removed (center and right)...... 70
43. ProboStat^{TM} in tube furnace (left) thermocouple controller (right) 70

LIST OF FIGURES (Continued)

Figure Page

44. Experimental setup for in situ resistance measurements 71

45. SPA connections to electrodes overlapping GO flake 73

46. General features of magnetic hysteresis loop 74

47. BH-Looper 76

48. Resistance of GO changing as sample 1 undergoes reduction process 78

49. Resistance of GO changing as sample 2 undergoes reduction process 79

50. Resistance of GO changing as sample 3 undergoes reduction process 80

51.Optical microscope images of samples 81

52. sample 2 - a.)3D AFM image. b.)optical image. c.)AFM image.
d.)height profile along the line shown in(c.)………….............................82

53. Raman spectra of both reduced and unreduced GO.. 83

54.Conductivity increases with substrate bias 84

55 Current flow through “source” electrode vs. ”drain” and “gate” voltages 85

56. Substrate patterned with permalloy structures 86

57.Representative hysteresis loops for short and long contact designs 87

58. Two possible “spintronic” devices based on graphene.. 93

59. Carbon fim grown by CVD on nickel 94

60. AJA “ATC Orion” sputter system 108

61. AJA sputter tool with main chamber open 110

LIST OF TABLES

Table | Page

1. Tool settings for wirebonder 66

2. Summary of results for samples 1-3 80

3. Resistance of sample 4 repeatedly heated and cooled to room temp 81

4. Results of coercivity measurements 87

5. Comparsion of electrical properties of graphene obtained by different methods 89

6. Experimental sputter rates for copper target in 3” DC cathode 111

7. Sputter rates for materials relative to copper (from AJA manual) 111

8. Experimental sputter rates for magnetic targets in 2” DC cathode 112

Electrical Characterization of Thermally Reduced Graphite Oxide

1 Introduction

Graphene is the name given to a single atomic plane of carbon atoms bonded together in a hexagonal lattice. The three-dimensional structure built of stacked sheets of graphene is nothing other than the "ordinary" graphite found in billions of pencils around the world. Interestingly, it was not until 2004 that researchers were able to isolate two-dimensional graphene from its bulk state [1]. Experiments revealed that graphene is a zero-bandgap material and that both the type and density of charge carriers can be tuned by the application of an electric field. This immediately made it an attractive candidate as the base material for a new class of transistor devices. Since this initial discovery, an astonishing amount of information about graphene has appeared in the scientific literature (as of June 2010, a search of the word "graphene" on the Web of Science database returns 6,771 results). Andre Geim, one of the authors of the seminal 2004 paper, has been publishing yearly update articles, surveying the state of the field [2, 3, 4].

There exist several techniques for the preparation of samples of graphene. The oldest method is mechanical exfoliation of highly oriented pyrolitic graphite (HOPG), which is traditionally done using Scotch tape to repeatedly cleave the sample thinner and thinner [1]. This technique has many disadvantages, such as the high cost of HOPG, the low yield of atomically thin samples, and the inability to place the graphene sample in a desired location. Another technique involves the "graphitization" of the surface of silicon carbide (SiC) by heating SiC wafers typically to beyond 1150 ºC so that silicon atoms desorb, leaving behind a single layer of carbon atoms (epitaxial graphene) [5]. This technique has the advantages of both high yields of few-layer samples and controlled placement of those samples (by masking certain areas to inhibit desorption of Si). Disadvantages of the method includes very high cost of SiC substrates, the fact that it requires a very high temperature furnace, and also that the "graphene" remains chemically bound to the substrate making it subtly different from graphene obtained by mechanical cleavage [6]. Most recently, progress has been made using chemical vapor deposition to grow layers of graphene on the surfaces of various metals, nickel being very

common. With this technique, the graphene samples can be easily patterned and transferred to other substrates [7].

This work will report on the electrical characterization of samples of graphene obtained by the thermal reduction of graphite oxide (GO) in a forming gas ambient (N_2/H_2). For the production of graphite oxide, Hummers' method [8] as modified by Kovtyukhova [9] was used. This process is used to transform graphite powder (SP-1 grade, 325 mesh) into an aqueous suspension of very small hydrophilic platelets of graphite oxide (a few microns from edge-to-edge and only a few nm thick). The GO thus produced is a strong insulator and must have its oxygen-containing functional groups removed (i.e., be chemically reduced) to be of any use electronically [10]. One of the most common methods of reduction involves flowing hydrazine vapors over the samples (chemical reduction). While this method has been shown to increase the conductivity of GO samples by several orders of magnitude, [11, 12, 13] it involves the use of a poisonous and potentially explosive chemical. There have also been some investigations into the thermal reduction of GO by exposing it to elevated temperatures. These experiments have been carried out both in atmosphere [14] and in vacuum, [15] but have yet to be performed in the presence of the relatively benign forming gas mixture. This work also begins an attempt to investigate spin transport through samples of thermally reduced GO. To date, reports of the magnetoresistive behavior of graphene in the scientific literature have been restricted to samples obtained by micromechanical cleavage of bulk HOPG [16, 17]. Investigations into the spin transport properties of reduced graphite oxide (rGO) have not been reported.

This thesis is organized as follows: Chapter 2 is a comprehensive review of the literature regarding graphene. In this chapter, the physical properties that make graphene interesting are discussed. The various techniques for isolating graphene are discussed in detail, as are techniques for determining the number of atomic layers in a sample and also potential applications for this most modern of materials. Chapter 3 focuses on fabrication and characterization techniques employed in this research project. Chapter 4 summarizes the results of this work, showing the effect of heating in a controlled atmosphere on the

resistivity of atomically thin graphite oxide particles. The results of investigations regarding the fabrication of independently switchable magnetic contacts are also reported. Chapter 5 consists of a discussion of the significance of these results, and the sixth and final chapter concludes with suggestions for future work.

2 Literature Review

This chapter reviews the nascent field of graphene technology. Various physical properties of the material are explored, as are several device applications making use of these properties. The various techniques used to isolate single-layer graphene are discussed at length and the primary techniques used to identify this atomically-thin material are examined.

2.1 Properties of Graphene

As mentioned, there has been enormous interest in graphene because it has attractive electrical properties that can be potentially exploited to build better electronic devices. Graphene also possesses myriad other unique characteristics that make it interesting, both for potential material applications and also for the insight that it can provide physicists seeking to better understand the fundamental laws of nature. In this section, the physical description of graphene as a macro-molecule are first reviewed. Secondly, interesting quantum-mechanical properties are discussed with the focus being on the unique manifestation of the quantum Hall effect in graphene. Next, the macroscopic qualities that make graphene useful are detailed with the emphasis being on electrical transport characteristics. Finally, bi-layer graphene and graphene nanoribbons are investigated, each having unique characteristics not seen in large-area single-layer graphene.

2.1.1 Physical Description

The graphene molecule consists of carbon atoms bonding together in a two-dimensional hexagonal structure. Each carbon atom bonds with three other carbon atoms with highly directional and very strong sp^2 hybridized σ-bonds (bond length of 1.42 Å). In bulk graphite, each graphene sheet is weakly bound to another by delocalized π-bonds (bond length of 3.35 Å). In graphene these electrons are unbonded and available for electric conduction. The structure of graphene can be viewed as two interpenetrating

triangular lattices of “type A” carbon atoms and “type B” carbon atoms (see Figure 1). The real-space lattice vectors are given by:

$$\overline{a_1} = (a/2)*(\sqrt{3},1) \;;\; \overline{a_2} = (a/2)*(\sqrt{3},-1)$$

where $a = \left|\overline{a_1}\right| = \left|\overline{a_2}\right| = \sqrt{3} * 1.42$ Å. The angle ABA is 120° and the atomic density of graphene is $3.82*10^{15}$ atoms/cm^2.

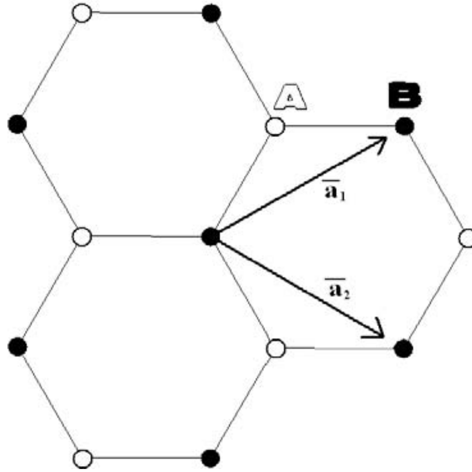

Figure 1. Real-space lattice description of graphene

The reciprocal (inverse) lattice of a 2D lattice is also two-dimensional and for graphene is also hexagonal. It can be shown that the inverse lattice of an “infinite” sheet of graphene has basis vectors given by:

$$\overline{b_1} = (2\pi/a)*(1/\sqrt{3},1) \;;\; \overline{b_2} = (2\pi/a)*(1/\sqrt{3},-1)$$

According to the well-established formalism, the “position” of an electron in reciprocal space (also called k-space) is related to its momentum in real space: $p_i = \hbar k_i$. The subscript i = 1,2,3 refers to the component of each quantity projected onto each of the three linearly independent axes chosen to represent the system. Another fundamental relationship (deBroglie’s) links the k-vector (also called wave-vector) to electron’s wavelength: $\lambda = 2\pi/|k|$.

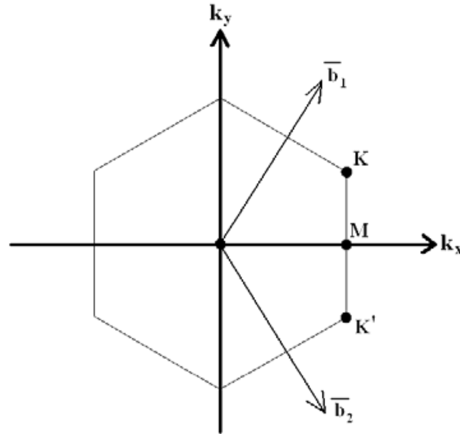

Figure 2. Reciprocal-space description of graphene

Bandstructure calculations have predicted that at the K-points in reciprocal space (see Figure 2) the conduction band and the valence band of single-layer graphene touch. The wave-vectors belonging to electrons at the six equivalent K-points are given by the following [18]:

$$\overline{k} = (\pm 2\pi / \sqrt{3}a, \pm 2\pi / 3a) \text{ also } (0, \pm 4\pi/3a)$$

This corresponds to electrons traveling in the direction of the real-space fundamental lattice vectors and having a wavelength equal to 3.69 Å.

The energy at which the bands touch coincides with the Fermi energy. As a consequence, the valence band is entirely full and the conduction band contains no electrons (the material is what is known as a zero-bandgap semiconductor). As the number of layers in the graphitic sample increases, the energy bands start to overlap and the material becomes semi-metallic. With two layers, the overlap is 1.6 meV. The overlap increases with the number of layers, and at eleven layers the overlap is within 10 % that of bulk graphite (~41meV) [19].

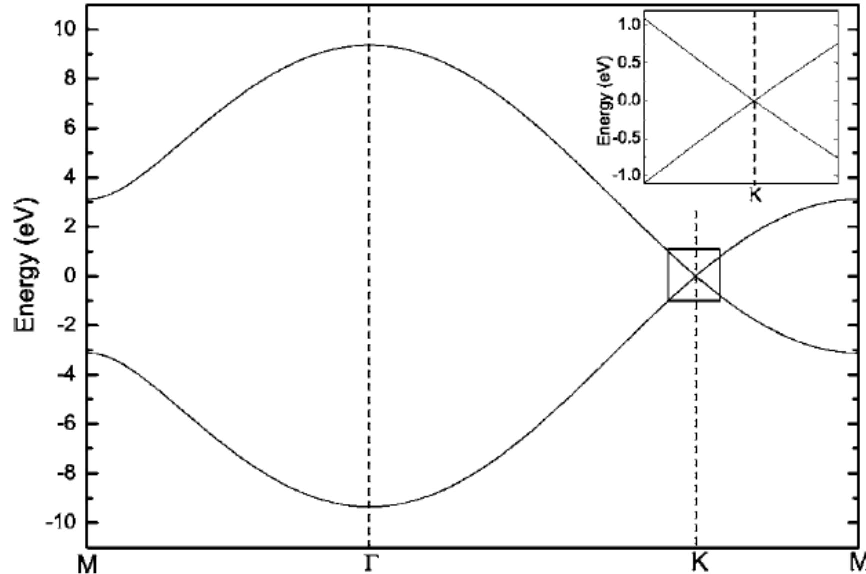

Figure 3. Calculated structure of single-layer graphene*

Another unique feature of the bandstructure of single-layer graphene is the linear dispersion around the K-point (see Figure 3). The velocity of an electron is proportional to the slope of the *E-k* curve: $v = (1/\hbar)*(\partial E/\partial k)$. This means that for graphene, the velocity of electrons near the K-point (those most likely to participate in conduction) is constant (~$1*10^6$ m/s). In the parlance of advanced physics, this linear dispersion is analogous to a system of relativistic paticles with zero effective mass [19]. It is this characteristic that is responsible for many of the interesting quantum mechanical effects observed in graphene.

2.1.2 Interesting Quantum Mechanical Properties

It has been shown that electrons in graphene obey the Dirac equation (which is the relativistic analogue of the well-known Schrodinger equation) with the bizarre consequence that they have zero rest mass [20]. Graphene also displays such exotic behavior as the Klein effect (paradox) in which electrons can tunnel through potential

* Reprinted with permission from: Partoens. Phys Rev B. **74**, 075404 (2006). Copyright 2006 by the American Physical Society

barriers with almost 100% probabilities. Prior to the discovery of graphene, the Klein paradox was only applicable to such experimentally difficult systems as black holes and high-energy nuclear collisions [21]. Graphene has become a favorite material of physicists looking to learn more about the fundamental laws governing quantum electrodynamics (QED).

One of the most studied quantum mechanical effects in graphene, and the only one to be discussed in detail in this work, is the "anomalous" quantum Hall effect. While much of the material that could be put in this section is well beyond the scope of a thesis in electrical engineering, it was felt that this subject is particularly relevant to the field and should be thoroughly digestible to the interested reader. It is also a particularly important effect, as it can be used to positively identify single-layer graphene [22].

Very briefly, the quantum Hall effect (QHE) is a property of 2-dimensional structures for which, in the presence of very strong magnetic fields, the Hall resistivity (ρ_{xy}) of the material takes on specific quantized values. In graphene, the QHE is said to be anomalous because ρ_{xy} is quantized differently than in other 2D systems, that is it takes on different values.

The "normal" Hall effect for 3-dimensional systems is a phenomenon that is commonly exploited in semiconductor characterization to determine both the density and the type of charge carriers (holes or electrons), as well as their mobility [23]. A voltage is applied across a material, causing a current to flow according to Ohm's law:

$$V_a = IR = I(\rho_{xx} L / tw)$$

In this equation, ρ_{xx} is a quantity known as the resistivity of the material. L,t, and w are dimensions of the sample as shown in Figure 4. If the applied voltage is known and the resulting current is measured, the resistivity can be easily calculated:

$$\rho_{xx} = (V_a / L)/(I / tw) = E_x / J_x$$

This equation also shows how the longitudinal electric field (E_x) and current density (J_x) can be defined.

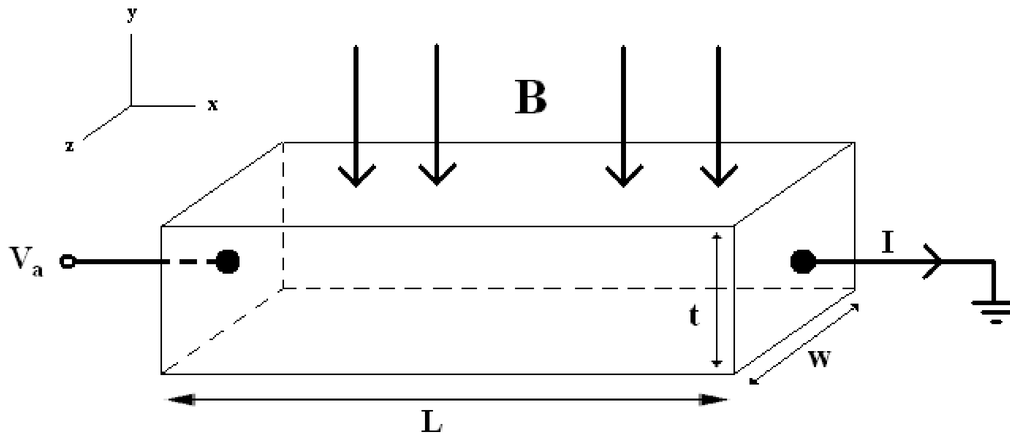

Figure 4. Hall effect in three-dimensional material

If a magnetic field is also applied perpendicular to the direction of current flow, a moving charged particle experiences a force (named after Dutch physicist Lorentz) which is perpendicular to both the field and to the direction of motion:

$$\overline{F} = q(\overline{v} \times \overline{B})$$

In this equation, $\overline{F}$ represents the force experienced by the particle, q is the charge of the particle, $\overline{v}$ is the particle's velocity, and $\overline{B}$ is the magnetic flux density at the location of the particle.

It is useful to consider the two cases of electron-mediated current and hole-mediated current separately with reference to the coordinate system of Figure 4. When holes are the dominant charge carrier, motion is in the positive x-direction and the cross product of velocity and field is in the negative z-direction (for magnetic field in negative y-direction as shown). For holes, the charge is positive and the force is in the same direction as the cross product. For electrons to be carrying current in the direction shown, they have to be traveling in the negative x-direction. This gives a cross product in the positive z-direction. However, the charge on the electron is negative making the force point in the negative z-direction.

The conclusion is that holes and electrons experience the same force and are accelerated toward the same face of the material. Over time, charge will accumulate on the face of the material, generating an electric field that will exactly cancel the Lorentz force and preclude the accumulation of further charge. This electric field (E_z) can be determined by measuring the "Hall" voltage (V_H) which develops between the two faces in the x-y plane (the front and back face in Figure 4): $E_z = V_H / w$.

In practice, the current density and the magnetic field are known quantities and the Hall voltage is measured. The Hall coefficient is defined according to:

$$R_H = E_z / J_x B_y = \pm 1 / nq$$

The polarity of the Hall coefficient informs the experimenter whether the current is carried primarily by holes or by electrons. The magnitude can be used to infer the density and mobility of the carriers (n).

More relevant to the discussion at hand is the quantity known as the transverse Hall resistivity:

$$\rho_{xz} = E_z / J_x = |B| / nq$$

It is seen that this quantity scales in a linear fashion with the applied magnetic field. In a two-dimensional structure, under specific conditions to be described, the transverse Hall resistivity is not a smooth linear function of magnetic field, but is instead quantized, occurring only in discrete values [24]. The conditions necessary for the observation of the quantum Hall effect are sufficiently high fields and low temperatures:

$$\omega_c \tau >> 1 \text{ and } \hbar\omega_c >> k_B T$$

where $\omega_c = q|B| / m_e$ is the cyclotron frequency (m_e is the mass of an electron). In the first constraint, τ represents the average time between phase-randomizing (inelastic) scattering events. In the second constraint, $\hbar$ is the reduced Planck's constant, k_B is the Boltzmann constant, and T is the temperature of the material. When the first inequality is satisfied, there is a high likelihood of an electron making at least one complete cyclotron orbit

before being scattered. In this regime, the transverse Hall resistivity manifests as a series of plateaus given by [24]:

$$\rho_{xz} = h / Nq^2 \approx (25.8\ k\Omega) / N$$

where *N* is an integer. For extremely high fields, *N* is unity. As field strength is reduced, *N* increases. As field is reduced further, the effect is eventually lost (because cyclotron frequency becomes too small) and a linear relationship between Hall resistivity and magnetic field is obtained (see Figure 5).

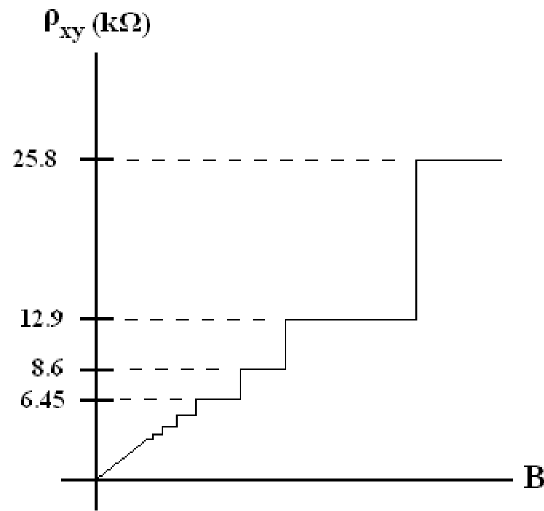

Figure 5. Integer quantum Hall effect

In graphene, it has been shown that the allowed quantized Hall resisitvities are not given by the familiar formula, but instead by:

$$\rho_{xz} = h / [4(N + 1/2)q^2] = (6.45\ k\Omega) / (N + 1/2)$$

N is now given by the integers including zero [25]. In Figure 6, the x-axis represents magnetic field in units of Tesla. The red line shows quantized levels of Hall resistivity (compare to figure 5) and the blue line shows Shubnikov-de Haas oscillations in the longitudinal resistivity. The behavior shown is a signature of single-layer graphene.

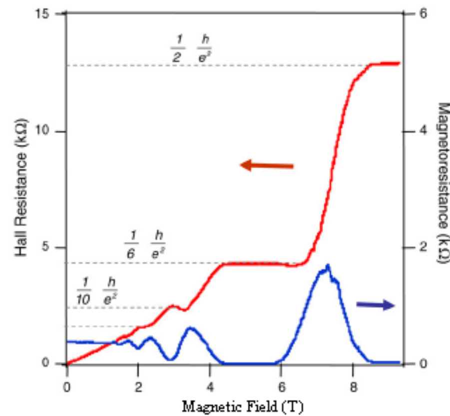

Figure 6. Half-integer quantum Hall effect in graphene*

2.1.3 Interesting Macroscopic Properties

In addition to subtle properties like the anomalous "half-integer" QHE, graphene possesses large-scale properties which make it a useful material from an engineering perspective. The focus of this section will be on electrical transport properties (including spin transport), but a brief survey will first be made of other interesting mechanical, thermal and optical properties.

Mechanically, graphene is the strongest material ever measured, with a breaking strength of 42 N/m. The ratio of stress to strain, the Young's Modulus, has been determined to be on the order of 10^{12} N/m^2 [26]. It is also quite flexible and stretchable. Experiments have shown very little change in the electrical resistance of graphene as it is folded and stretched to produce tensile strains in the material of up to 6.5 percent. Resistance has been shown to return to its original value after up to 18.7 percent strain has been applied and subsequently removed [22]. Graphene has also been shown to have the highest known thermal conductivity at 3000-5000 W/m-K [27]. Optically, graphene is quite transparent with 60-70 % transmittance over the visible and infrared regions of the

---

* Reprinted from Solid State Communications, **143**, Jiang, "Quantum Hall Effect in Graphene," pp 14-19,copyright (2007), with permission from Elsevier.

spectrum [28]. These properties of graphene make it perfectly suited to a large variety of applications to be discussed in Section 2.4.

Before discussing the electrical properties of graphene, a quick digression will be made to explain the visibility of graphene on the Si/SiO_2 substrate. It has been found experimentally that graphene becomes visible when placed on a silicon substrate with exactly 300 nm oxide. The reason graphene wasn't discovered until 2004 is related to the fact that on most surfaces it is invisible under optical microscopes [2]. Mathematical modeling of the system has been done to calculate the contrast (defined as relative intensity of reflected light in the presence and absence of graphene) as a function of both the thickness of the oxide and the wavelength of the light. In the study, the refractive index of graphene was taken to be that of bulk graphite (2.6-1.3i) with no wavelength dispersion. The results are summarized in Figure 7 and suggest that for a 300 nm oxide, contrast is highest under green light. It also suggests that a 90 nm oxide may provide better overall contrast over a large range of wavelengths [29].

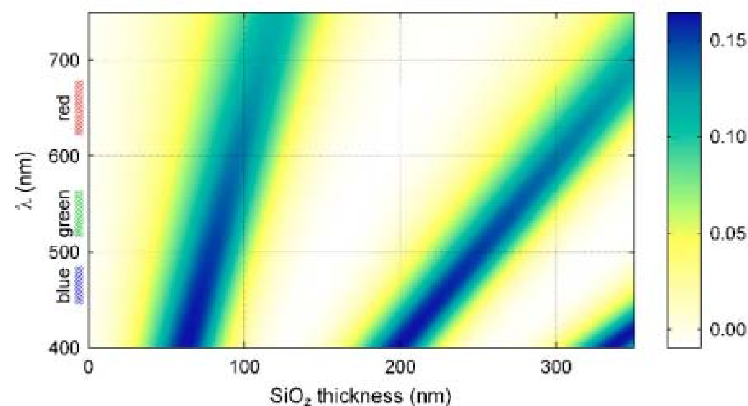

Figure 7. Contrast of Graphene on Si/SiO_2 vs. Wavelength and Oxide Thickness*

Electrically, graphene is neither a conductor (with lots of available energy states within a few k_BT of the Fermi energy) nor a semiconductor/insulator (with a large gap separating the Fermi energy from unoccupied states). The valence and conduction bands

---

* Reprinted with permission from: Blake. Appl Phys Lett. **91**, 063124 (2007). Copyright 2007, American Institute of Physics.

touch at the Fermi level (see Figure 3) so that there is not a large amount of either holes or electrons available to carry current. It has been shown that in this state the conductivity of graphene is a minimum and is given by: $4q^2/h$ = 154.5 μS (in this equation, q is the charge of an electron and h is Planck's constant) [21]. This is a quantum mechanical effect and an explanation of its origin will not be attempted here. It will be pointed out that the units are appropriate to a two-dimensional material such that conductance equals the conductivity scaled by the ratio of width to length (length is along the direction of current propagation).

It has been shown experimentally that the carrier concentration, and hence conductivity (given by the product of charge, carrier density, and carrier mobility), can be increased by application of an electric field [1]. In the original 2004 experiment by Novoselov, single-layer graphene flakes obtained by repeated mechanical peeling of bulk HOPG were dispersed onto a silicon wafer with 300 nm silicon dioxide. Metallic contacts were defined atop the graphene samples and the degenerately-doped silicon substrate acted a gate electrode. It was seen that when the gate voltage (V_G) was positive, the Hall coefficient was negative indicating charge carried by electrons. As the magnitude of the gate voltage increased, the magnitude of the Hall coefficient decreased indicating an increase in electron density. Conversely, when the gate voltage was negative the Hall coefficient was positive implicating holes as the dominant charge carrier. Again, as the magnitude of the gate voltage increased, the carrier density also increased.

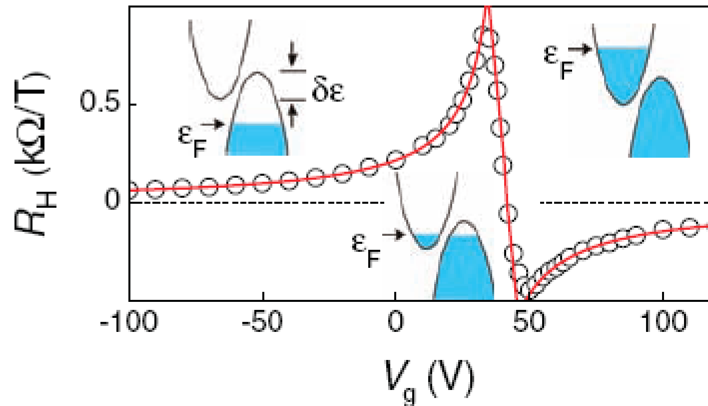

Figure 8. Hall coefficient of few-layer graphene vs. gate voltage*

Two comments must be made in explanation of Figure 8. The first is that the bands are drawn as appropriate for few-layer graphene, not for single-layer graphene. Single-layer material would not show the overlap of valence and conduction bands. Secondly, the neutral level of equal numbers of charge carriers does not occur at zero gate voltage as expected. This was attributed by the authors to unintentional doping due to water adsorption, and annealing was reported to cause a shift toward zero volts.

The observed behavior can be easily explained as a capacitive effect: $C=Q/V$. Using the parallel-plate approximation for capacitance ($C=\varepsilon A/d$) with the permittivity of SiO_2 (ε=3.9*8.85*10^{-12} F/m) and the distance between "plates" as the thickness of the oxide (d=3*10^{-7} m) gives an areal capacitance of 115 μF/m^2. Dividing this by the charge per carrier (1.6*10^{-19} C) gives the carrier density as a function of gate voltage: 7.2*10^{14} carriers/V-m^2. This linear dependence of carrier concentration to gate voltage can be inferred from the Hall measurements of Figure 8 (remember that $R_H=\pm 1/nq$), but is more easily seen in Figure 9.

* From: Novoselov. Science. **306**, 666 (2004). Reprinted with permission from AAAS.

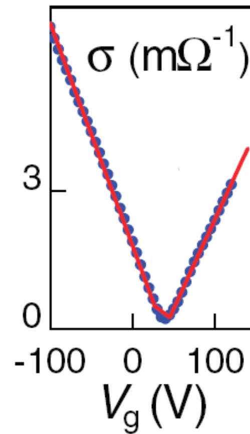

Figure 9. Conductivity of few-layer graphene vs. gate voltage*

Based on the measured carrier concentration and conductivity, Novoselov and his colleagues determined the mobility of few-layer graphene via the relationship ($\mu = \sigma/qn$). The mobility varied from sample to sample between 3000 to 10,000 cm^2/V-s and was independent of either gate voltage or temperature. Graphene was also found to be able to support a large current density of greater than 10^8 A/cm^2 before being destroyed (if the reported current density was calculated by assuming a nominal thickness of 3.35 Å, this would correspond to a "two-dimensional" current density of 3.35 A/cm). The significance of these results will be made clear in Section 2.4.1 when graphene-based transistors are discussed.

Spin transport in graphene has been investigated by Hill [16] who deposited permalloy ($Ni_{80}Fe_{20}$) contacts on a graphene sample and ran current through it. In the experiment, the direction of magnetization of each of the two ferromagnetic contacts could be set independently due to differences in coercivity resulting from irregularities in shape. Using graphene obtained by peeling from HOPG (see Section 2.2.1), a change in resistance of 10 % was reported when the relative direction of magnetization of the two contacts was switched from parallel to anti-parallel (at room temperature). The distance between the permalloy contacts was 200 nm.

---

* From: Novoselov. Science. **306**, 666 (2004). Reprinted with permission from AAAS.

This is a manifestation of the giant magnetoresistive effect (GMR) originally observed in multilayers of alternating magnetic and nonmagnetic conductors [30]. When both contacts are magnetized in the same direction (parallel state) there is less scattering at the second graphene/permalloy interface, and consequently less resistance, than when the contacts are magnetized in opposite directions (anti-parallel state). This is referred to as spin-dependent scattering. It results from the fact that there are more energy states in the contact that are available to be populated by electrons with spins orientated in the same direction as the magnetization of the contact. Conversely, there are less energy states in the contact available to be populated by electrons with spin oriented opposite the direction of magnetization of the contact [31]. For the observation of the GMR effect two phenomena must occur: the first of these is spin injection, and this occurs at the first permalloy/graphene interface. The second phenomenon is that the injected electrons must not re-orient their spin by the time they reach the second permalloy/graphene interface.

When electrons passing through a magnetic contact into a nonmagnetic material (such as graphene) keep their spins oriented in the same direction as the magnetization of the contact, it is referred to as spin injection. It has been shown that the degree of spin injection is approximately proportional to the ratio of the resistivity of the magnetic contact to the resisitvity of the nonmagnetic material [32]. An electric field could, in principle, then be used to modulate spin injection through modulation of graphene's resistivity (as discussed in Section 2.1.3). Efficient spin injection can also be achieved (in spite of a nonmagnetic material's potentially large resistivity) by using a tunnel barrier in the form of a very thin oxide between the materials [33].

The second condition that must be met for GMR to occur is that the spin diffusion length (λ_{sf}) in the nonmagnetic material must be at least as large as the separation between magnetic contacts. This will determine whether or not the polarity of the injected electron has still been maintained by the time it reaches the second graphene/permalloy interface. If it has not, then spin dependent scattering cannot occur and the GMR effect will not be observed.

As electrons travel through the nonmagnetic material (graphene) they experience scattering events which will randomize the direction of spin orientation. The dominant mechanism is spin-orbit scattering and an average time between spin-randomizing scattering events (τ_{sf}) can be defined. The spin diffusion length is then defined according to:

$$\lambda_{sf} = \sqrt{D\tau_{sf}}$$

where D is the diffusion constant of the material [34]. The reports by Hill (in reference 16) of an observed GMR effect in graphene can be taken as evidence that the spin diffusion length is at least 200 nm, the spacing between the magnetic electrodes.

In a separate study, a magnetoresistive effect (though much smaller than found by Hill, at only 0.25 %) was observed in multilayer graphene (MLG) consisting of roughly six layers spanning magnetic contacts separated by 500 nm, suggesting that the spin diffusion length in MLG (isolated by peeling of HOPG in this study as well as Hill's) is not less than half a micron [17]. Other work using a four-terminal "non-local" technique has found the spin diffusion length to be between 1.5 µm - 2 µm at room temperature in single-layer graphene also obtained by peeling HOPG [35].

2.1.4 Bilayer Graphene and Graphene Nanoribbons

It has been stated that bilayer graphene (BLG) and graphene nanoribbons (GNR) have unique characteristics not seen in single-layer large-area graphene. The most interesting and potentially useful characteristic of bilayer graphene is the ability to open and tune the bandgap of the material by application of an electric field. By applying an increasing voltage to a gate electrode, bilayer graphene can theoretically be continuously tuned from a semimetal with a band overlap of 1.6 meV to a semiconductor with a band gap of up to 200 meV. Bilayer graphene is the only known material with an electrically tunable energy gap [36]. Considering the fact that a material will not absorb wavelengths longer than hc/E_G (where h is Planck's constant, c is the speed of light, and E_G is the energy gap between the valence and conduction bands), BLG can find many applications including tunable optical filters.

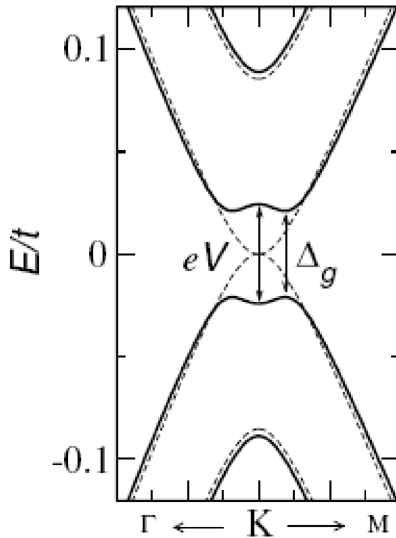

Figure 10. Bandstructure of BLG under zero bias (dotted) and with applied bias (solid)*

Graphene nanoribbons are distinguished by the fact that when the width of the sample becomes small enough (on the order of 10s of nm), a bandgap begins to open due to quantum confinement and edge effects, with the size of the gap being inversely proportional to the width of the sample. Energy gaps approaching 0.4 eV have been measured in GNR less than 10 nm wide (see Figure 11, in which the dotted line represents an empirical fit to the data of the form: E_G(eV)=0.8/w(nm) and the colored lines represent various first-principles calculations) [37].

Another interesting characteristic of graphene nanoribbons is that they can have much lower minimum conductivites than “bulk” graphene. Recall from Section 2.1.3 that when graphene is biased such that the Fermi energy lies at the level where the valence and conduction bands touch at the K-point, there are not large numbers of either type of carrier and the conductivity takes the minimum value of $4q^2/h$ = 154.4 μS. It has been demonstrated that as the width of the GNR shrinks, the minimum conductivity can be made to decrease well beyond the minimum value possible in bulk to as low as 10 nS for widths near 25 nm. A trend is also observed showing smaller minimum conductivities to

* Reprinted with permission from: Castro. Phys Rev Lett. **99**, 216802 (2007). Copyright 2007 by the American Physical Society.

be obtainable in GNR at lower temperatures [38]. A smaller minimum conductivity is necessary in order to achieve a larger on/off ratio when using graphene as a channel material in transistor devices (a point that will be discussed in greater detail in Section 2.4.1).

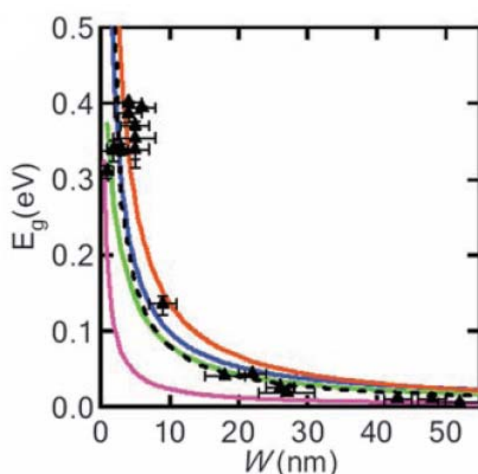

Figure 11. Bandgap of GNR vs. ribbon width (length ~ 200nm)*

2.2 Isolation Techniques

Though isolated from its bulk state only as recently as 2004, an amazing amount of resourcefulness has gone into looking for new ways to prepare single-layer graphene samples for application and study. This section follows the order of chronological development, starting with the method of micro-mechanical cleavage from highly oriented pyrolitic graphite (HOPG). Graphene obtained by the "graphitization" of various surfaces of silicon carbide is then be briefly discussed before the method of the synthesis and subsequent reduction of graphite oxide is discussed in greater detail. Next, new techniques involving chemical vapor deposition (CVD) of graphene from gaseous carbon sources onto the surfaces of various metals are reviewed. Finally, cutting-edge methods used to obtain graphene ribbons from carbon nanotubes are introduced.

* From: Li. Science. **319**, 1229 (2008). Reprinted with permission from AAAS.

2.2.1 Micro-Mechanical Cleavage

The original method used to isolate single-layer graphene was rather complicated compared to its direct descendant, which became known simply as the "Scotch-tape" method. Both methods involve mechanical cleavage (sometimes referred to as mechanical exfoliation) of graphene films from bulk carbon samples. The methods are mechanical because they rely on the application and subsequent removal of sticky tape to the sample to reduce its dimensions. A novel and somewhat related method involves using the electrostatic force resulting from application of a voltage across a sample of HOPG contacting a Si/SiO_2 substrate to exfoliate onto the SiO_2 surface monolayer and few layer graphene from the bulk HOPG [39].

The initial process developed by Novoselov and his colleagues involved lithographically patterning and oxygen-plasma etching five-micron high mesas onto the surface of a bulk sample of HOPG. The mesas were then pressed against fresh wet photoresist (PR) which was allowed to harden. These became attached to the PR and were able to be cleaved from the rest of the sample of HOPG. Each of the "islands" of graphitic material stuck in the photoresist was next peeled thinner and thinner by repeatedly using Scotch tape to remove layer after layer, leaving only single and few layered samples behind. Finally, the atomically thin flakes were released in acetone and dispersed on a substrate of oxidized silicon [1].

The now-famous Scotch-tape method starts with taking a piece of tape, sticking it to a sample of HOPG, and peeling off the top layers. With a chunk of graphitic material stuck to the tape, the tape is doubled back on itself and pressed against the graphitic material again. By unpeeling the tape, the material is separated into two pieces. This process is repeated approximately ten times, each time cleaving the material thinner until eventually single-layer regions remain stuck to the tape. The tape is then pressed (graphene side down) against an oxidized silicon wafer. The backside of the tape is rubbed for several minutes with soft plastic tongs to transfer the graphene to the oxide before slowly removing the tape [3].

The Scotch-tape method is relatively easy to apply, though finding single-layer samples can be challenging amidst the thicker pieces. Figure 12 shows a microscope image of few layer graphene (FLG) samples obtained by the author using the Scotch-tape method. The purple regions at the lower right are thinnest. For years, mechanical exfoliation from HOPG was the method used for production of high-quality graphene, rivaled only recently by chemical vapor deposition (CVD) techniques to be discussed in Section 2.2.4.

Figure 12. Optical microscope image of FLG obtained by micro-mechanical cleavage.

2.2.2 Graphitization of SiC

It has been known since at least 1998 that the graphitization of silicon carbide (SiC) surfaces could be accomplished by heating it to temperatures sufficient to sublimate silicon atoms, leaving the surface carbon rich. It was found that an epitaxial layer of graphite could be engineered on 6H-SiC(0001) surfaces by heating the material under vacuum to 1400 °C. Rather thick graphitic layers were obtained, but it was speculated that single layer samples could be produced by proper annealing [40].

SiC, also known as Moissanite or Carborundum, was first reported around 1885 by Dr. Edward Goodrich Acheson. SiC does not occur naturally except in meteorites, and

was originally produced by heating silica sand and carbon in an electric furnace to very high temperatures (the Acheson process). SiC occurs in about 250 crystalline forms or "polytypes". The 6H (also known as the α) polytype has a hexagonal crystal structure similar to Wurtzite and is a wide-bandgap semiconductor with a gap of 3.05eV [41].

The first reported demonstration of controlled growth of truly two-dimensional graphene films on SiC is attributed to Berger and his coworkers in 2004, interestingly at almost exactly the same time that Novoselov and his colleagues reported graphene derived by their own techniques. Very similar experiments were even performed by the two groups, with the Berger team also performing magnetoresistance measurements. They were unable to directly observe a quantum Hall effect, however, though they did suspect that one should be found [42]. Much progress has since been made in the art of "growing" atomically thin carbon layers on different surfaces of various polytypes of SiC (see reference [5] for a good review).

Electrical transport properties of SiC-derived graphene have been shown to be similar to those of exfoliated graphene. There are however, a few interesting effects unique to the method and deriving from the intimate contact of the carbon layer with the SiC substrate. For example, in graphene grown on the (0001) surface, the Fermi level lies 0.4 eV above the point when the valence and conduction bands touch, making the material n-type (an example of substrate doping) [43]. To be more precise, the Fermi level lies 0.4 eV above the point where the bands would normally touch in graphene (if not for the SiC substrate). It has been shown that when single-layer graphene is grown on SiC, a bandgap of 0.26 eV is created in the material. This substrate induced band gap decreases with carbon thickness and by about four layers has disappeared [44].

2.2.3 Reduction of Graphite Oxide

Graphite oxide (GO) was first prepared by Brodie as long ago as 1859 by treating pure graphite with potassium chlorate and nitric acid. In 1898, Staudenmaier introduced a method which also included sulfuric acid as an oxidizing agent. Hummers, in 1958,

published the method of preparation that would later become the method of choice for graphene researchers [8].

The exact procedure used to synthesize the graphite oxide investigated in this work is given in Appendix A. Briefly, the method of Hummers involves mixing powdered flake graphite with sulfuric acid (H_2SO_4), sodium nitrate ($NaNO_3$) and potassium permanganate ($KMnO_4$). The modification of Kovtyukhova to the method of Hummers [9] requires the pretreatment of the graphite with sulfuric acid, potassium persulfate ($K_2S_2O_8$) and phosphorous pentoxide (P_2O_5) and neglects the sodium nitrate in the main oxidation step of Hummers.

Once synthesized, the graphite oxide is hydrophilic and can be dispersed in water to extremely thin sheets consisting of a single and few layer oxidized carbon. The GO platelets differ from "pristine" graphene, however, by the fact that they have very low electrical conductivity [13]. The conductivity of GO is low because of the presence of hydroxyl and epoxy functional groups chemically bonded to the surface of the underlying graphene (see Figure 13, which shows carbon atoms in black, oxygen in blue, and hydrogen in green). The exact structure of GO is amorphous with surface coverage anywhere between 25-75% and a chemical formula ranging from $C_8H_2O_3$ to $C_8H_4O_5$. The key to recovering the conductivity of GO is the removal of these functional groups [10].

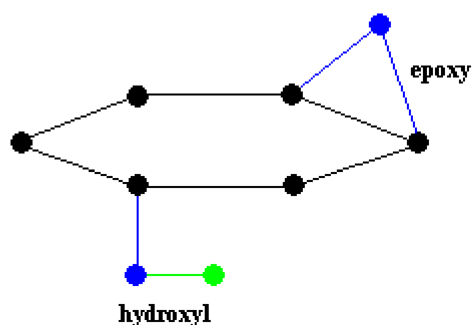

Figure 13. Representation of functional groups in GO

The removal of functional groups has been attempted both thermally, exposing the GO to elevated temperatures [14, 15], and chemically, using hydrazine [11, 12, 13].

In almost all studies, the GO was first dispersed in solution, then deposited onto the surface of a substrate (usually Si/SiO_2 by spray deposition) where metal contacts were lithographically defined and transport measurements were taken.

In the thermal reduction studies of Jung [15], GO flakes were subjected to a repeated cycle of heating and cooling under vacuum while conductivity was monitored using a four-point contact structure. Initially, the resistance of the GO was so high as to be essentially unmeasurable. By the time the sample reached 160 °C, however, the resistance had dropped to about 5 GΩ. Resistance was shown to increase somewhat during those times when the sample was allowed to cool, but it then decreased to even lower values during the cycles of reheating. For the four heating cycles shown, the sample reaches a minimum resistance of about 2 MΩ (see Figure 14 which shows sample resistance in solid red and temperature in a dotted black). The maximum conductivity reported by these methods is ~85 S/m.

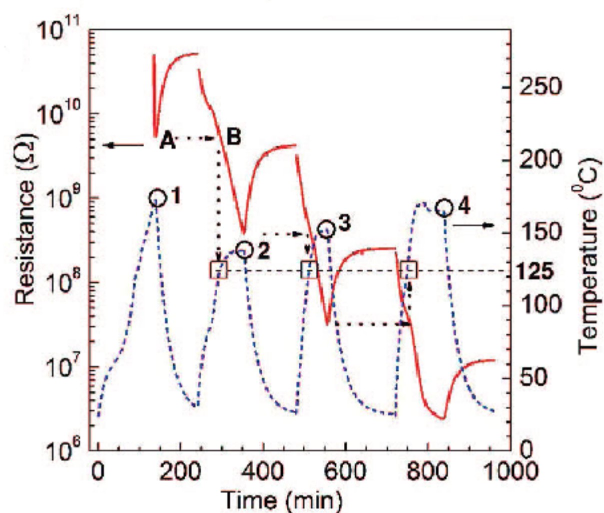

Figure 14. Thermal reduction of GO in vacuum*

Another interesting result from the studies of Jung is that the ambipolar field effect is observed in samples of GO at all stages of reduction, with a maximum resistance

* Reprinted with permission from: Jung. Nano Letters. **8**, 4283 (2008). Copyright 2008 American Chemical Society.

corresponding to the charge neutral point occurring very near to zero gate bias (see Figure 16a, which shows data for four different samples, the top two curves belonging to the same sample in different stages of reduction). When the sample is removed from vacuum and exposed to air however, the field effect displays hysteresis (see Figure 16b) which can be removed by reheating the sample under vacuum. This is evidence that the properties of thermally-reduced GO are inherently unstable.

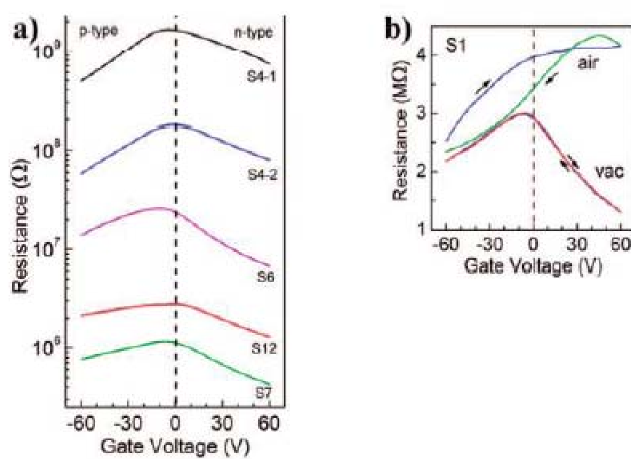

Figure 15. Effect of gate voltage on GO in various stages of thermal reduction*

The reports of chemical reduction using hydrazine all suggest that the method may be an effective way to increase the conductivity of GO samples, although in situ and time dependent studies have yet to be performed. Gilje [11], studying continuous films of overlapping GO platelets, has shown the sheet resistance of such films drops from about $4*10^{10}$ Ω/square to about $4*10^{6}$ Ω/square before and after hydrazine treatment. He also reported field effect measurements using a gate bias which suggest that chemically reduced GO is p-type (resistance steadily increased as gate bias was swept from -15 V to +15 V). Gomez-Navarro [12] has reported chemically reduced individual GO monolayers displaying conductivities between 0.05 S/cm and 2 S/cm and mobilities of 2 cm^2/V-s to 200 cm^2/V-s (both quantities far inferior to that seen in "pristine" graphene). He, like

* Reprinted with permission from: Jung. Nano Letters. **8**, 4283 (2008). Copyright 2008 American Chemical Society.

Jung, was able to observe the ambipolar field effect and also noted that several hours of exposure to ambient chemical reduction resulted in a shift of the resistance maxima toward positive gate voltages. Stankovich [13] reports the conductivity of chemically reduced GO powder to be about 200 S/m which he describes as five orders of magnitude better than the conductivity of (unreduced) GO.

A unique method reported for the reduction of GO involves using a Xenon flash from a camera to trigger reduction via the suggested mechanism of photo-thermal heating. This technique promises selective reduction of desired areas of GO (say to create conducting channels) by masking certain areas of the sample from the flash. After exposing roughly 1 μm thick films of GO to flash energies of 0.1-2 J/cm^2, volume shrinkage, cracking, and color-change were visually apparent. Repeated flashing is even shown to obliterate the GO film, effectively etching the exposed regions. The conductivities of flash reduced large-area films were found to be around 1000 S/m [45].

2.2.4 Chemical Vapor Deposition

The most recent advances in graphene isolation/fabrication technology have produced ever larger samples of high quality single-layer material using chemical vapor deposition (CVD) of carbon precursors (such as methane, ethylene, or hexabenzocoronene) on the surfaces of various metals (such as Ni, Cu, Co, or Ru) [7, 22, 46, 47, 48]. Kim [22] reports graphene grown on nickel covering areas up to 2.5 cm x 2.5 cm, with sheet resistance as low as 280 Ω/square and electron mobility as large as 3700 cm^2/V-s.

In all CVD techniques, the exact flow rate of carbon-containing precursors (as well as inert and reducing gasses), the temperature of the flow-cell, the heating and cooling rates, and the thickness of the metal layer are all important variables that must be tuned to achieve large-area continuous single-layer graphene growth. As an example, this section will describe the method of Reina [7] in some detail.

The synthesis process employed by Reina starts with 500 nm nickel films evaporated onto oxidized silicon substrates. The CVD process actually consists of two

steps. In the first, the sample is heated to 900 °C - 1000 °C for 10 minutes - 20 minutes under argon and hydrogen flow (600 sccm and 500 sccm, respectively). The purpose of this is to cause the polycrystalline nickel to form larger grains (1 μm -20 μm), enabling better uniformity of graphene to be grown. The second step is the actual CVD growth. The sample is maintained at 900 °C – 1000 °C while the hydrogen flow is increased to 1500 sccm and methane flow is substituted for the argon (5 sccm - 25 sccm). The exposure time is 5 minutes - 10 minutes.

Further work by the group [49] has investigated the effect of the rate of cooling. During the CVD process, carbon is dissolved into the bulk of the nickel film and only precipitates to the surface as it is cooled. It was found that slower cooling rates (less than 25 °C/min) gave a greater area covered by 1-2 layer films than faster cooling rates (more than 100 °C/min). For very slow cooling rates (4 °C/min), the area covered by no thicker than two-layer graphene was a maximum 87 %. The work by Kim (also decomposing methane on nickel) suggests an optimal cooling rate of 10 °C/sec [22].

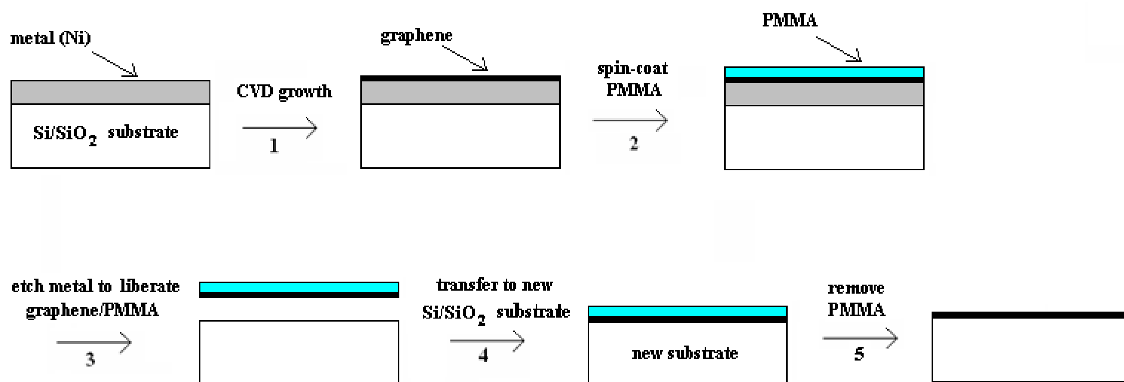

Figure 16. Flow-chart showing CVD growth/transfer process

In addition to large-area coverage and superior electrical properties, CVD graphene has further advantages of being both easily patterned (by etching the nickel prior to growth) and easily transferable to other substrates (by etching the nickel after growth to liberate the graphene sample). When etching away the nickel for transfer of graphene films, it is important to first coat the top of the graphene with some material

that will offer mechanical stiffness. Reina's group uses polymethylmethacrylate (PMMA) to coat the sample and provide mechanical stability as the film is transferred. The PMMA is then rinsed away with photoresist stripper. Alternatively, Kim's group uses polydimethylsiloxane (PDMS) for the purpose of structural support. PDMS is not easily dissolvable, but can be used as a "stamp" to transfer graphene to substrates to which the samples will have a greater affinity than to the PDMS.

2.2.5 Graphene from Carbon Nanotubes

The final method for graphene preparation to be discussed in this thesis uses carbon nanotubes (CNT) as starting material and "unzips" them to form graphene nanoribbons. This is a particularly useful technique because graphene has been shown to display interesting quantization effects as its dimensions are reduced (see Section 2.1.4). There exist two main techniques for unzipping nanotubes: chemical treatment and plasma etching. In this discussion, the method of fabrication of CNT will not be treated.

In the chemical unzipping method, CNT are suspended in concentrated sulfuric acid. Dilute $KMnO_4$ (potassium permanganate) is then added and the solution is heated for thirty minutes. This treatment unrolls the CNT, but also oxidizes the material so that what is obtained is actually a nanoribbon of graphite oxide. As discussed in Section 2.2.3, the nanoribbons must subsequently be reduced (using hydrazine or other methods) [50].

The method involving plasma etching produces higher-quality samples than the chemical method, but is slightly more complicated as the CNT must first be embedded in a PMMA matrix. Etching was accomplished in argon plasma with power set at 10 W and a pressure of 40 mTorr [51].

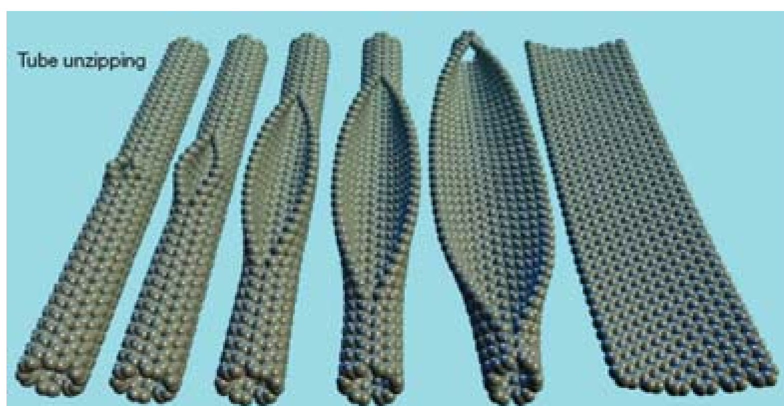

Figure 17. Graphene nanoribbon formed by chemically unrolling CNT*

2.3 Identification Techniques

Location and determination of the number of layers in a sample of graphene is accomplished by the use of three primary techniques: optical microscopy, atomic force microscopy (AFM), and Raman spectroscopy.

2.3.1 Optical Microscopy

Optical microscopy is typically the first step in attempting to locate potential samples of graphene, as it is much less time consuming than AFM or Raman and allows larger areas to be scanned. As previously stated (in Section 2.1.3), the optical contrast of graphene can be enhanced by placing it on a silicon wafer oxidized to an optimal thickness (300 nm is standard). Modern optical microscopy can be used to image features no smaller than about half of a micron. This fundamental limitation is due to the wavelength of light in the optical spectrum, and the ultimate possible magnification by optical methods is about 750x [23].

Returning to the relevance of optical microscopy to graphene research, it should be pointed out again that layers of different thicknesses appear differently colored when viewed under a microscope (see reference [1] supplementary information). For

* Reprinted with permission from Macmillan Publishers Ltd: Kosynkin. Nature. **458**, 872 (2009). Copyright 2009.

production techniques such as mechanical cleavage, which require finding suitable samples amidst a mass of unsuitable samples, optical microscopy is indispensable. Often, location marks are patterned on the substrate to help relocate potential graphene samples for more quantitative AFM or Raman characterization later. The author found it easiest to etch the marks into the oxide using hydrofluoric acid, but metal deposition (gold) followed by liftoff was necessary if the marks were to be visible under a layer of photoresist (which would be necessary for later alignment of strucutres to graphene samples).

2.3.2 Atomic Force Microscopy

AFM methods are among the highest resolution imaging techniques known. Proposed in 1986 by Binnig, Quate, and Gerber [52], the AFM combines the principles of the scanning tunneling microscope (STM) and the stylus profilometer. Atomic resolution is obtained by measuring the force between a surface and a very small, sharp tip at the end of a cantilever as the tip is scanned over an area of the surface. The tool was designed as a modification of the STM that would be capable of imaging insulators (the STM is only able to image conductors due to its reliance on tunneling current). The STM is used as a component of the original AFM to measure the deflections of the conductive cantilever. Piezoelectric actuators are used for very accurate control of all relative positionings. A common modification to the design of Binnig dispenses with the STM portion of the AFM entirely and uses a laser reflecting from the back of the cantilever into a photo-detector to sense tip motion [53].

As the sample is scanned beneath the probe tip, piezoelectric actuators also raise and lower the sample so that there is a constant force between the tip and the sample's surface. As the force on the cantilever changes (due to a surface feature), the laser is reflected onto different regions of the split segment photo-detecor. The signal from the detector is then fed back to the actuators to reposition the sample stage to maintain constant force between sample and cantilever. It is this signal from the photo-detector that is processed to give the AFM "image" of the surface.

The AFM can be operated in one of a few distinct modes. In contact mode, the tip is actually dragged across the surface of the sample. This mode can potentially provide the best resolution, but can also damage the sample and/or the tip. In non-contact mode, the cantilever is made to oscillate at its resonant frequency and the tip is maintained at some height above the sample surface. Tapping mode is a compromise of the two, enabling close contact for high resolution but not maintaining contact in a way that can cause damage. The cantilever is made to oscillate, but is kept closer than in non-contact mode so that the tip touches (taps) the surface, generally at a rate of 50 kHz - 500 kHz [23].

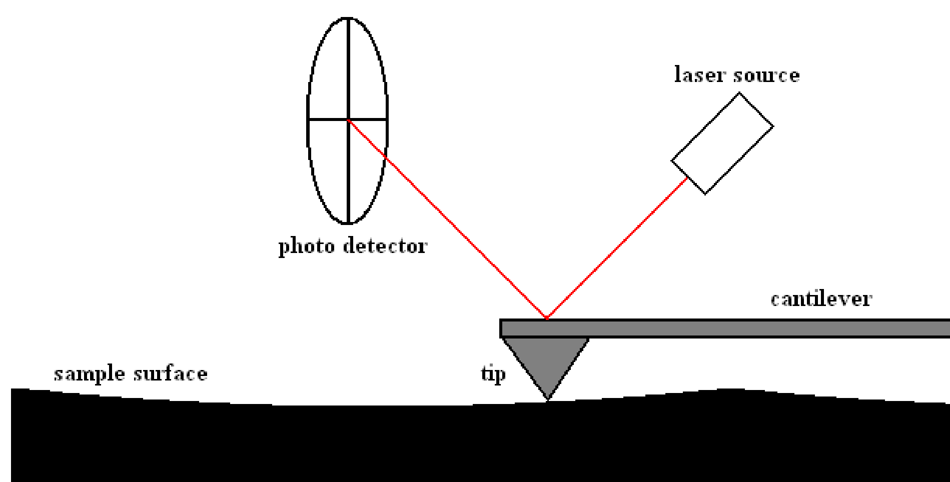

Figure 18. Atomic force microscope schematic

The relevance of atomic force microscopy to graphene research is that it can be used to measure the step heights of graphene samples on a substrate, thus determining the number of layers in the sample. It was found by Novoselov that graphene sheets are often folded upon themselves in a rather complex way, but that each overlapping sheet should contribute about 4 Å to the overall height (the interlayer spacing in bulk graphite is 3.35 Å). There is also a “dead layer” between the graphene and the SiO_2 that can be anywhere from 5 Å – 10 Å and has been attributed to water trapped under the film [1]. It has also been shown that the apparent height of a single layer of GO on an oxide

substrate is very close to 10 Å. Depending on the amount of absorbed water in a multilayer sample of GO, the distance between sheets can be anywhere from 6 Å to 12 Å [13].

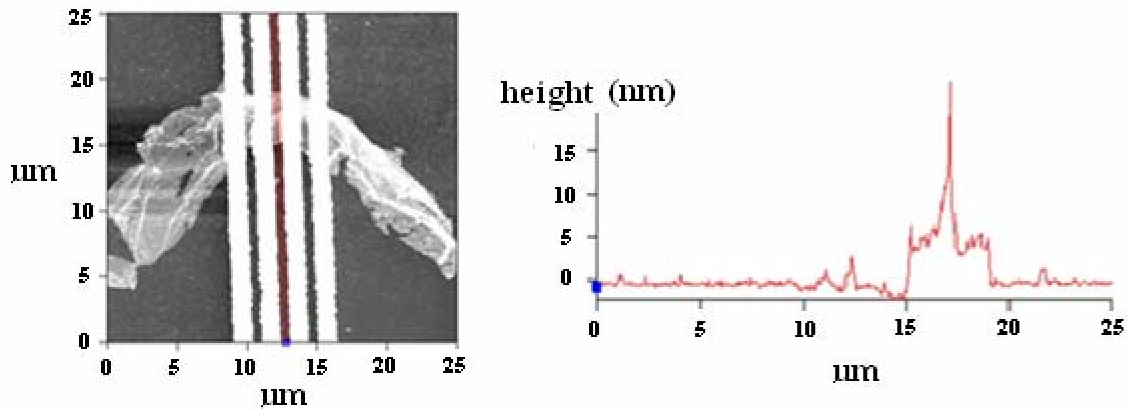

Figure 19. AFM image (left) and height profile (right) of GO flake

2.3.3 Raman Spectroscopy

Raman spectroscopy is the preferred technique for unambiguous determination of the number of layers in a graphene sample. This analytic technique involves irradiating the sample with light of a particular frequency and analyzing the light that is scattered. Within the material, each photon is absorbed and some of the energy is used to create or annihilate an optical (high energy) phonon (lattice vibration). The remainder of the energy is re-emitted as light of a different frequency so that energy is conserved:

$$\hbar\omega_{in} = \hbar\omega_{out} \pm E_{phonon}$$

The change in frequency is known as the “Raman shift” corresponding to (de)excitation of a phonon. When a phonon is created and the emitted photon is lower energy than the absorbed photon, it is called a “Stokes” process. Conversely, when a phonon is annihilated and the emitted photon is higher energy, it is called an “anti-Stokes” process. The Stokes process dominates at low temperatures, and at high temperatures the processes are equally likely.

The energies of phonons are quantized according to: $E = (n + 1/2)\hbar\omega$. In this equation, n is typically regarded as the number of photons present in the material vibrating at frequency ω. It needs to be emphasized that both n and ω have a functional dependence on k (the wavevector = $2\pi/\lambda$). The dependence of phonon frequency on wavevector, $\omega(k)$, is known as the dispersion relation and is a unique property of each material (much like bandstructure). The number of phonons existent at each frequency depends on the temperature:

$$n(k) = 1/(e^{\hbar\omega(k)/k_B T} - 1)$$

This is the Bose-Einstein distribution function, showing that phonons are not Fermions but Bosons.

The final key to Raman scattering theory is that momentum must be conserved in the process as well. Thus, the difference between the wavevectors of the incident and scattered photons must be equal to the wavevector of the phonon: $\overline{k}_{in} - \overline{k}_{out} = \overline{k}_{phonon}$. The overbars are included in the equation to emphasize that the wavevector is a true vector with both magnitude and direction. Knowing the wavevectors of the incident and scattered light (by employing the dispersion relation for electromagnetic radiation: $\omega=ck$, where c is the speed of light) enables one to determine the wavevector of the phonon [24].

Raman scattering results are often presented in the form of a graph with wavenumber on the x-axis (in units of cm^{-1}) and intensity on the y-axis (in arbitrary units). The wavenumber represents a frequency shift from that of the incident light that is sensed by a detector used to measure the intensity of the scattered light over a range of frequencies. Typically, peaks will appear at specific wavenumbers which can be characteristic of a specific material. Though not mathematically trivial, it can be seen that by knowing E and k for each allowed energy transition (peak on the intensity plot), the corresponding ω can be determined and the dispersion relation of the material, $\omega(k)$, mapped out.

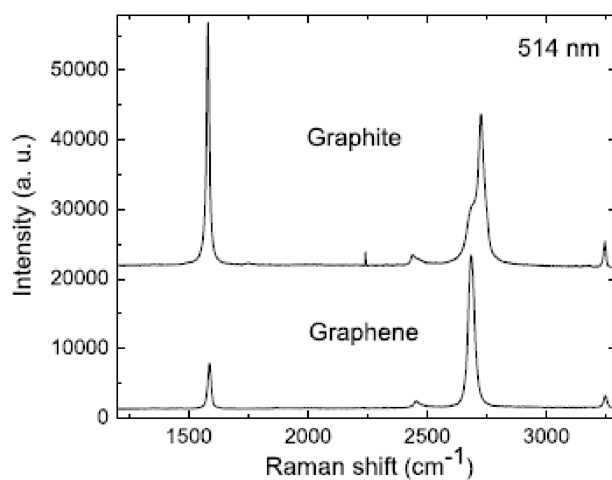

Figure 20. Comparison of Raman spectra in graphene and bulk graphite*

The first reports of Raman spectroscopy on graphene showed a distinct spectrum for each number of layers in the sample, up to five layers beyond which the spectrum is indistinguishable from bulk graphite. Bulk graphite shows three peaks of interest. The first peak at ~1350 cm^{-1} is called the "D" peak which arises due to defects such as a sample edge. The next peak of interest is called the "G" peak at 1580 cm^{-1} (the largest peak in bulk graphite) and the third peak at ~2700 cm^{-1} is called either the "G' "peak or the "2D" peak. It is this 2D peak that is of most interest for graphene research. Using an illuminating wavelength of 514 nm, it was found that the 2D peak is significantly larger and more sharply peaked for graphene than it is for bulk graphite and is also shifted to slightly lower wavenumbers (see Figure 20, in which the y-axis is scaled differently for the two samples, the intensity of the G peak actually being comparable in both) [54].

The full width at half maximum (FWHM) of the 2D peak has been found to be an excellent indicator of the number of layers in a graphene sample as it steadily increases from single layer graphene (~24 cm^{-1}) to bulk graphite (45-60 cm^{-1}) [55]. Figure 21 shows the detailed evolution of the 2D peak at ~2700 cm^{-1} (the Lorentzian curves

* Reprinted with permission from: Ferrari. Phys Rev Lett. **97**, 187401 (2006). Copyright 2006 by the American Physical Society

represent fundamental transitions and can be summed to give the overall Raman response). The illuminating radiation is 2.41 eV (515 nm). It should also be pointed out that the integrated intensity of the 2D line remains nearly constant with the number of layers [56].

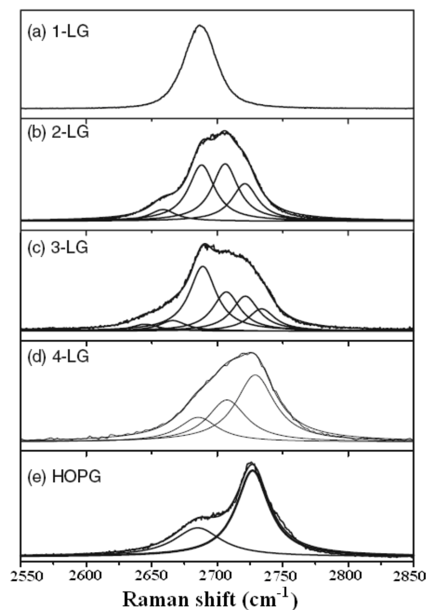

Figure 21. Detailed evolution of Raman 2D peak from graphene to bulk graphite*

2.4 Applications

This section reports on several proposed applications which take advantage of many of the unique electrical, mechanical, optical and thermal properties of graphene. The focus is on transistors, but sensor, resonator, capacitor and hydrogen storage applications are also discussed.

---

* Reprinted from: Physics Reports, **473**, Malard, "Raman Spectroscopy in Graphene" pp 51-87, Copyright (2009), with permission from Elsevier.

2.4.1 Transistors

It has been mentioned several times that the resistance of graphene can be modulated by an electric field (see Figure 9). This is the ambipolar field effect discussed by Novoselov in his seminal 2004 paper [1]. In this paper, he suggests that graphene may be a good material for transistor applications, citing its scalability, ballistic transport, linear I-V characteristics, and large sustainable current densities. He also points out that the high resistance (off) state is only about a factor of thirty times higher than the low resistance (on) state, not necessarily a good quality for transistor applications.

A transistor is essentially a three-terminal device such that the resistance between two of the terminals (source and drain) can be controlled by a voltage or current at the third terminal (gate). Historically, the most important types of transistors have been the bipolar junction transistor (BJT) and the metal oxide semiconductor field effect transistor (MOSFET). The MOSFET is a particular example of the more general FET family, which is distinguished by the "control" electrode capacitively affecting the amount of charge in a channel, and thus the channel's conductivity.

The two most important applications of a transistor are amplification and switching. Figure 22 shows the ideal characteristics of a MOSFET device. In generating these curves, the source would be grounded. It is seen that, in general, increasing the gate voltage increases the current through the device (the drain current). It is also apparent that for each value of gate voltage, there is a range of drain voltages over which the current increases linearly and there is also a range of drain voltages over which the current is saturated and does not change.

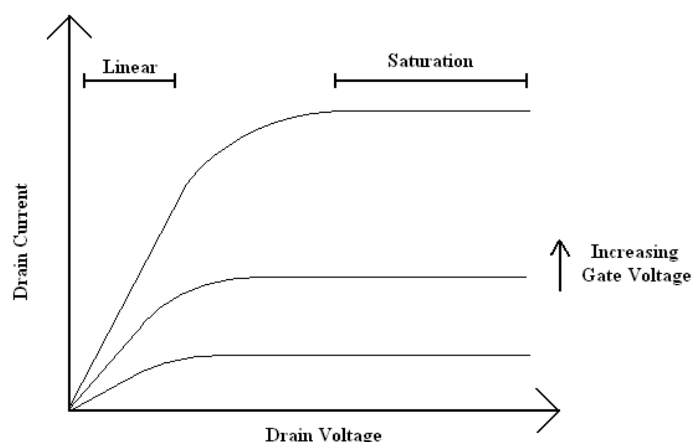

Figure 22. Ideal MOSFET output curves

When operated as an amplifier, a small DC gate bias is typically established and a large enough drain voltage is applied to put the device in the saturation regime: $V_D > V_G - V_T$ (where V_T is the threshold voltage necessary to establish the inversion layer in the channel). Now, when a small AC voltage is superposed on the gate bias, the drain current will follow the signal. If the amplitude of the signal is small enough, the response in drain current can be considered approximately linear. The change in drain current per unit change in gate voltage is known as the transconductance. A large transconductance is essential to large amplification.

When used for switching applications, the gate electrode is used to make the drain behave either as an open circuit (high resistance) or as a “short” circuit (low resistance). The drain resistance can be visualized as the inverse slope of the curves in Figure 22: $R_D = V_D / I_D$. The saturation region, where current does not change with voltage, is a region of essentially infinite resistance (off state). In contrast, in the linear region where a small increase in V_D gives a large increase in I_D, the channel displays a constant relatively low resistance (on state). It is these on and off states that are cleverly manipulated to produce the behavior demonstrated by logic gates, the basic building blocks of microprocessors and other digital electronic systems.

Some insight into the behavior of graphene-based field effect transistors (GFETs) can be obtained through the following very simplified analysis. It should first be pointed out that the original GFETs studied by the group of Novoselov used the "bottom gate" configuration in which the gate dielectric and control electrode both lie beneath the graphene channel. In these experiments, the dielectric was ~300 nm SiO_2 (for optical reasons, see Section 2.1.3) and the entire backside of the degenerately-doped Si substrate was the gate electrode. In more recent investigations, the "top-gate" geometry has been employed [46, 57]. This is preferable for several reasons, one being that multiple devices on a single substrate can be separately controlled by individual top gates rather than by a common bottom gate. This is necessary to interconnect GFETs and engineer more complicated circuits. Another advantage of top gates is that a wide variety of dielectrics can be used and the dielectric thickness is not constrained by considerations of graphene visibility. The group of Kedzierski, for example, has reported on experiments using top-gated GFETs with a 40 nm HfO_2 gate dielectric [57].

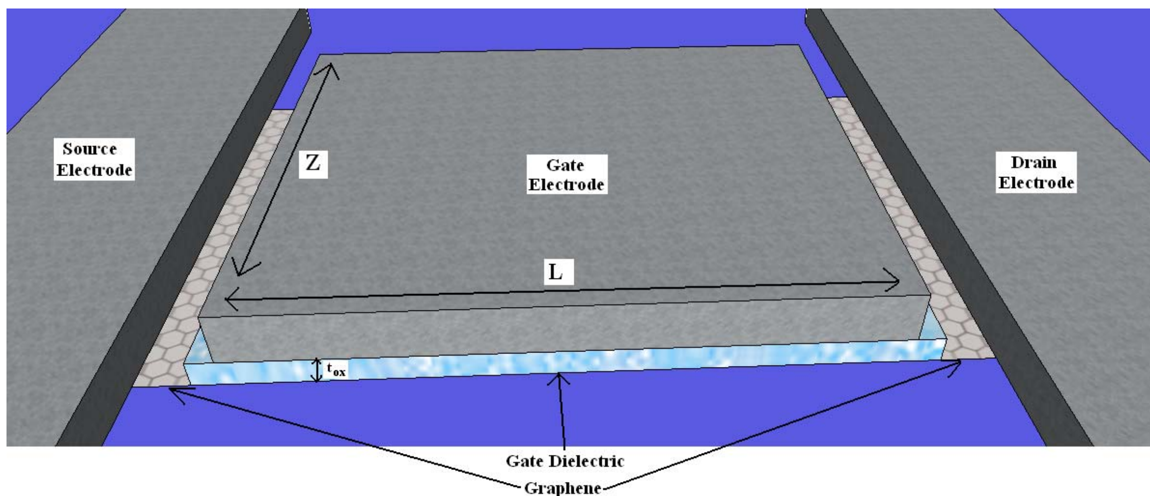

Figure 23. Top-gated GFET

The current in a GFET can modeled using the gradual channel approximation [58] to separate the effect of the gate bias (carrier generation) from that of the drain bias (drift field to which carriers respond). The basic equation from semiconductor theory for drift

current is: *J=qnv*. For graphene, a two-dimensional material, we consider *n* to represent an areal carrier density induced by the gate electrode and *v* to be the velocity of the carriers in response to the drain voltage (*q* is the charge of an electron). The current density, *J*, must be scaled by the width of the channel, *Z*, to give the total drain current.

In general, each quantity can be a function of position along the channel and the total current will be given by the following integral:

$$I_D = \frac{Z}{L}\int_0^L qn(x)v(x)dx$$

To a first approximation, we can consider the carrier density to be constant and given by: $n = V_G \varepsilon_0 \varepsilon_{ox} / qt_{ox} = V_G C_{ox} / q$ (see Section 2.1.3). We can also assume a constant mobility (μ) relating carrier velocity to electric field: $v = V_D \mu / L$. Substitution into and evaluation of the integral above yields:

$$I_D = \frac{Z}{L}\mu C_{ox} V_G V_D$$

This model predicts an output conductance ($\partial I_D / \partial V_D$) that is proportional to gate voltage (which is clearly seen in Figure 9). It is obvious that this model doesn't capture all GFET behavior, however, as it predicts zero output conductance with zero gate bias. We have seen already that the conductivity of graphene cannot fall below the minimum value of $4q^2/h$ (~154 μS) which occurs at the charge neutral level (Section 2.1.3). This is the origin of the poor on/off ratio pointed out by Novoselov. The key to obtaining a better resistance ratio in GFETs is to engineer a bandgap in the material. This can be done either by using bilayer graphene with its electrically tunable bandgap, or by using graphene nanoribbons (see Section 2.1.4). GFETs using GNR less than 10 nm wide have demonstrated on/off ratios as high as 10^6 at room temperature [59].

This section will close with some data by Kedzierski showing typical GFET behavior. In Figure 24, we see the general features of the model derived in this section to be correct. In Figure 24A, it is apparent that drain current increases with both gate voltage and drain voltage. Figure 24B clearly shows that increasing the *Z/L* ratio of the

device increases the drain current (*W* on the graph is equivalent to *Z*). Two further observations can be made regarding the graphs, the first being that the locations of minimum current (the Dirac voltages) are shifted only slightly from zero volts, indicating a small amount of doping (p-type). The second observation is that the curves are not quite symmetric, indicating a small difference in carrier mobilities. In fact, these mobilities can be estimated form the slope of the I_D-V_G curves:

$$\mu_n = (\partial I_D / \partial V_G) * (\frac{L}{ZC_{ox}V_D}) \quad ; \text{ for } V_g > V_{Dirac}$$

$$\mu_p = (\partial I_D / \partial V_G) * (\frac{L}{ZC_{ox}V_D}) \quad ; \text{ for } V_g < V_{Dirac}$$

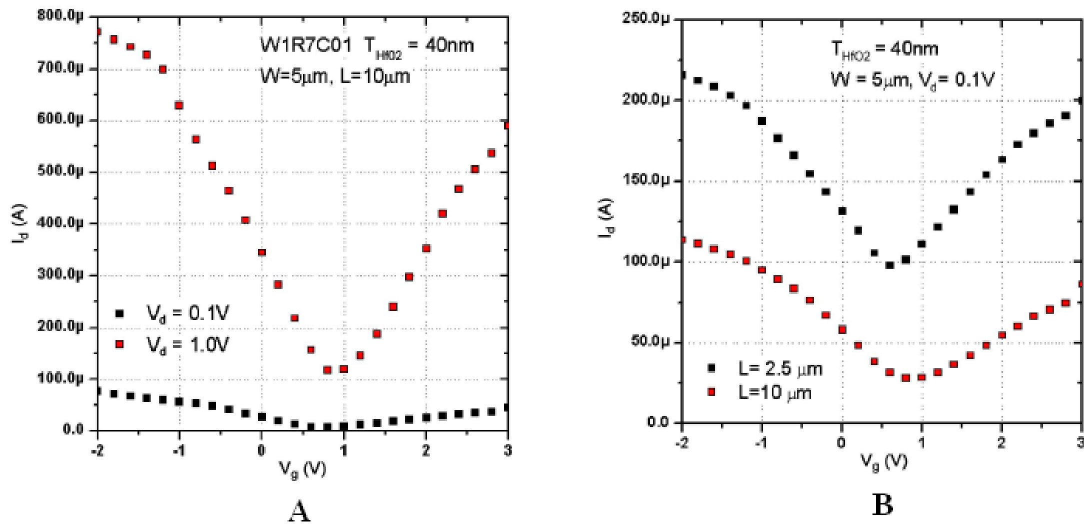

Figure 24. Typical GFET behavior*

* Reprinted from: Kedzierski. IEEE Electron Device Letters. **30**, 745 (2009). © 2009 IEEE.

2.4.2 Sensors

Graphene has been shown to be a useful material for a variety of sensing applications, two of which are gas sensors and magnetic field sensors. As a gas sensor, the graphene has been shown to be capable of detecting individual gas molecules as they impinge upon the material, either donating or accepting an electron and thus changing the sensor's conductivity [60]. Several types of gasses were investigated and it was found that NO_2, H_2O, and iodine acted as electron acceptors, while NH_3 and CO were electron donors. Factors contributing to graphene's exceptional sensitivity include a surface-to-volume ratio of essentially unity and very low levels of defect-related noise.

Figure 25 shows the change in resistivity of a sample of graphene as it is exposed to a variety of gasses. Initially, the sample is under vacuum. At time zero, it is exposed to a 1 ppm concentration of each of the gasses studied. After about 500 seconds, the gasses are evacuated and it is seen that the change in resistivity persists when no gasses are present. The fourth region of the graph shows that the initial resistivity can be recovered by annealing in vacuum at 150 °C.

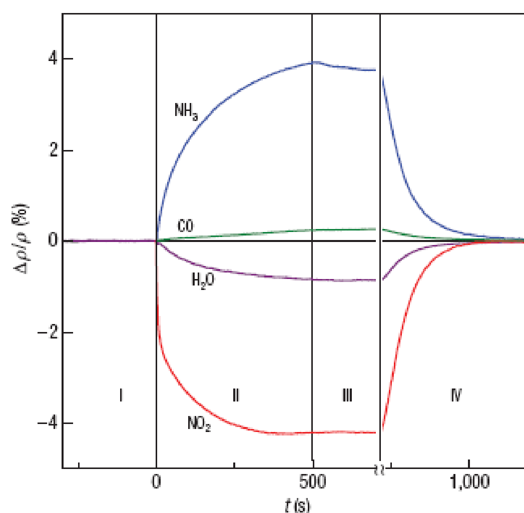

Figure 25. Resistivity change in graphene upon exposure to various gasses*

* Reprinted by permission from Macmillan Publishers Ltd: Schedin. Nature Materials. **6**, 652 (2007). Copyright 2007.

It should be pointed out that in all cases the change in resistivity is negative upon exposure to the gasses, as the number of carriers in the sample is always increased. The polarity in the graph is meant to distinguish electron-doping donor gasses (positive $\Delta\rho$) from hole-doping acceptor gasses (negative $\Delta\rho$).

First-principles calculations using density functional theory have been performed to study the energetics of gaseous adsorption on a layer of graphene [61]. Three different adsorption sites were considered: directly atop a carbon atom, at the center of a carbon hexagon, and at the center of a carbon-carbon bond. Also, for each type of gas molecule (H_2O, NH_3, CO, NO_2, and NO) several orientations of the molecule on the graphene surface were considered. For each orientation of each molecule, the calculated adsorption energy and the amount of charge transferred to the graphene sheet from the molecule were reported.

The results of the theoretical work correlate very nicely with the experimental results of the Schedin group. For example, the most stable orientation of H_2O (one O-H bond parallel to surface and the other bond pointing at surface) was found to produce an electron transfer of 0.025 e^-/molecule from graphene to the H_2O molecule, making it an acceptor gas. NO_2 is also theoretically shown to be an acceptor gas with an electron transfer of 0.099 e^-/molecule, making it a stronger acceptor than H_2O. This is experimentally confirmed in Figure 25. The calculations also correctly predict both NH_3 and CO to be donor gasses, though it predicts a surprisingly small amount of electron transfer from NH_3 to graphene when compared to empirical data.

The remainder of this section will be dedicated to magnetic field sensors. The principles behind magnetic field sensing (GMR) have already been discussed in some detail in Section 2.1.3. Though yet to be realized in practice, graphene-based spin valve sensors could someday be incorporated as read-elements in memory devices, perhaps enabling higher-density storage and faster operation than currently available.

The diagram of a conventional spin valve sensor is shown in Figure 26. It consists of two ferromagnetic (FM) layers, one of which is free to align with ambient magnetic

fields. The other ferromagnetic layer has its magnetization pinned in a particular direction due to coupling with an adjacent anti-ferromagnetic (AF) layer [62]. The resistance of the structure depends on the angle between the magnetizations of the free and pinned layers (which are separated by a non-magnetic (NM) conductive spacer layer such as copper):

$$\Delta R \propto -\cos(\theta_1 - \theta_2) \propto -\sin\theta_1$$

The easy axis of the free magnetic layer is oriented perpendicular to the pinned layer's magnetization so that zero applied field corresponds to a state of high resistance. As an external field is applied (in the y-direction) the magnetization of the free layer rotates towards the pinned layer and the resistance of the structure decreases.

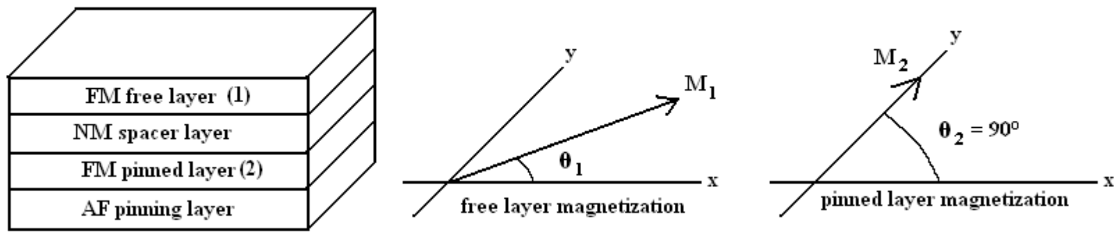

Figure 26. Conventional spin valve sensor

The response of the free layer can be analyzed be considering the interplay of two energies. The anisotropy energy wants to keep the magnetization in the x-direction and is of the form: $K*\sin^2\theta_1$ (where K is a function of the physical dimensions of the free layer). On the other hand, the Zeeman energy wants to align the magnetization (M) with the applied field (H) and has the form: $-M*H*\cos(90°-\theta_1)$. The total energy is given by the sum of these terms and the resulting angle of magnetization corresponds to the minimum energy state. This is found by differentiating energy with respect to angle and setting the result equal to zero:

$$E = K\sin^2\theta + \mu MH\sin\theta$$
$$\partial E/\partial\theta = 2K\sin\theta\cos\theta + \mu MH\cos\theta = 0$$
$$\sin\theta = -\mu MH/2K \propto H$$

Combining this with the previous result ($\Delta R \propto \sin\theta$) we see that the change in resistance scales linearly with the magnitude of the applied magnetic field (*H*). The response is only linear for rather small fields, however, because the resistance eventually saturates as the free and pinned layers are aligned parallel to one another (see Figure 27).

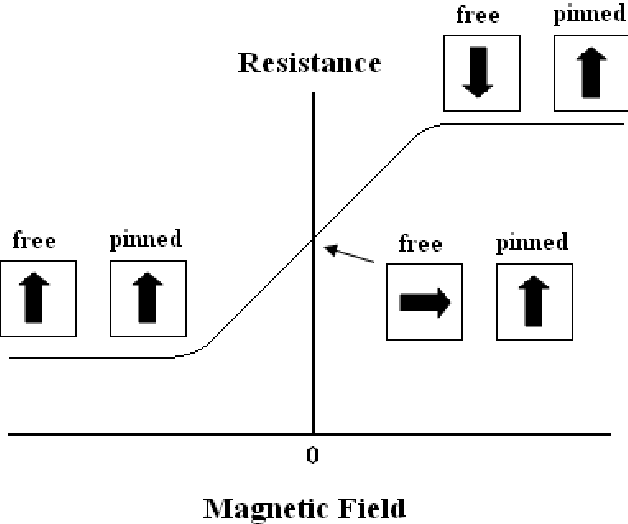

Figure 27. Resistance of spin valve sensor vs. magnetic field

Graphene-based spin valve sensors would operate in an analogous manner to conventional spin-valve sensors, with graphene playing the role of the spacer material between two magnetic contacts. Perhaps the biggest advantages of graphene devices would be scalability and a potentially simpler fabrication process than the complex layering of materials required in conventional spin valve stacks.

2.4.3 Transparent Conductors (Solar Cells)

Another application that takes advantage of the unique characteristics of graphene uses the material as a transparent conductor in new solar cell designs. Both graphenes obtained by reduction of GO [28] and those obtained by CVD growth [63] were studied for this application. Before discussing these results, the general form and function of a

solar cell will briefly be reviewed so that the significance of the results can be best understood.

The basis of a modern solar-cell is simply a p-n junction diode connected across a resistive load. When the diode is exposed to light, photo-generation of carriers occurs both in the bulk semiconductor regions and in the depletion region. The electric field that exists in the depletion region sweeps excess carriers out of this region (drift) where they diffuse to the edges of the device and out through the load. This is referred to as the photocurrent [64].

Important considerations for solar cell design include the size of the bandgap of the semiconductor material employed. Light of wavelengths longer than E_G / hc will not be absorbed, and will not contribute to the photocurrent (h is Planck's constant and c is the speed of light). On the other hand, the maximum voltage that can be generated with the solar cell is limited to the bandgap of the material. Another important consideration, and the one that is relevant to graphene, is the series resistance of the photocell device. By reducing series resistance, the amount of power that can be delivered to the load is increased.

One source of series resistance is the bulk semiconductor material and can be minimized by heavy doping. Another source is actually the metal contact on the "top" side that is exposed to light. A trade-off in design must occur. Since the contact is not perfectly transparent, it will absorb some of the light, reducing efficiency. This makes it desirable to reduce contact area. However, a smaller top contact area translates into a larger contribution to the series resistance. The compromise in geometry typically involves using a set of optimally-spaced contact "fingers" (see Figure 28). Another balance exists in the choice of conductor material itself. The desired characteristics of high transmittance and low resistance have historically been supplied by materials such as indium-tin-oxide (ITO). It has been shown that graphene has the potential to be a low-cost alternative to ITO for such an application.

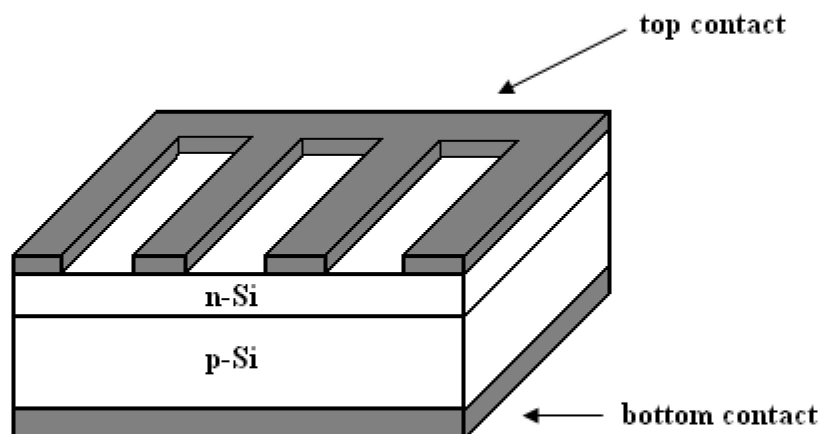

Figure 28. Basic solar cell design

Studying continuous films of overlapping thermally-reduced GO films, the group of X. Wang [28] found that films of approximately 10 nm thickness displayed a conductivity of 550 S/cm (sheet resistance ~ 1.8 kΩ/square) with a transparency of 70 % over the near infrared range. The transparency of GO films is compared to that of ITO and another common electrode material, fluorine-tin-oxide (FTO), in Figure 29.

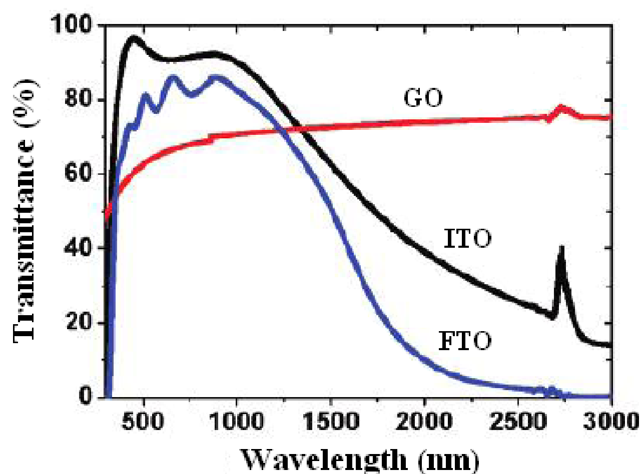

Figure 29. Transmittance of various solar cell electrode materials*

---

* Reprinted with permission from: Wang. Nano Lett. **8**, 323 (2008). Copyright 2008 American Chemical Society.

It can be seen that the transmittance of GO films is superior for wavelengths above about 1500 nm. For overall comparison, the conductance of ITO is 1000 S/cm - 5000 S/cm [65] while that of FTO can range from 0.05 S/cm - 100 S/cm [66]. While ITO has higher conductivity and better transmission in the visible range, advantages of graphene include lower cost, higher mechanical strength and flexibility, and better chemical stability.

Studying graphene obtained by chemical vapor deposition on nickel, the group of Y. Wang [63] saw even higher conductivity than possessed by graphene obtained from GO. They reported sheet resistances from 1350 Ω/square - 210 Ω/square and transmittance from 72 % - 91 % in the visible frequency.

2.4.4 Supercapacitors

Yet another application that takes advantage of the unique properties of graphene leverages its large surface area (2630 m^2/g including both sides) to produce capacitors with extremely large energy densities [67]. These graphene-based supercapacitors (or ultracapacitors) have been shown to possess energy densities of 28.5 W-hr/kg and specific capacitances in excess of 200 F/g [68]. In both experiments cited, chemically reduced GO was used as the supercapacitor electrode material.

Supercapacitors are based on a somewhat different design than ordinary dielectric capacitors and are often referred to as electrochemical double-layer capacitors (EDLCs). The operating principle behind a supercapacitor is charge separation at the interface between electrode and electrolyte. The two electrodes are separated by an electrolyte and an ion-permeable barrier. The overall structure can thus be analyzed as two capacitors in series, although due to the large surface area and small separation of charge the resulting capacitance is quite large.

Technologically, supercapacitors fill the application niche between dielectric capacitors and batteries (electrochemical cells). They are able to store larger amounts of charge than conventional dielectric capacitors (though not as much as batteries) and are able to deliver their stored power much more quickly than batteries (though not as

quickly as conventional capacitors). One example of an application for supercapacitors is a backup system that can provide power during the time between a failure and the time when a more permanent backup can be employed (such as a generator).

In graphene-based EDLCs, the large surface area results from the intricate folding and overlapping of the GO sheets. In both studies cited, the electrolyte used was an aqueous solution of KOH. Though not quite able to match the performance of porous-carbon-based supercapacitors (~250 F/g) graphene-based EDLCs are projected to have technological value for several reasons, the first and most important being the lower cost of the starting material and process used to create GO as compared to porous carbon. Other advantages over the porous carbon design include lower resistivity of GO and better chemical stability [69].

2.4.5 Other Applications

To conclude this section, a few more applications proposed for graphene will briefly be discussed: electro-mechanical resonators, hydrogen storage, and heat sinks.

Graphene resonators have been fabricated by mechanical exfoliation over trenches etched into SiO_2. It has been suggested that graphene-based resonators could be used as yet another type of sensor. Similar to a crystal-oscillator rate monitor used in thin-film depositions, graphene-based oscillators could be used for extremely sensitive mass detection and force detection, as impinging molecules would result in measurable changes in the structure’s resonant frequency [70].

Hydrogen storage is to be accomplished using exfoliated GO (unreduced). Recall that graphite oxide contains epoxy groups (oxygen atoms bonded to two carbon atoms, see Figure 14). The idea is to introduce titanium atoms, which the oxygen atoms will break a bond with carbon in order to join with. Each titanium atom joined to the structure can then bond with several hydrogen molecules. The high surface area of GO discussed in the previous section is a major benefit for this application as well. The requirement for this application is that the energy required to remove the hydrogen is less than the energy required to break any link of the chain of bonds (C-O-Ti) holding it to the graphene

“backbone”. Calculations have suggested this to be the case. The upper limit of hydrogen that can be stored using this technique has been found to be 4.9 wt% [71]. The hydrogen could later be liberated as needed by some expenditure of energy, the use of which would be justified by the fact that the hydrogen was able to be stored and transported in a non-explosive state.

The final application for graphene that will be discussed in this thesis is its proposed use as a heat sink material in integrated circuits. We have seen in section 2.1.3 that graphene possesses an extremely high thermal conductivity at 3000-5000 W/m-K. This means that if two ends of a sheet of graphene are held at different temperatures, a large amount of energy will flow through the material. This principle can be used to remove excess heat from modern ultrasmall and ultrafast integrated circuits. Simulations have been performed which suggest that the incorporation of a graphene layer can reduce the maximum temperatures of hot spots on a microchip by up to 70 K [72].

3 Materials and Methods

In the course of this experimental work, several advanced scientific techniques had to learned and mastered. This chapter explains those techniques in detail. The information is divided into methods related to sample processing and fabrication and those related to measurement and characterization. As each technique is introduced, its relevance to the overall experimental design will be made manifest.

3.1 Fabrication Techniques

The organization of this chapter follows the sequence of processing steps used to prepare samples for study. The first process that is outlined is the thermal oxidation of silicon. Secondly, details of the processing of GO into solution are given, as are methods for its deposition onto substrates. (The synthesis of the starting graphite oxide was performed by graduate student Sean Smith. His procedure is given in Appendix A). In the third section, lithography is explained in detail. This includes both general theory and the specific operation of both the Heidelberg DWL laser lithography system and the Karl Suss MJB3 manual aligner. Next, various methods of thin film deposition are explored, the focus being on sputtering and thermal evaporation. The final topic treated is wirebonding.

3.1.1 Thermal Oxidation of Silicon

It has been observed that graphene becomes visible when placed on a substrate of silicon with 300 nm oxide (see Section 2.1.3). The first step in the fabrication of all samples studied was the thermal oxidation of silicon wafers. The mathematical model for silicon oxidation was worked out by Deal and Grove in 1965 [73]. In their model, the incoming flux of oxygen (O_2 if a “wet” oxidation, and H_2O vapor if “dry”) must diffuse through any layer of SiO_2 already present in order to reach the silicon surface and react to form more oxide. This leads to a reduced reaction rate as oxidation proceeds. The following formula has been derived which relates oxide thickness to time:

$$X_{ox}^{2} + AX_{ox} = B(t + \tau)$$

In the equation above, A and B depend on the temperature and pressure of oxidation, the nature of the oxidation (wet or dry), the crystallographic orientation of the silicon substrate, and also the type and density of dopants in the substrate. Also, τ represents the time that would have been required to grow any oxide already present (if, for example, a wafer were re-oxidized).

In this research project, the substrates used were n-type 125 mm wafers with resistivity of 0.003-0.007 Ω-cm (doping $5*10^{18}$ - $2*10^{19}$ cm^{-3}). The Lindberg tube furnace located in Owen 433 was used for the oxidations. Wet oxidations were performed, introducing water vapor into the tube by bubbling oxygen gas through a beaker of water heated to 95 °C. The temperature of the oxidations was chosen to be 1100 °C. For these parameters, the Deal-Grove equation gives an expected growth time of 14.5 minutes for 3000 Å oxide. Experimentally, it was found that the required oxidation time was closer to 17.5 minutes.

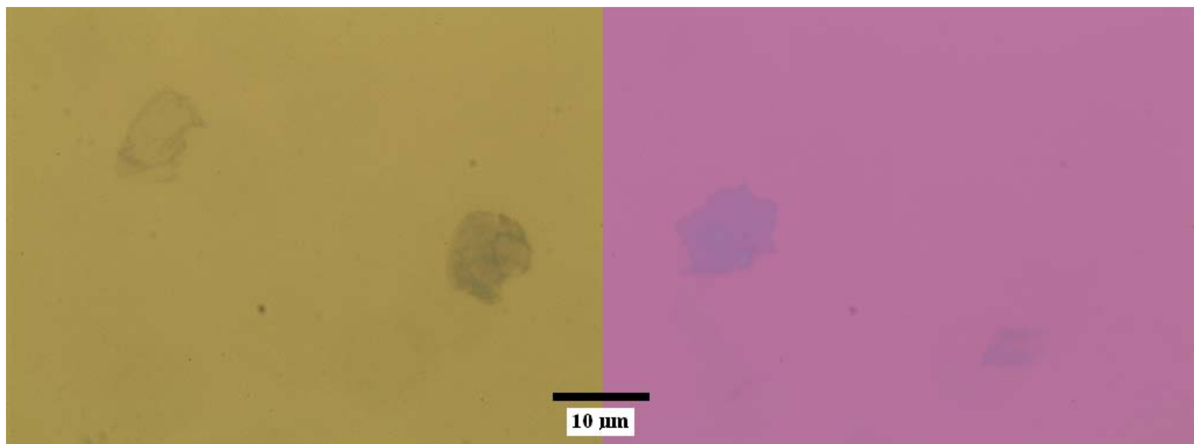

Figure 30. GO flakes on 90 nm SiO_2 (left) and on 300 nm SiO_2 (right)

Substrates oxidized to 90 nm were also fabricated (1050 °C for 6 minutes). It was mentioned earlier that graphene should show good contrast on oxide of this thickness as

well. GO particles were found to be about equally visible on either substrate, with perhaps more texture being seen in the samples atop the 90 nm oxide (see Figure 30). The 90 nm oxide also has the advantage of quicker processing.

The thicknesses of the oxides were determined using a Nanospec® tool also located in the Owen 433 cleanroom. The tool is an optical-based system that can measure a variety of films on different substrates. It operates by the principle of spectroscopic reflectometry in which the reflectance of the sample is measured over a range of frequencies in the optical range. If the optical constants associated with each material are known, the film thickness can be calculated. A silicon wafer recently dipped in HF is used as a zero-oxide reference.

3.1.2 GO Solution Processing

The result of the oxidation of bulk graphite is referred to as "GO paper" (see Appendix A). It is a black, lustrous material obtained by peeling the final dried oxidation product from a filter.

Figure 31. GO Paper

In this experiment, 100 mg of GO paper was dispersed in 1 L de-ionized H_2O (18.2 MΩ) by constant stirring at 350 rpm for 30 days. After this time, the solution was dark black and had visibly large particles suspended in it. However, after being allowed

to settle for a day with no stirring, the large particles sank to the bottom, and a light-brown homogeneous suspension of dispersed GO platelets was skimmed from the top and placed in a plastic push-top spray bottle (see Figure 32).

Figure 32. One Liter of dispersed GO (left) and 2 oz spray bottle (right)

This solution was sprayed onto oxidized silicon substrates heated to 225 °C. Graphite oxide is hydrophilic so that if a large droplet of water were placed on the heated substrate, the GO platelets would become concentrated as the droplet evaporated. The result would be a very thick agglomeration of GO particles, not the single sheets desired for this study. By exposing the substrate to a fine mist, each tiny droplet comprising the mist evaporates individually and forms a distribution of single and few-layer GO platelets over the surface of the oxide.

It was found that three sprays from about six inches away and at an angle of perhaps forty-five degrees gave acceptable results. The technique is sometimes referred to as “spray-and-pray”. In the next processing step, a large number of metal four-point contact structures are deposited with the hope that one of them will land atop and make electrical contact to a suitable platelet of GO, which can then be measured by

wirebonding the microstructure to macroscopic contact pads (this will be explained in the following sections).

The point is that a consistent spray-coating process is not needed because the random nature of the GO distribution is made up for by the large number of contact structures fabricated. The only requirements of the spray process are that it keeps the platelets separated enough so that significant overlap does not occur, yet they must also not be so dilute that there becomes a very small probability of finding a platelet suitably situated with respect to a contact structure (i.e., spanning all four electrodes).

3.1.3 Photolithography

After spray-deposition of GO, the process of lithography was begun. Each sample was spin-coated with photoresist (4000 rpm for 30 seconds), then placed on a 85 °C hot plate for two minutes. Using Microposit S1805 photoresist, these spin parameters consistently yielded resist thicknesses from 500 nm - 600 nm as measured by the Nanospec® tool (see section 3.1.1). The resist was patterned using a Karl Suss MJB3 manual aligner. Before discussing this technique, however, the theory of lithography will be reviewed.

Photoresists have been used to make printed circuit boards since the 1920s and have since become an integral part of semiconductor processing [74]. In general, there are two types of photoresist: positive and negative. The resist used in this experiment was a positive resist. When a positive resist is exposed to light of certain wavelengths (high enough energy photons), it undergoes a chemical decomposition. By selectively exposing certain regions of photoresist to light, those regions can be rendered soluble and subsequently rinsed away by a solution known as “developer”. Microposit 351 developer was used in this experiment (Microposit products are distributed by the Shipley Company). It consists of water, sodium hydroxide, and sodium tetraborate decahydrate.

By selectively exposing and subsequently removing predetermined regions of the film, a pattern is transferred into the photoresist. This patterned resist can serve many functions (serving as a barrier against many acids, for example). Selected areas of a metal

layer can be dissolved by the acid while the regions covered by photoresist remain, forming structures. Once the metal has been patterned, the resist has served its purpose and can be removed by rinsing with acetone (see Figure 33).

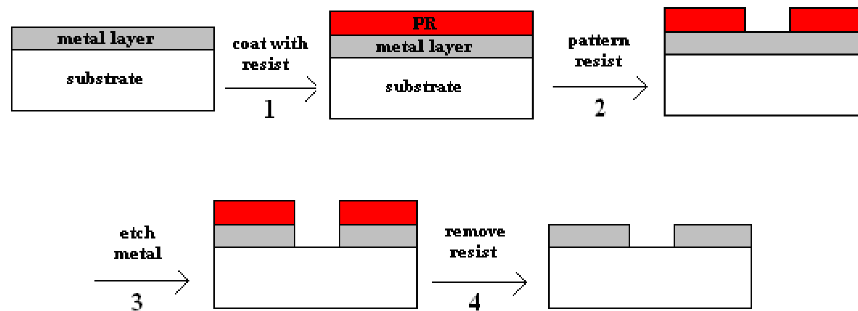

Figure 33. Photoresist used in "wet-etch" process to pattern metal layer

Negative resists are chemically just the opposite of positive resists, although they serve the same functions once they are patterned. Negative resists are normally soluble in developer, but regions that are exposed to light undergo a process known as "cross-linking" in which a three-dimensional network of molecules is formed. It is these regions that will remain when the sample is washed in developer solution.

When working with any type of photoresist, care must be taken to expose only the desired areas with photons possessing enough energy to cause the desired chemical transformation. Practically, this requires ultraviolet filters over the fluorescent lights in any room in which photolithography occurs, rendering the area in an eerie yellow hue. Without the filters, though, the entire sample would be exposed at once and there would be no way to form a pattern. To selectively expose only certain regions of photoresist to high-energy photons, two techniques are commonly used: mask exposure and direct laser writing.

The first technique used to selectively expose photoresist is exposure through a mask consisting of the desired pattern formed of a reflective metal (such as chrome) on a glass plate. A photoresist-coated substrate is placed in contact with the mask and a UV

source is shined through the mask so that the resist covered only by glass is exposed to the light, while the regions that are shielded by the reflective metal pattern are not exposed. This is the method of the Karl Suss manual aligner, which consists of a mask holder and a platform stage that the user can manipulate to position samples very accurately beneath a mask (using a microscope if necessary). A shutter can be made to open for a predefined length of time (typically 4-8 seconds), allowing ultraviolet light from a mercury lamp (emission peaks at 365 nm and at 405 nm) to pass through the mask, selectively exposing the photoresist beneath.

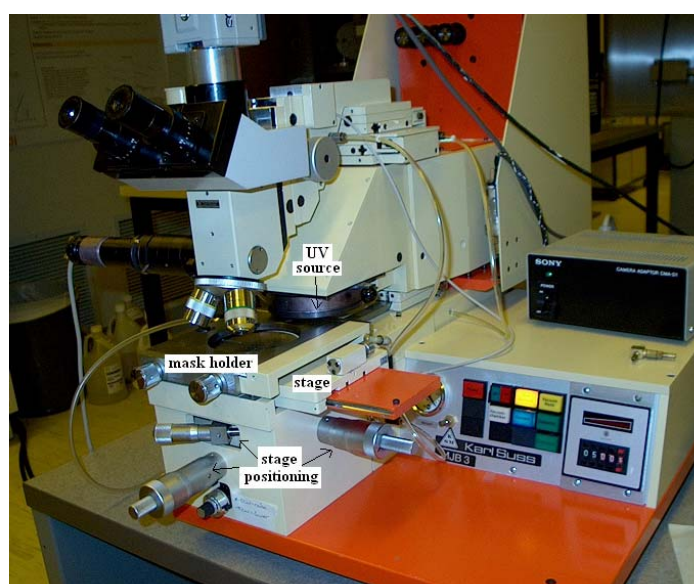

Figure 34. Karl Suss manual aligner

For features larger than about 10 microns, masks can be fabricated by printing the pattern in ink on transparent mylar. For smaller features, however, masks must be generated using a laser lithography tool such as the Heidelberg DWL (Direct Write Laser) system. With a tool such as this, a design can be drawn on a computer using any number of software programs such as Cadence, AutoCAD, Kic, or LayoutEditor. The design can then be saved in a number of formats (the following types being compatible with the Heidelberg system: GDSII, DXF, GERBER, and CIF) and loaded into a computer that controls the DWL stage. A mask blank consisting of glass with a thin

coating of chrome topped by a layer of photoresist (~500 nm) is placed on the stage and the computer coordinates the stage's motion beneath a stationary diode laser (405 nm wavelength).

Depending on the size and complexity of the design, the pattern may take from a few minutes to several hours to transfer to the photoresist (it should be noted that the minimum feature size attainable with the DWL is 600 nm). Once the photoresist has been selectively exposed by controlled movement under a laser, the exposed resist can be removed by soaking the mask in a developer solution. Next, the mask is soaked in an acid that dissolves chrome. This removes the chrome that is now exposed, while the chrome that is still covered by photoresist remains intact. Finally, the remaining resist is removed with acetone (the details of DWL operation and mask fabrication are given in Appendix B). This mask can then be used with the Karl Suss manual aligner to pattern resist-covered samples. It should be noted that mask fabrication using the DWL essentially follows the process described in Figure 33 with the substrate being glass, the metal layer being chrome, and the PR being already applied when the mask blanks are purchased.

Alternatively, samples can be placed directly in the DWL and the resist can be patterned by laser without ever having to fabricate a mask or use the manual aligner. In general, if multiple substrates must be patterned with the same design, it is more efficient to use the DWL only once to make a mask and then use the manual aligner to replicate the design. Otherwise, the only reason to use the DWL to directly pattern resist on a substrate would be to align a layer to a pre-existing layer with accuracy better than can be achieved using a manual aligner.

Once the photoresist had been exposed, the sample is placed in a dish of Microsposit 351 developer (mixed with four parts DI water) and gently agitated for an amount of time dependent on photoresist thickness, exposure time, and exposure energy. It was found that only 2-3 seconds in the developer were required with the S1805 resist and an exposure time of four seconds. The sample is then rinsed thoroughly with DI water and placed on a 85 °C hot plate for five minutes. The remainder of this sub-section will describe the structures fabricated.

To measure the resistivity of GO as it is being thermally reduced, it is necessary to establish electrical contact to the sample at four collinear points. By sourcing a current through the outer two electrodes, and measuring the voltage that is developed across the inner two electrodes, the effect of contact and probe resistance can be eliminated and an accurate measure of the resistance of the sample can be obtained [23].

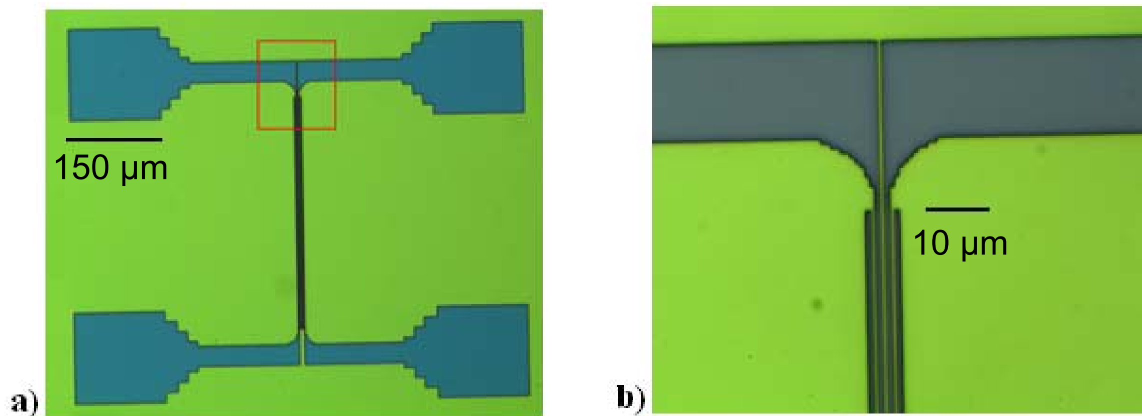

Figure 35. Photoresist patterned for four-point resistance structure

Figure 35a shows one complete contact resistance measurement structure. The yellow areas are photoresist and the purple is the substrate showing where photoresist has been removed. The four large areas in each corner are 150 microns on each side. Each of these four areas is wirebonded to one of several large contact regions around the sample's perimeter. Silver epoxy and a short length of radio wire is then used to create electrical contact from the perimeter pads to the measuring device (this process will be made more clear in Section 3.1.5 and an alternative method of establishing contact will be introduced which does not require wirebonding).

In the middle are four very thin electrodes, each connected to one of the larger regions. Figure 35b is a close-up of the region enclosed by the red box in the first figure. In it, the structure of the four electrodes can be seen. Ideally, the lines would each be one micron wide with a one micron space between lines. However, as a result of slight overdeveloping, it can be seen that the lines are a bit wider than the spaces.

3.1.4 Thin Film Deposition

A variety of techniques have been developed by which to create thin layers of one type of material atop another. Two examples have been introduced in this section: spray deposition of GO solution, and spin coating of photoresist. In semiconductor device processing, it is common to fabricate thin metal films to serve as contacts and interconnects. It is also common to fabricate thin insulating films to provide device isolation as well as perform specific device functions (such as a MOSFET gate oxide, for example). Insulators are typically deposited using some type of chemical vapor deposition (CVD) process, in which a gaseous precursor chemically reacts with the surface to cause film growth. In contrast, most metals are deposited by some type of physical vapor deposition (PVD) process, in which a film grows by condensation of a gaseous material. No chemical change occurs at the surface (only a change of phase).

For this research project, thin metal films of two different types were deposited. For the four-point resistivity structures, a thin layer of gold (~100 nm) topping an even thinner layer of chromium (~5 nm) was used. This was done by dual-source thermal evaporation, using the evaporator in the physics lab (Weniger room 487). An operating procedure for this tool is included as Appendix C. Gold was preferred for its low resistivity and excellent stability. Chromium was included as an adhesion layer to help the gold stick to the substrate.

Additionally, independently switchable magnetic contacts were fabricated of a nickel-iron alloy (80 % - 20 %) known as Permalloy. This material was chosen for its low crystalline anisotropy and magnetostriction and was sputter deposited (to a thickness of ~100 nm) using the AJA brand ATC Orion system located at the ONAMI facility in Corvallis. An operating procedure for the sputter tool is included as Appendix D as are experimental deposition rates.

Thermal evaporation will be discussed first. It must be pointed out, however, that nearly all thin-film deposition techniques occur at significantly reduced pressures. This is necessary for several reasons, the most important being to ensure the purity of the

deposited film. Typically, some sort of vacuum pump must be used to evacuate the interior of a stainless steel chamber where the deposition occurs. The thermal evaporator employed in this project maintains high vacuum (~10^{-6} Torr - 10^{-7} Torr) with a diffusion pump. Within such a pump is a special type of oil that is heated, creating a vapor. The oil vapor rises a short distance but is then cooled, so that it falls and re-condenses. As it does so, it traps some of the air molecules in the chamber and effectively removes them. The exhaust end of a diffusion pump (diff pump) cannot be exposed to atmospheric pressures, however, and needs a second pump to "back" it. This secondary pump is a mechanical rotary-type unit that cannot produce such low pressures as a diff pump, but is used to bring the chamber to a low enough pressure that the diff pump can take over. The reason for this is that diffusion pumps cannot operate with either end exposed to atmospheric pressure, but must have the chamber "roughed" down to ~10^{-4}-10^{-5} Torr before they are of any use.

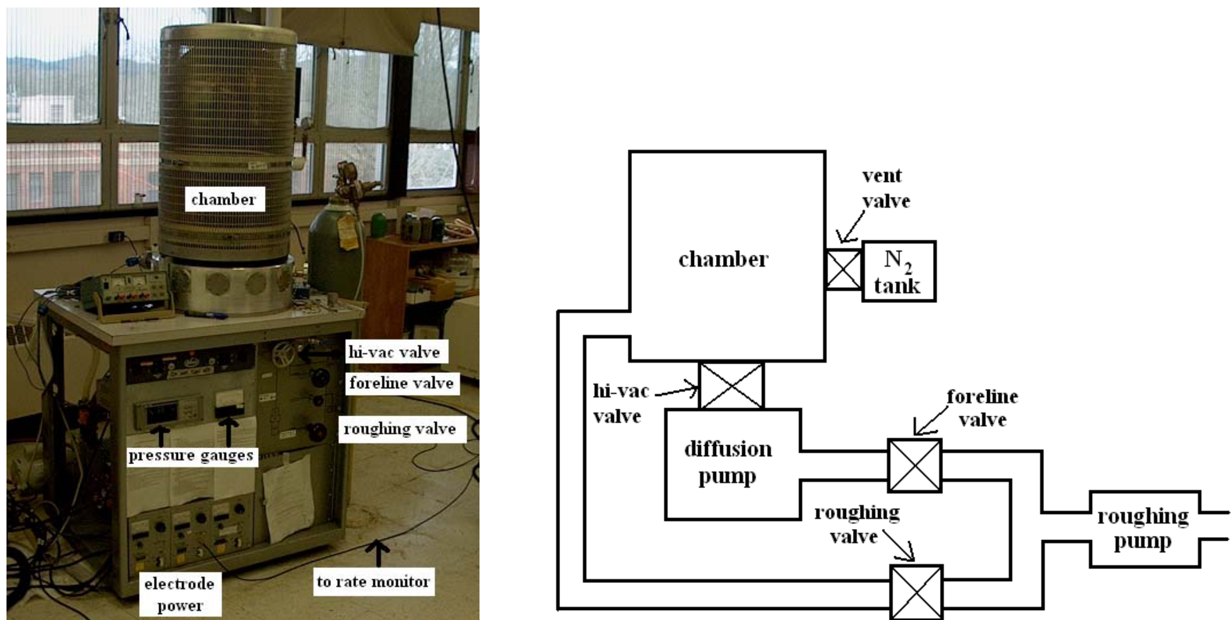

Figure 36. Thermal evaporator

In a thermal evaporator, a bulk sample of the material to be deposited must be placed within the chamber prior to pumping to high vacuum. Within the chamber is a set

of electrodes through which large amounts of current can be passed. The bulk material (in this case, a pellet of gold) is placed in a “boat” made of tungsten that makes electrical contact between the electrodes. The current is large enough (~25 Amps - 100 Amps) to cause sufficient ohmic heating to evaporate the deposited material (though not enough to melt the supporting tungsten). The chromium comes in the form of a thin rod (presumably with a tungsten core) and is placed between a second set of electrodes. The current through each can be independently controlled from the front panel.

Also within the chamber must be the substrates upon which the film must be deposited. These are positioned directly above the evaporation source so that a film of solid material condenses on the substrate from the gaseous phase. The final item present in the chamber is a rate monitor. This consists of a quartz crystal oscillator, the frequency of which can be correlated to the mass deposited on its surface. Knowing the density and acoustic impedance of the material being evaporated, the rate of film deposition can be inferred quite accurately from changes in the oscillator’s resonant frequency. This is all controlled by software, and a “tooling factor” can even be input to compensate for differences in rate at the location of the substrate and at the location of the rate monitor (due to proximity to the source of evaporation).

After the Au/Cr layer had been deposited, and the samples removed from the chamber, one further step in the metallization process remained. The step is known as “liftoff”, and it is used to remove metal from regions where it is not wanted. During the evaporation, metal was deposited over the entire patterned substrate. In the areas where the photoresist was removed, the metal would adhere directly to the oxide beneath. This forms the pattern that is desired. On the other hand, the metal that condenses on areas of photoresist must be removed by soaking the sample in acetone and exposing to mild ultrasonic agitation. The key to this technique being successful is that the deposited film must be thinner than the photoresist. This allows the acetone to make contact with and dissolve the photoresist, which allows the liberated metal to float away. In this process, the PR was about 0.5 micron with metallization layers from 100 nm – 200 nm.

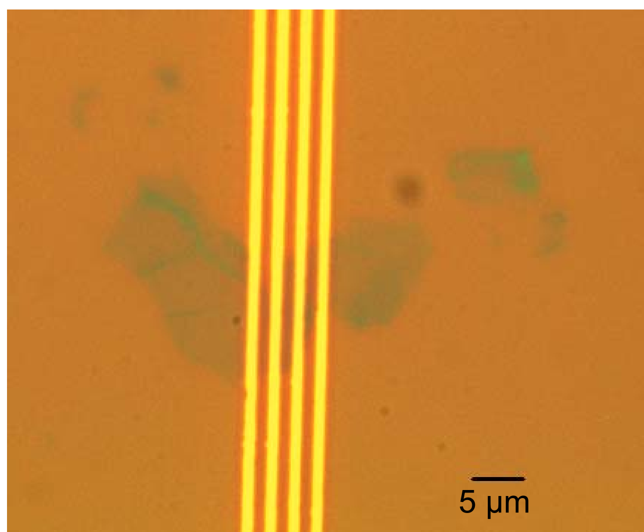

Figure 37. Gold electrodes overlapping GO flake

Sputtering is fundamentally quite different than thermal evaporation, though it also occurs under very high vacuum conditions. The sputtering system used in this study employs a turbomolecular (turbo) pump to achieve hi-vac state. The system also features a load-lock that sidesteps always having to pump down the entire chamber and so allows speedier processing. Unfortunately, the system has no rate monitor and rates were inferred by measuring the thicknesses of sputtered films by profilometry (see Appendix D).

The principle of sputtering involves using a combination of electric and magnetic fields to accelerate ions toward a target material (usually formed like a hockey puck), which they strike with sufficient energy to cause atoms of the material to be expelled in reaction to the impact. It is these atoms that re-deposit elsewhere in the chamber on a substrate, forming a thin film.

After the substrates and target material are loaded into the chamber and it is pumped down to vacuum, a small amount (~4 mTorr) of an inert gas (argon, in this case) is allowed into the chamber. An electric field is then applied that is large enough to strip many argon atoms of one or more electrons. This creates a mix of positive ions and free

electrons known as plasma. The target material is held at a negative potential so that the electric field accelerates the heavy positive ions into the target. A circular ring of magnets is also located directly behind the target material. They create a magnetic field that tends to trap the heavy ions into circular orbits directly above the target material, increasing the rate at which it is bombarded by ions.

Several variables influence the qualities of the resulting sputtered film. The deposition rate is determined primarily by the power used to generate the electric field which creates the plasma. If one thinks of the plasma as possessing a certain resistance, the power is related to the applied voltage by the familiar formula: $P=V^2/R$. The height of the substrate relative to the target is another important factor determining deposition rate. A third factor that influences deposition rate is the type of material being deposited. For each ion incident on the surface, the number of atoms ejected from the surface is different on average for each element (or compound). The ratio of atoms ejected per incident ion is known as the sputter yield and is tabulated for a variety of materials (see reference [74], page 446 for example).

For a given deposition rate, the film thickness is controlled by the amount of time that a shutter covering the target is left open and material is allowed to deposit on the substrate. For large substrates, uniformity can be improved by rotating the substrate beneath the target. The AJA system has the nice feature of automatic substrate rotation over a range of angular velocities up to several rotations per second. A substrate heat of up to 300 °C can also be applied. Substrate heat can affect the size of the grains in the sputtered film as well as its crystalline structure.

3.1.5 Wirebonding

The final step in sample preparation for the four-point resistance measurement structures was wirebonding. In this step, a very small (25 micron diameter) gold wire was used to establish electrical contact between each of the four electrodes touching a sample of graphene and four large contact pads around the perimeter of each substrate. Bonding

was accomplished using the Westbond tool (model 747677E) located in the applied magnetics research laboratory at OSU.

A wirebonding tool consists of a spool of gold wire threaded through a set of clamps (which can be actuated to either hold onto the wire or to let it pass freely) and then through a type of tool tip that is appropriate for the desired job. If ball bonds are to be used, a capillary tip must be employed. The short length of wire that protrudes through the tip is heated by a spark from a discharging capacitor, melting the wire and forming a ball. The ball is lowered against a contact pad and the tip is vibrated at ultrasonic frequencies for tens of milliseconds so that a bond is formed between the pad and the gold ball. The clamps are then released and wire is allowed to unspool as the second pad is positioned beneath the tool tip. The tip is again lowered into contact and the second bond is formed by the edge of the capillary tip pinching the wire and forming what is called a wedge bond. Once the second bond is formed, the clamps close and hold the wire as the tip is lifted from the surface, snapping the wire at the bond.

If a ball bond is not necessary, a wedge tip can be used which produces two wedge bonds rather than a ball bond and a wedge bond. Ball bonds are used because they are stronger than wedge bonds, but their downside is that they also cover a greater area than wedge bonds (about 3 times the diameter of the wire, rather than the 1.2 - 1.4 times for wedge bonds) and are more complicated because they require application of a spark to form the ball each time.

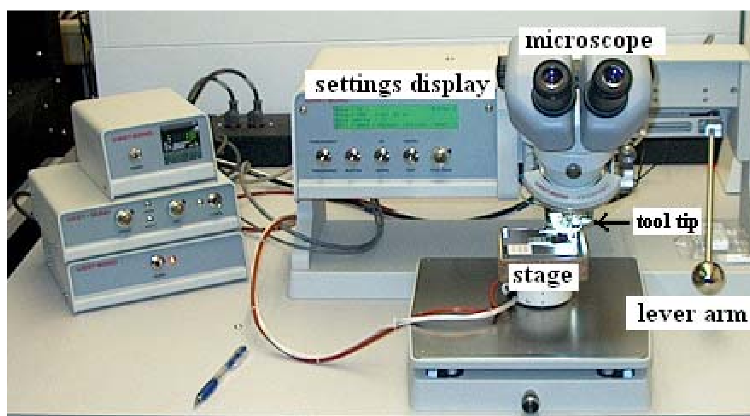

Figure 38. Westbond model 747677E wirebonder

The Westbond tool is operated by manually positioning the tool tip over a contact pad and lowering the tip into contact using a lever arm (see Figure 38). This is possible by viewing the substrate and tool tip through a low-power microscope. A sensor informs the microprocessor when the tip has contacted the surface and ultrasonic agitation is initiated. The pressure required to actuate agitation can be adjusted, as can both the time and the amplitude of the agitation. Two other parameters that can be adjusted are substrate temperature and temperature of the tool tip. These five parameters can be optimized to allow bonding to a variety of pad materials using either gold or aluminum wire of various gauges. In this research work, it was found that the following settings were the most successful at bonding 25 µm (one mil) diameter gold wire to thin gold contacts:

Pressure	Time	Amplitude	Stage Heat	Tip Heat
50 g	999 sec	Power = 185	325 °C	off

Table 1. Tool settings for wirebonder

It must be pointed out that this strategy of using wire-bonding to establish electrical connection to the GO sample was eventually abandoned due to the inevitability of short circuits developing between the bond pads and the substrate. It is believed that the vibrating tool tip destroys the thin oxide (~90 nm) beneath the bond pad due to a thin gold layer of only a few hundred nanometers being used (instead of the industry standard of 0.6 micron).

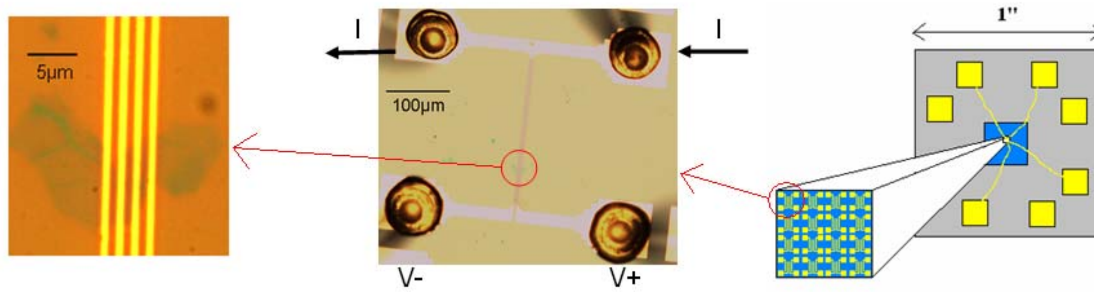

Figure 39. Ball bonds connect one 4-point structure to four perimeter pads

The solution to the problem of short-circuited contacts was solved by implementing a two-step metallization process. In the first step, a large number of resistance structures is deposited (same as before, only no perimeter contacts). In the second step, four much larger contact pads (4 mm) are aligned to overlap the desired contact structure (which is determined by optical microscopy). An SEM image of the results of the two-step deposition can be seen in Figure 40. At the very center is the contact structure that overlaps the GO flake, and connected to each of the 150 µm pads of this structure is a 4 mm pad that can be directly accessed using silver epoxy and a short length of wire (see Figure 41).

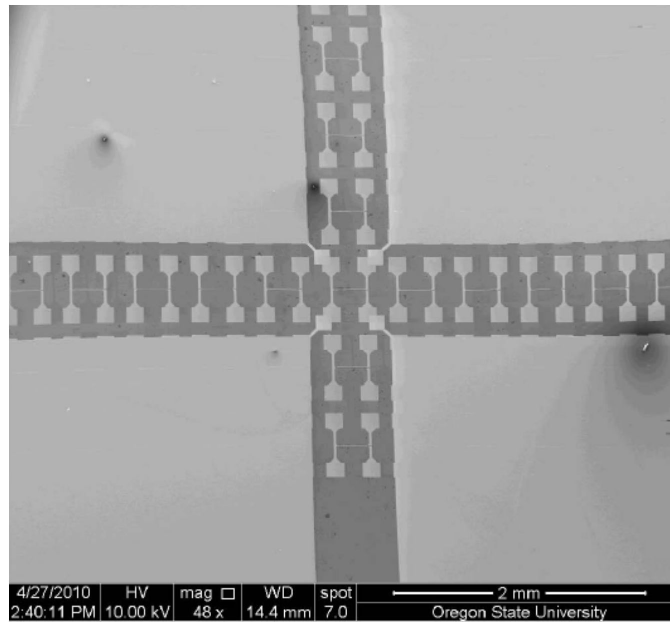

Figure 40. SEM image of two-Step metallization process

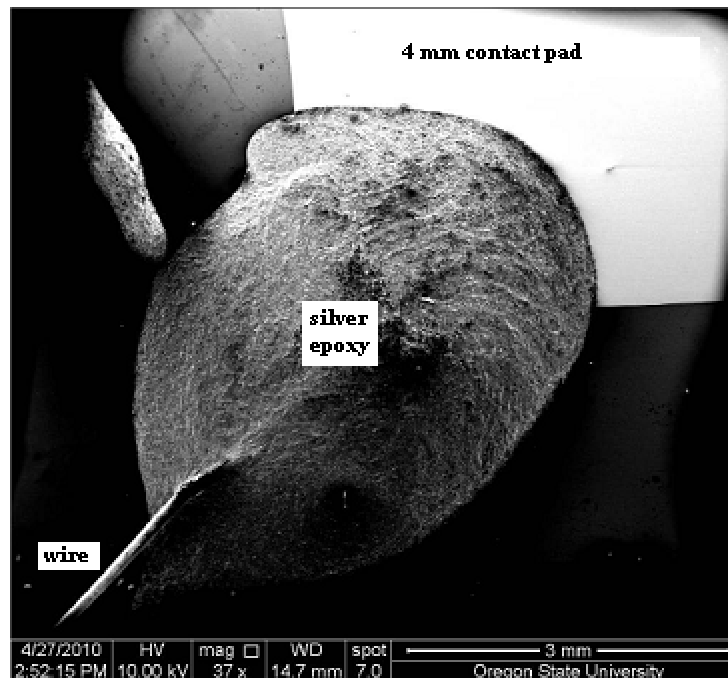

Figure 41. SEM image showing epoxy and wire connecting to resistance structure

3.2 Characterization Techniques

After successful sample fabrication, measurements of various electrical properties were performed. This section describes those measurements in detail. The first experimental apparatus to be discussed is the Probostat® and tube furnace. This arrangement allows the "in situ" measurement of the resistance of platelets of GO as they undergo thermal reduction. Next, the Agilent B1500a semiconductor parameter analyzer (SPA) is introduced. This is the device that sources current between the outer electrodes and measures the voltage developed across the inner two electrodes of the four-point structures. The final measurement tool to be discussed in this section is the BH-Looper manufactured by Shb Instuments, Inc. This tool is used to trace the hysteresis loops of the magnetic samples, and thus determines the coercivity of each contact design.

3.2.1 ProboStat™ and Tube Furnace

The ProboStat™ is a device manufactured by Norwegian Electro Ceramics which consists of a 50 cm long alumina tube, into which samples can be placed. There exist feedthroughs for up to four electrical contacts to the sample, as well as inlet and outlet ports for gasses to be flowed through the device (saturating the enclosed samples). The device can be placed in a standard tube furnace to control the temperature of the samples. This section will analyze the structure of the device in detail, as well as the various connections that were made to it for this experiment.

The sample is loaded into the device by first unthreading and removing the alumina shell to expose the platinum wires which run the length of the tube and terminate in BNC connectors. The four short lengths of radio wire that had been attached to the sample are each then wound around one of the ProboStat™ wires (see Figure 42).

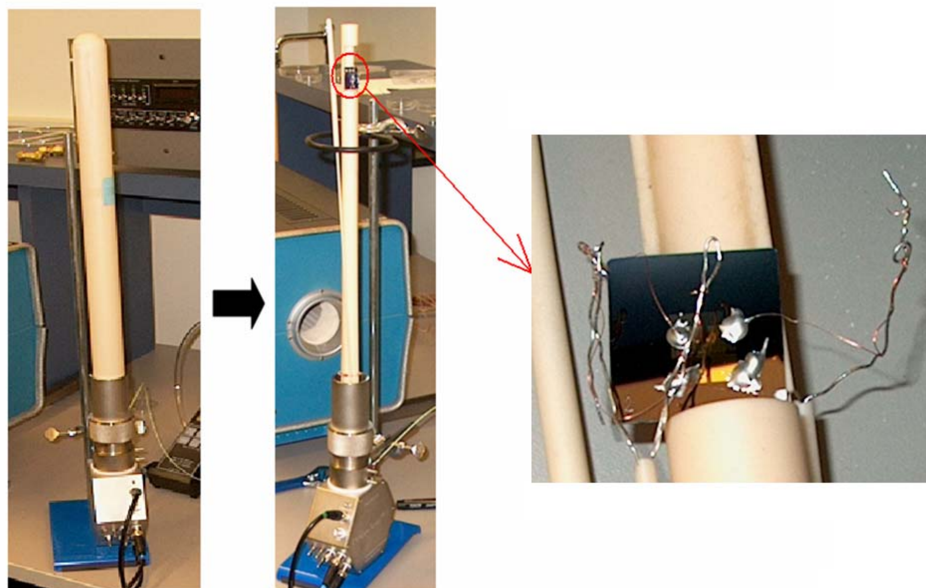

Figure 42. ProboStat^{TM} with alumina shell (left) and with shell removed (center and right)

The outer shell is then replaced, enclosing the sample and sealing against the base with a rubber O-ring. The entire apparatus is turned on its side and the tip holding the sample is inserted into the end of a “clam-shell” type tube furnace (see Figure 43a). There is also a thermocouple sensor within the tube near the sample which is used to accurately determine the temperature of the sample as it is heated (see Figure 43b).

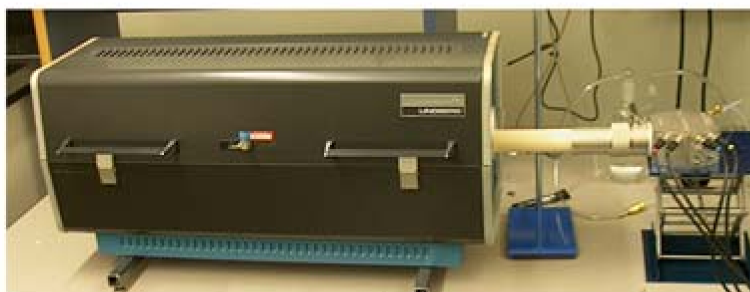

a)

b)

Figure 43. ProboStat^{TM} in tube furnace (left) thermocouple controller (right)

Gas flow through the tube and across the device is controlled by a manual switch which sends a signal to a mass flow controller (MFC) connected to a tank of compressed forming gas. Currents are sourced through the sample and voltages are measured by using a semiconductor parameter analyzer (discussed in Section 3.2.2) which is connected to the BNC ports of the ProboStat^{TM}. An overview of the experimental setup is shown in Figure 44. The top figure shows the components necessary for the desired measurement: a sample in an airtight chamber, through which gas can be flowed, with an electrical connection from the sample to a measurement device. The bottom pictures shows the actual arrangement.

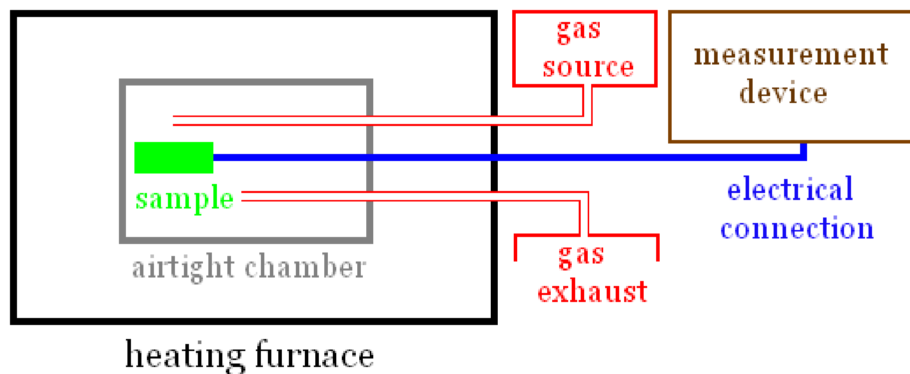

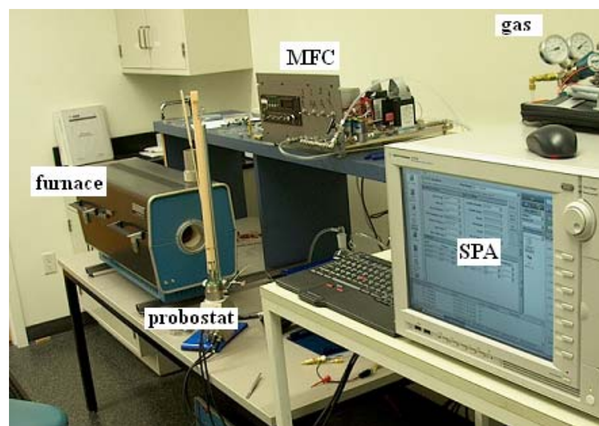

Figure 44. Experimental setup for in situ resistance measurements

3.2.2 Semiconductor Parameter Analyzer (SPA)

The Agilent B1500a semiconductor parameter analyzer is essentially a hybrid of a personal computer, a multimeter, and a power supply. It features a windows operating system and provides a convenient graphical interface through which a variety of electrical signals can be sourced while other electrical quantities can be sensed. The exact functionality of the tool depends on the particular units that have been installed in the expansion ports at the rear of the device. This experiment required the use of four of the expansion slots filled by three source/measurement units (SMU) and one ground unit (GNDU). Each SMU can be configured to either source a DC voltage or current (up to 100 V or 100 mA) or to sense a voltage or current (0.5 μV or 10 fA resolution).

In this experiment, each of the expansion units were connected to BNC ports on the ProboStat™ by short lengths of coaxial cable. As explained in the previous section, each BNC port is connected to a piece of platinum wire that runs the length of the device and makes electrical contact to one of the four electrodes of the sample's resistance measurement structure (via silver epoxy and a short length of radio wire). The ground unit is connected to one of the two outer electrodes and SMU1 is connected to the other outer electrode. SMU2 is connected to the inner electrode adjacent to SMU1 and SMU3 is connected to the inner electrode adjacent to the ground unit.

The Agilent B1500a comes programmed with a variety of commonly performed tests for which parameters are chosen from a pull-down menu or entered into specific fields. When all required parameters are entered (and the appropriate electrical connections have been made) a button can be clicked to begin gathering data. For this experiment, the data gathered is simply the voltages measured by SMU2 and SMU3 as a function of time. SMU1 is set to source a current, which will flow through the GO sample to the ground unit (see Figure 45). The magnitude of the current was chosen so that the voltages developed on the three SMUs (given by Ohm's law as the product of this current and the resistance of the GO sample) would be between about 1 V and 10 V. In order to

function as voltmeters (with a very large internal series resistance) SMU2 and SMU3 had to be configured as current sources with a magnitude of zero (sourcing zero current).

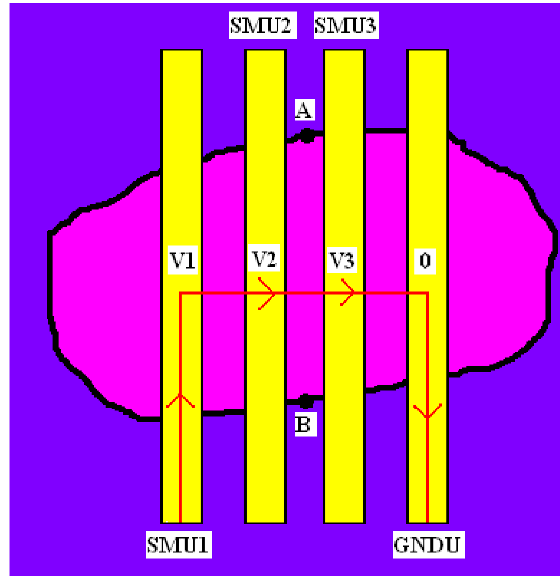

Figure 45. SPA connections to electrodes overlapping GO flake

The four-point resistance of the sample is given by the voltage at SMU2 (V2) minus the voltage at SMU3 (V3) divided by the current sourced by SMU1. From this, if the thickness of the sample (*t*) is known, the resistivity can be calculated:

$$\rho = R*t*x / (1\ \mu\text{m})\ [\Omega\text{-m}]$$

The variable "*x*" in the previous equation is the distance between points A and B in Figure 45 and one micron is the distance between the inner two electrodes. It is also not uncommon to consider GO/graphene to be two-dimensional and to report the material's sheet resistance:

$$R_{sh} = R*x / (1\ \mu\text{m})\ [\Omega/\text{square}]$$

The final parameters that had to be entered into the SPA in order to define the test were related to the time sampling of the data. Specifically, the time between data samples and the number of samples were entered, which together defined the duration of the test.

3.2.3 B-H Looper

A B-H looper is a tool that does exactly what one would expect, it generates B-H loops of materials. To be more precise, it plots the magnetic flux within a material (B*A) versus an applied magnetic field (H). In order to determine the flux density (B) the cross-sectional area of the sample lying within the pick-up coil must be known. Furthermore, a loop only occurs if the material exhibits hysteresis when the field is swept in opposite directions; showing a remanent flux at zero applied field, and requiring a certain magnitude of field (the coercive field) to reverse the direction of the flux within the material.

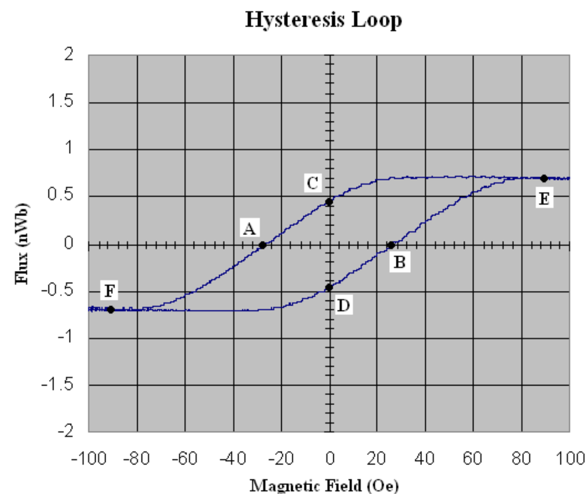

Figure 46. General features of magnetic hysteresis loop

The general features of the hysteresis loop are shown in Figure 46. For large positive magnetic fields, the sample's flux essentially saturates (point E). When the field is reduced to zero, there is some nonzero flux remaining in the sample which is known as the remanent flux (point C). At some magnitude of magnetic field applied in the opposite direction, the flux within the sample is reduced to zero. This is called the coercivity or coercive field (point A). As the field is increased further in this direction, the flux will eventually saturate (point F). As field is reduced to zero, the material will again exhibit

remanence (point D) and will display its coercivity (point B) as field is increased back in the original direction.

The basic operation of the tool is fairly straightforward. The sample is placed between two coils of wire known as a Helmholtz pair. The coils are of equal size, wound in the same direction, and are separated by a distance equal to the radius of the coils. It has been shown that when a DC current is run through this configuration, a quite uniform field is established between the coils ($d^2B/dx^2 = 0$ at the center, and the strength of the field varies by only 6 % from the center to the planes of the coils) [75].

In addition to the two coils comprising the Helmholtz pair, the sample is also surrounded by a third coil, the "pick-up" coil. Due to the way the sample is inserted into the tool, the plane of the pick-up coil is cut by the sample under test. When a low frequency AC current (~1 Hz - 10 Hz) is sourced through the Helmholtz pair, a sinusoidally alternating magnetic field is produced between the coils and this causes a sinusoidally alternating flux to develop within the sample. Because the sample is positioned within the pick-up coil, a sinusoidally alternating voltage is then induced on the pick-up coil in accordance with Faraday's law: $V = N(d\phi / dt)$ (where N is the number of turns in the coil and φ is the magnetic flux cutting the plane of the coils).

It should be pointed out that a voltage is also induced on the pick-up coil due to the alternating magnetic field being produced by the Helmholtz pair. This voltage, however, is easily "zeroed out" using software. Before the sample is inserted into the tool, AC current is run through the Helmholtz pair and the voltage induced on the pick-up coil is stored in memory. When a sample is inserted and a voltage is induced on the pick-up coil, this stored pattern is subtracted to give only the response of the material under test. This method also mitigates measurement error resulting from nearby sources of electromagnetic noise.

Figure 47. BH-Looper

This tool was used to characterize the switching fields (coercivities) of magnetic contacts of different geometries. It must be remembered that the goal of this investigation is to demonstrate a method of fabrication by which two magnetic contacts can be made to switch directions of magnetizations at independent fields. It will also be remembered that the ultimate goal of such research is to span the magnetic contacts with GO/graphene and seek evidence of the giant magnetoresistive effect as the contacts are independently switched.

4 Experimental Results

This chapter conveys the results of all experiments performed in the course of this thesis. This includes the resistance vs. time data for the thermal reduction of GO, various measurements taken on the material after reduction, and coercivity data for magnetic contacts of various dimensions.

4.1 Thermal Reduction of Graphite Oxide

This section reports the results of in situ four-point resistance measurements of thermally reduced graphite oxide (both in forming gas and in atmosphere). AFM and Raman data are also presented, along with data showing a weak ambipolar field effect. Both sheet resistance (resistivity) and mobility of reduced GO are inferred from measurements.

4.1.1 In Situ Resistance Measurements

In this experiment, the four-point resistances of samples of GO were monitored as functions of time as the samples were exposed to a forming gas environment and heated to 200 °C. Four different samples were studied.

The first sample showed an initial four-point resistance of about 22 MΩ. The sample was loaded into the ProboStat™ and heated to 200 °C. As the temperature increased, the resistance of the sample decreased and attained a stable value of less than 1 MΩ as the final temperature was reached (see Figure 48a). Once the temperature stabilized, the flow of forming gas was initiated and the resistance of the sample was observed to decrease even further (see Figure 48b). Over 7.5 hours, the resistance dropped by over half from about 860 kΩ to nearly 400 kΩ. After the resistance had reached a reasonably stable value, the sample was cooled back to room temperature (still in the presence of forming gas). The cooling was accelerated with the aid of fans, and took approximately one hour to accomplish. During this time the resistance increased from about 400 kΩ to nearly 1.2 MΩ (see Figure 48c). It was also found that the

resistance continued to increase at a rate of roughly 1 kΩ/minute after the temperature had stabilized at about 20 °C. Next, the forming gas flow was turned off and the ProboStat™ outer shell was opened (exposing the sample to atmosphere). At this point, the resistance began a rather steep increase which after a few hours had slowed to approach a constant increase of approximately 500 Ω/minute (see Figure 48d). Over eleven hours, the resistance had increased to 2.25 MΩ, roughly one order of magnitude lower than the original starting resistance. The two-point resistance was also measured and found to be 3.35 MΩ (allowing us to infer a resistance contribution of ~550 kΩ from the contact and wiring).

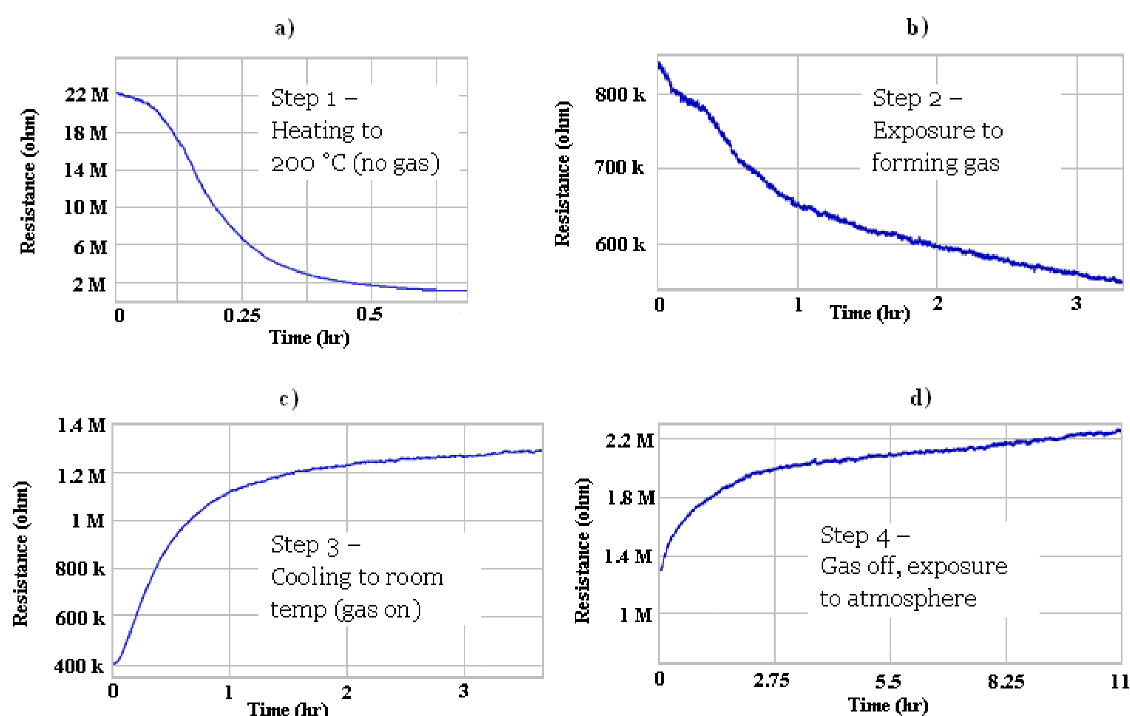

Figure 48. Resistance of GO changing as sample 1 undergoes reduction process

The next sample was exposed to exactly the same process of heating and gas exposure and similar results were obtained. This sample had an initial resistance of only about 1.5 MΩ which decreased to less than 100 kΩ when heated to 200 °C (see Figure 49a). One hour of gas flow reduced this resistance even further to about 60 kΩ (see

Figure 49b). As the sample was cooled to room temperature (in the presence of forming gas) the resistance increased to about 140 kΩ, and when the sample was exposed to atmosphere the resistance was observed to increase still further (see Figures 49c and 49d). After twenty-four hours of exposure to atmosphere, the four-point resistance had reached a value of 283 kΩ (a decrease by about a factor of five from its starting value). A two-point resistance measurement taken at this time gave 538 kΩ.

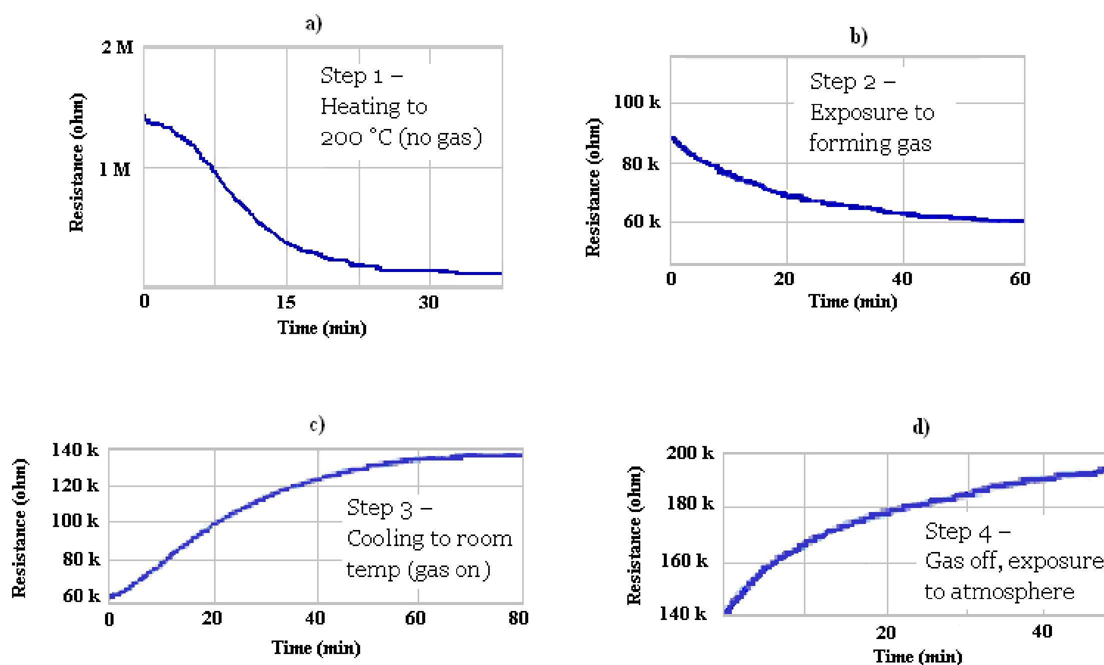

Figure 49. Resistance of GO changing as sample 2 undergoes reduction process

The third sample was given a slightly different treatment, in that the sample was exposed to forming gas from the very beginning. In this case, the gas flow was initiated and then the sample was heated to 200 °C. Results were obtained which were quite similar to those obtained in the first two instances. The initial resistance of this sample was 4.66 MΩ which decreased to about 80 kΩ when heated to 200 °C in the presence of forming gas (see Figure 50a). The sample was then observed to increase by a few hundred kilohms as it was cooled to room temperature and then to increase further as it was exposed to atmosphere (see Figures 50b and 50c). After twenty-four hours of

exposure to atmosphere, the resistance had reached 565 kΩ (two-point resistance was 1.35 MΩ). The results for the first three samples are summarized in Table 2.

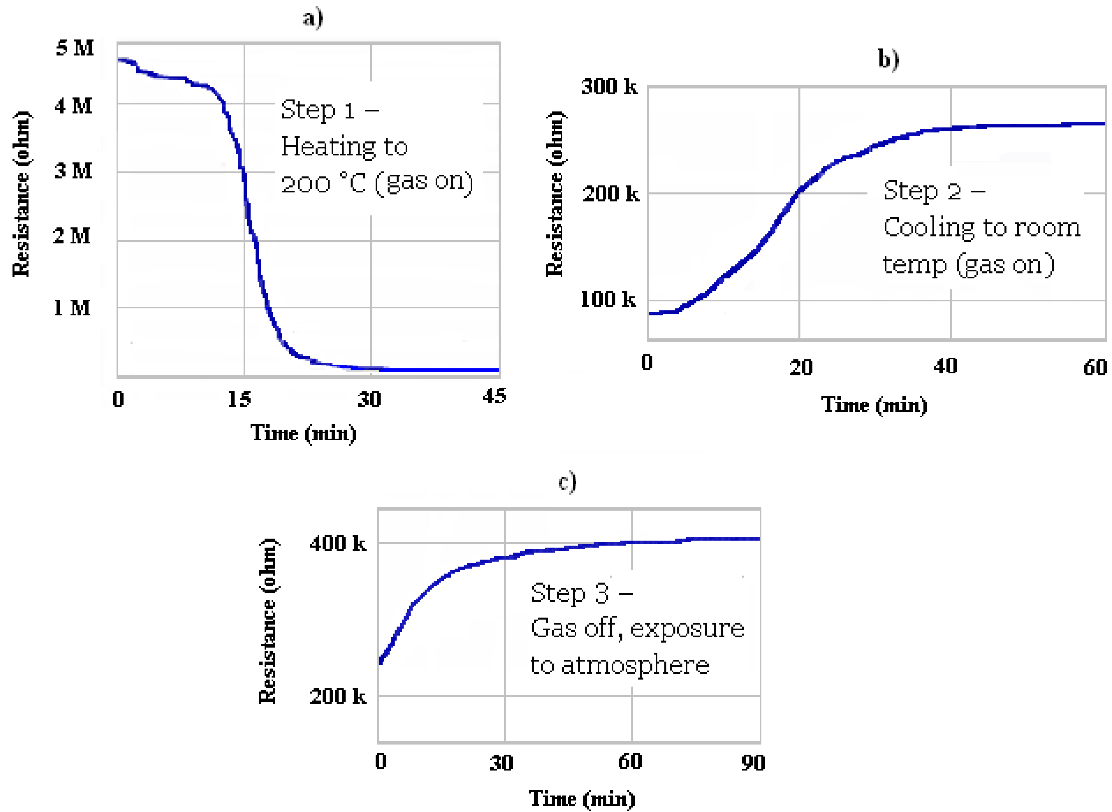

Figure 50. Resistance of GO changing as sample 3 undergoes reduction process

	Initial	200 °C (atm)	200 °C (gas)	20 °C (gas)	20 °C (atm)
Sample 1	22 MΩ	860 kΩ	400 kΩ	1.2 MΩ	2.4 MΩ
Sample 2	1.5 MΩ	100 kΩ	60 kΩ	140 kΩ	283 kΩ
Sample 3	4.66 MΩ	N.A.	80 kΩ	250 kΩ	565 kΩ

Table 2. Summary of results for samples 1-3

The fourth sample was used as a control to help elucidate the effect of the forming gas flow. In this experiment, the sample was heated to 200 °C and then cooled back to

room temperature without ever exposing the sample to forming gas. It was found that the sample's resistance decreased when heated from 8 MΩ to about 600 kΩ. When cooled back to room temperature, the sample's resistance increased to 1.44 MΩ. To investigate further, the sample was again heated to 200 °C and the resistance was seen to decrease to about 240 kΩ. When the sample was then cooled again to room temperature, the resistance only increased to 950 kΩ. A third round of heating and cooling was then performed. When heated, the resistance decreased to 200 kΩ and when cooled it increased to 700 kΩ. For the final round of heating and cooling, these same values were obtained, suggesting the sample could not be reduced further by this technique. These results are summarized in Table 3.

initial	**1st heat**	**1st cool**	**2nd heat**	**2nd cool**	**3rd heat**	**3rd cool**	**4th heat**	**4th cool**
8 MΩ	600 kΩ	1.44 MΩ	240 kΩ	950 kΩ	200 kΩ	700 kΩ	200 kΩ	700 kΩ

Table 3. Resistance of sample 4 repeatedly heated to 200 °C and cooled to room temp.

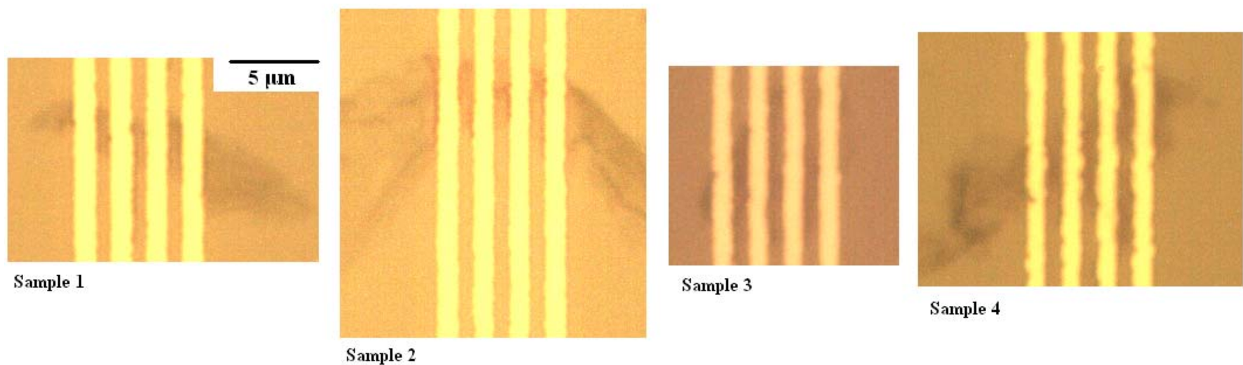

Figure 51. Optical microscope images of samples

4.1.2 Atomic Force Microscopy and Raman Spectroscopy

The only sample characterized by AFM was sample two, as it appeared from optical images that this sample was the thinnest. AFM imaging was able to confirm that the average thickness of this sample was ~4 nm (see Figure 52). This thickness would be consistent with 3-4 layer reduced GO.

This image also clearly shows that the width of the sample between the inner two electrodes is 4 μm. Using these dimensions (and assuming a 1 μm "length" between the electrodes) with a final resistance of 283 kΩ, one is able to calculate a resistivity of ~0.5 Ω-cm for this sample (1.25 MΩ/square).

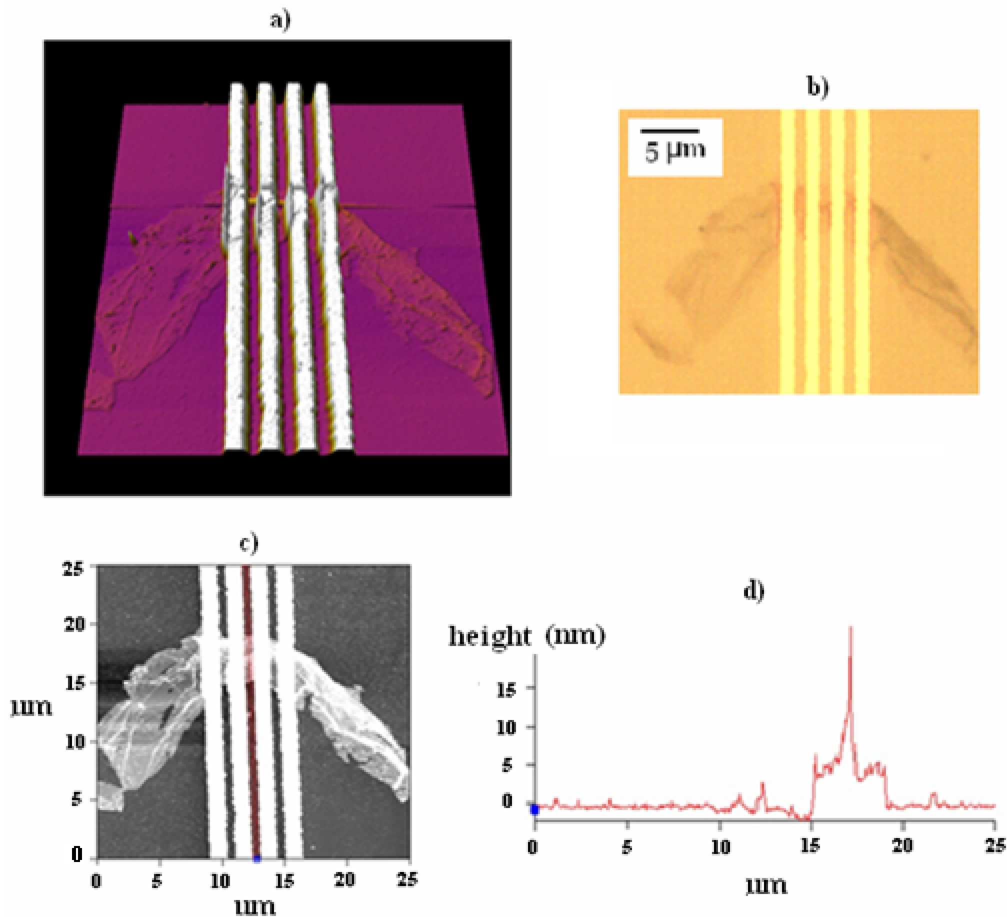

Figure 52. sample 2 - a.)3D AFM image. b.)optical image. c.)AFM image. d.)height profile along line shown in (c)

Raman spectroscopy was performed both on sample 2 and on another sample of GO which had not received any reduction treatment (see Figure 53). The peak at 0 cm^{-1} is simply the incident laser reflecting back into the detector due to an imperfect filter. The peaks at 510 cm^{-1} and roughly 1000 cm^{-1} can be attributed to Si-Si bonds (according to data from http://rruff.info). The next peak at ~1350 cm^{-1} is called the "D" peak (which, as we recall from Section 2.3.3) arises from defects. The final peak observed is the "G" peak at 1580 cm^{-1}. Recall that it is the ratio of this peak to the "2D" peak at ~2700 cm^{-1} that is used to determine the number of layers in pristine graphene. No such "2D" peak was observed in either the reduced or unreduced GO sample.

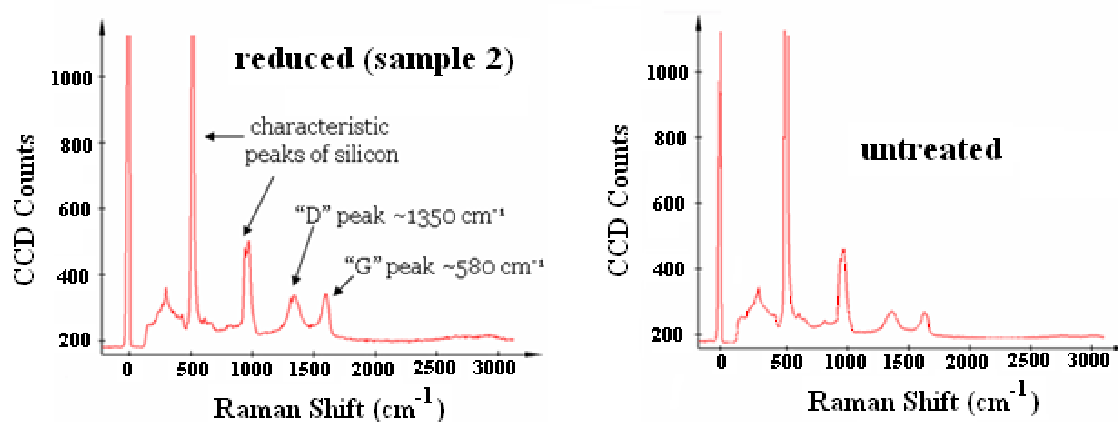

Figure 53. Raman spectra of both reduced and unreduced GO

4.1.3 Substrate Bias

As explained in Section 2.1.3, graphene displays an ambipolar field effect in which the resistance decreases when exposed to electric fields of both polarities (conductivity proportional to field intensity). This effect was observed in sample 2 though it was a much weaker effect than that observed in "pristine" graphene. The resistance of the sample could only be decreased by up to 16 % (see Figure 54) whereas in pristine graphene it can be modulated by up to a factor of about thirty.

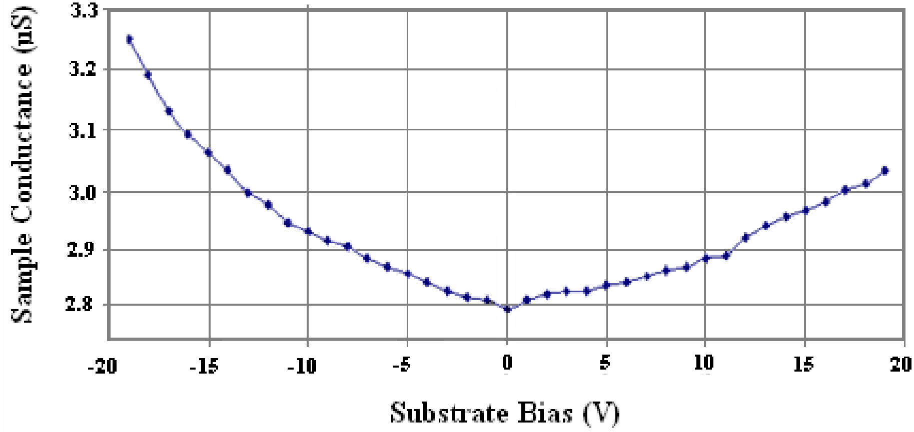

Figure 54. Conductivity increases with substrate bias

Figure 54 was obtained by applying a voltage across the inner two contacts of the structure and measuring the current that flowed through the sample. The voltage was swept from -1 V to +1 V and conductance was taken as the slope of the curve (d*I*/d*V*). The resistances given by the inverse of the conductances are therefore two-point resistances. This test was performed as the substrate bias was also swept from -19 V to +19 V.

As discussed at the end of Section 2.4.1, the carrier mobilities of a sample of graphene can be estimated from the slope of a graph of "drain" current through the sample vs. "gate" bias applied to the substrate:

$$\mu_n = (\partial I_D / \partial V_G) * (\frac{L}{ZC_{ox}V_D}) \quad ; \text{ for } V_g > V_{Dirac}$$

For positive gate voltages (and a drain bias of 0.1 V), the slope is $3*10^{-8}$. A 90 nm thick oxide gives a capacitance of $3.84*10^{-8}$ F/cm^2. Substituting these values (along with L=1 µm and Z=4 µm) yields $\mu_n \approx 2$ cm^2/V-s. A similar analysis for $V_g < V_{Dirac}$ gives the same value for μ_p: 2 cm^2/V-s.

This estimate can be improved somewhat when leakage current through the gate oxide is taken into account. Figure 55 shows a plot of current through the device vs. drain

bias for five values of substrate (gate) bias. It can be seen that when a substrate bias is applied, the current through the device is not zero when the drain bias is zero (y-intercept not zero). This zero-bias current can be subtracted from the currents measured at each gate bias to give only the current that passes between drain and source contacts (drain current). This does not change the calculated resistances, but it does change the value obtained for dI_D/dV_G. For positive gate voltages, the ratio is $1*10^{-9}$ (giving $\mu_n \approx 0.1$ $cm^2/V\text{-}s$) while for negative gate voltages, the ratio is $2*10^{-9}$ (giving $\mu_p \approx 0.2$ $cm^2/V\text{-}s$).

By plotting the measured current vs. gate voltage when the drain bias is zero, the oxide resistance can also be extrapolated. For this sample, an oxide resistance of 30.9 MΩ was obtained.

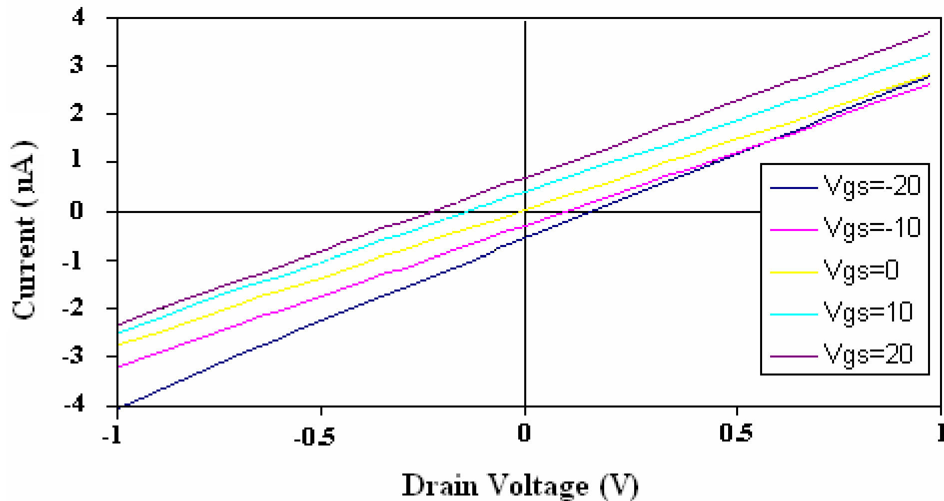

Figure 55. Current flow through “source” contact vs. “drain” and gate” voltages

The same test was performed on sample 4, which was reduced thermally by repeated heating in atmosphere, and no evidence of the ambipolar field effect was observed. In this case, the gate voltages were limited to ±4 V because nonlinearities were observed when larger magnitudes were applied.

4.2 Independently Switchable Magnetic Contacts

As discussed in Section 3.1.4, magnetic contact structures were formed by first sputter depositing permalloy (Ni:Fe::81%:19%) films of roughly 100 nm thickness onto a silicon wafer with 200 nm thermally grown oxide. The ferromagnetic film was then lithographically patterned and wet-etched using nitric acid (~15 minutes in 1:1::H_2O:HNO_3) to form structures of varying aspect ratios. Some samples were patterned with "short" contacts only (60 µm x 35 µm), others were patterned with "long" contacts only (90 µm x 30 µm), and some were patterned with contacts of both sizes. Each 1" square substrate contains approximately ten thousand contacts. Figure 56 shows a microscope image of a substrate patterned with both big and small contacts.

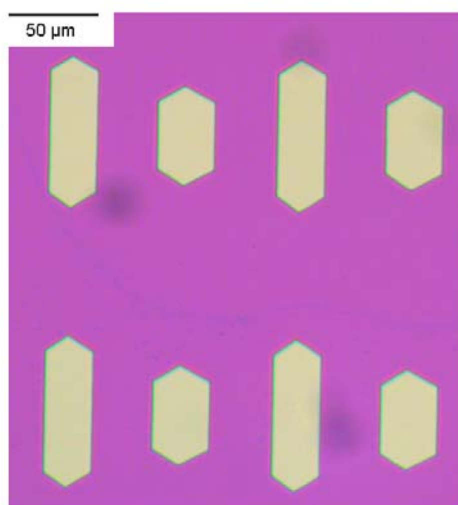

Figure 56. Substrate patterned with permalloy structures

Three samples were fabricated with short contacts only. The measured coercivities were 54.2 Oe, 55.7 Oe, and 66.1 Oe with an average coercivity of 58.7 Oe (standard deviation = 5.3 Oe). Four samples were fabricated with long contacts only. The measured coercivities of these samples were 63.9 Oe, 69.3 Oe, 65.2 Oe, and 67.9 Oe: an average coercivity of 66.6 Oe (standard deviation = 2.2 Oe). Four unpatterned permalloy samples were also measured and displayed an average coercivity of 45.7 Oe (standard

deviation = 4.9 Oe). Only two samples were fabricated with both long and short contacts. Their measured coercivities were 50.6 Oe and 47.8 Oe: an average of 49.2 Oe. These results are summarized in Table 4. Figure 57 shows representative hysteresis loops for samples patterned with only short contacts (left) and with only large contacts (right). The coercivity (x-axis crossing) is clearly larger for the deisgn with longer contacts.

	Short only	Long only	Short and long	Unpatterned
Average coercivity	**58.7 Oe**	**66.6 Oe**	**49.2 Oe**	**45.7 Oe**
Standard deviation	**5.3 Oe**	**2.2 Oe**	**2.0 Oe**	**4.9 Oe**

Table 4. Results of coercivity measurements

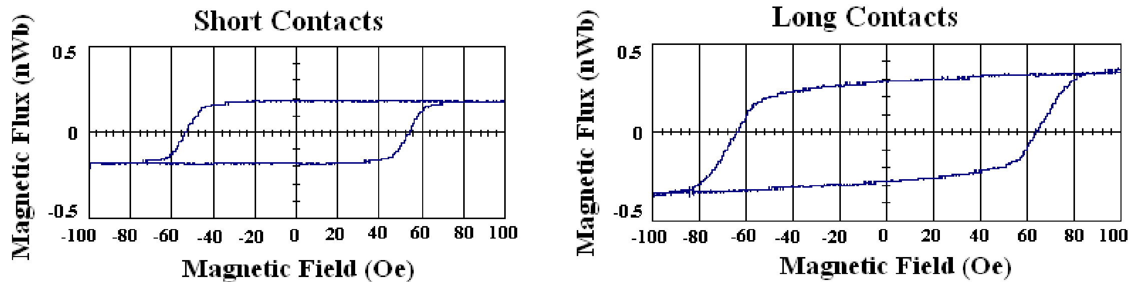

Fig 57. Representative hysteresis loops for short and long contacts designs

These results compare well with calculated values. Subtracting the measured coercivities of the patterned samples from the coercivities of the unpatterned samples (square, no shape anisotropy) gives the contribution to coercivity arising from the geometric shape of the contacts. For the shorter contacts, this was 13.0 Oe and for the longer contacts, it was 20.9 Oe. The samples with both sizes of contacts gave rather unexpected results, however. One would have expected a coercivity somewhere in between the coercivities for the samples with small contacts only and those with large contacts only. Instead, a coercivity just 3.5 Oe larger than the unpatterned samples was observed. Upon closer examination of these samples under a microscope, it was found

that both were incompletely etched and the results were probably skewed by a very thin layer of permalloy remaining over the entire sample.

The effects due to shape anisotropy can be estimated by using the following approximations for the demagnetizing factors of two-dimensional structures:

$$N_w \approx 2t / (\pi w) \quad ; \quad N_h \approx 2t / (\pi h)$$

In these equations, t is the thickness of the film, w is the length along the long axis, and h is the length along the short axis. The coercive field needed to rotate the magnetization through the hard axis (this analysis does assume single domain particles) is given by $M_s*(N_h-N_w)$ [76].

Using a film thickness of 100 nm and a saturation magnetization (M_s) of 1 Tesla for permalloy, one can calculate the short contacts to have a coercivity of 7.6 Oe and our long contacts to have a coercivity of 14.1 Oe. This is about 6 Oe less than what was observed and can probably be attributed to the contacts being pointed rather than rectangular.

5 Discussion of Results and Conclusion

This chapter will begin with a comparison of some of the properties observed in thermally reduced graphite oxide with those reported for graphene (rGO) obtained by other methods.

	Conductivity (S/cm)*	Mobility (cm^2/V-s)
Mechanical Exfoliation [1]	~ $5*10^4$ - 1545	3000 - 10,000
Chemical vapor deposition [22]	$3.6*10^4$	3700
Reduction of GO with hydrazine [12]	2	2 - 200
Thermal reduction of GO in forming gas	~ 2 – 0.1	~ 0.1

* In some cases, conductivity was inferred from a reported two-dimensional sheet resistance by assuming a thickness of 1 nm: $\sigma = (1/R_{sh})*10^7$

Table 5. Comparison of electrical properties of graphene obtained by different methods

It is easy to see that the properties of rGO cannot begin to compete with those of pristine graphene obtained by mechanical exfoliation or grown by CVD. It is interesting to note that the maximum conductivity obtained by reduction of graphite oxide is still orders of magnitude lower than the minimum conductivity observed in pristine graphene. The method of thermal reduction in forming gas does seem to give conductivities that are at least comparable to those obtained by reduction with hydrazine, however (although the estimated mobility is not as high).

One point that requires some discussion is that the starting resistances of the four samples studied were 22 MΩ, 1.5 MΩ, 4.66 MΩ, and 8 MΩ. It was stated earlier that unreduced GO is a strong insulator and if one looks in the literature, one finds reports of resistances in the GΩ range [15]. This discrepancy can perhaps be traced to the methods used to fabricate the samples studied. It will be recalled that the GO was spray deposited on a wafer heated to 225 °C. Though not at this temperature for very long, this can be considered a short thermal treatment and likely decreased the resistance of the samples. Next, the samples were patterned with photoresist and placed in an evaporation chamber where they were brought to a vacuum of $5*10^{-6}$ Torr for over one hour and exposed to elevated temperatures during the thermal evaporation of gold (melting point ~1000 °C) and chromium (m.p. ~1850 °C) contacts. This step is speculated to have had significant effect on the "initial" resistances of the samples studied. None of the references cited specifically mention such a high temperature deposition step in the preparation of their samples [11,12,13,14,15]. It would be interesting to fabricate structures by sputtering instead of thermal evaporation and compare the measured resistances.

It does seem to be clear from the data that the presence of forming gas during the reduction process increases the conductivity of the sample by about a factor of two over heating in atmosphere. The resistance of sample 1 dropped from 860 kΩ to 400 kΩ when exposed to forming gas for several hours at 200 °C. Likewise, exposure of the sample to atmosphere for 24 hours (after cooling to room temperature in forming gas flow) increased the resistance from 1.2 MΩ to 2.4 MΩ. In fact, comparison of the two rightmost columns in Table 2 reveals this relationship for samples 1-3. A final piece of evidence for this conclusion comes from comparing the initial resistance of sample 4 (8 MΩ) with its resistance after the first heating and cooling cycle (1.44 MΩ). This is a change by a factor of 5.55 when the sample is heated and cooled in atmosphere. The resistance of sample 3, which was heated to 200 °C then cooled to room temperature under forming gas flow, changed from 4.66 MΩ to 250 kΩ, a decrease in resistance of over 18 times.

A second point that should be observed is that the resistance of the thermally reduced GO sample is not a stable value, but increases with time. It was shown in Figure 48d that the resistance continues to increase (at a rate of about 500 Ω/min) even up to eleven hours after cooled to room temperature and exposed to atmosphere. More than a month after thermal treatment in forming gas, the resistance of sample 2 had increased to 980 kΩ (2-point resistance). If we recall that the two-point resistance of the sample was 357 kΩ roughly 24 hours after reduction, one begins to realize that the electrical properties of thermally reduced GO are quite unstable.

In conclusion, the dynamics of the thermal reduction of graphite oxide in forming gas have been well characterized and conductivities have been achieved which are consistent with those obtained by other methods of reduction. The small sample size of the experiment is an admitted weakness, but the cost and difficulty of fabrication of the devices made it difficult to include a larger data set.

6 Recommendations for Future Work

The next logical step in this research would be to look for evidence of the magnetoresistive effect in thermally reduced GO samples. This would be done by patterning a substrate with GO platelets and thermally reducing them in the manner described in this work. An array of magnetic contact pairs with differing coercivities would then be deposited and a search under an optical microscope would reveal samples that are suitable for study. Contact could be made to the samples via microprobes and resistance could be measured using the Agilent B1500a SPA. A magnetic field could be accurately swept to flip the magnetization of only one contact, perhaps resulting in a measurable change in resistance. This could be efficiently done using the Lakeshore probe station in the Applied Magnetics Laboratory in Kelley Engineering Center which features applied field control of up to 0.55 Tesla and ability to control temperature from 400 K to the temperature of whatever coolant is used (4 K for liquid helium, 77 K for liquid nitrogen). Contacts could be given various spacings to help elucidate the spin transfer length in the material should the magnetoresistive effect be observed. The effect of substrate bias on spin transfer through the material could also be investigated.

Once it is proven that the spins on the electrons maintain their orientation while traversing a sample, a “spintronic” device could be constructed which would use a third terminal (gate) to modulate the orientations of the spins of the electrons as they pass from one magnetic contact (source) to another (drain). Two possible manifestations of such a device are shown in Figure 58. The top picture shows a low resistance state in which both contacts are magnetized in the same direction. In the design shown in the bottom left picture, a “gate” terminal is used to cause the electrons to change the direction of their orientation so that they arrive anti-parallel to the second contact (a high resistance state). In the design shown in the bottom right, the direction of magnetization of one of the contacts could be made to switch in order to achieve the high resistance state. This would be possible due to a difference in coercivities of the contacts perhaps brought about by shape anisotropy. It is interesting to note that in this case the third terminal would be a

current carrying strip (not shown in picture) that would produce the magnetic field necessary to switch the magnetization of the contact.

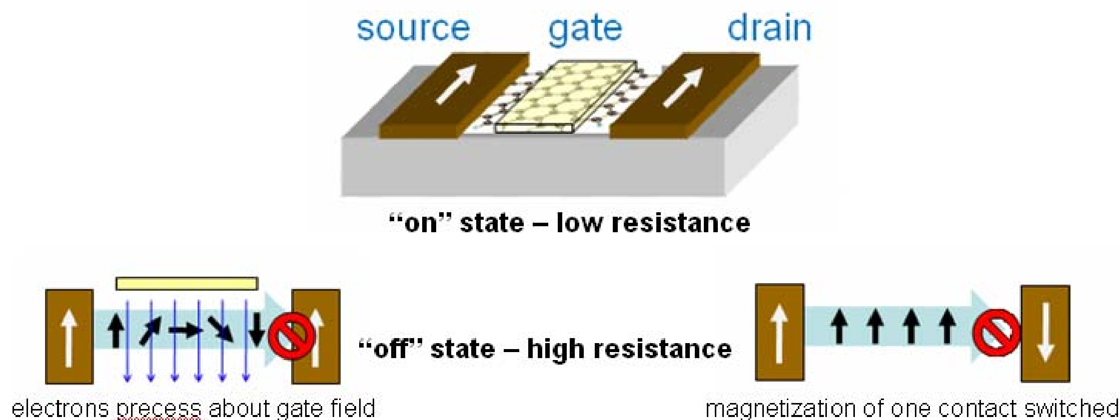

Figure 58. Two possible "spintronic" devices based on graphene

Perhaps the author's strongest recommendation for future work is to abandon research into graphite oxide and focus instead on obtaining "pristine" graphene by chemical vapor deposition (CVD) techniques. As shown in Table 5, graphene obtained by CVD on nickel films has been shown to have conductivities more than four orders of magnitude higher than can be obtained by the reduction of graphite oxide. This is indicative of a very high degree of order and purity, qualities which are necessary for spin orientation to be conserved for any significant distance in the material.

Initial investigations have been made into CVD growth of graphene on both nickel and copper. This was done using the tube furnace, located in Dr. Minot's lab in Weniger, to heat samples while exposing them to processing gasses such as methane, argon, and hydrogen. The resulting carbon films were then liberated by a metal etchant and transferred to oxidized silicon substrates using PDMS (as described in Section 2.2.4). It can be seen in Figure 59 that the resulting films have been patchy with many thick areas.

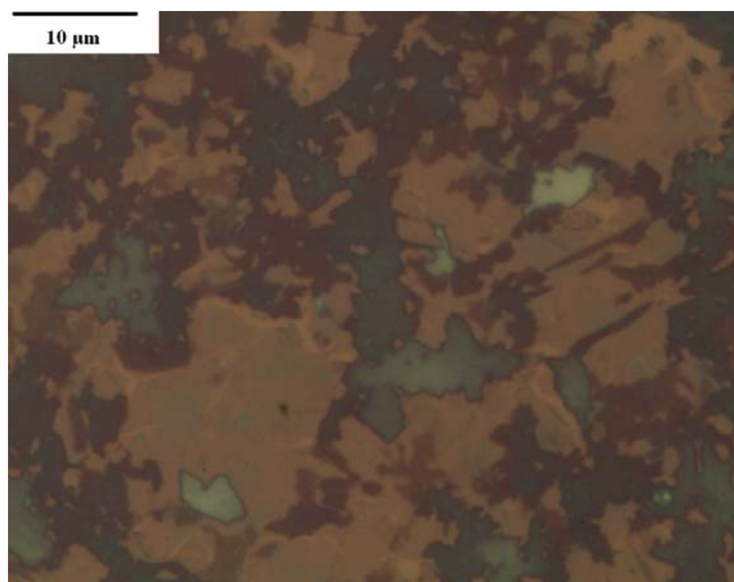

Figure 59. Carbon film grown by CVD on nickel

It is believed that a vacuum pump, which will soon be installed at the exhaust end of the CVD furnace to allow for low-pressure growth, will improve the quality of the resulting films. This and some amount of experimentation with variables such as temperature, pressure, flow rate, and processing time should eventually yield high-quality large-area graphene films, to be characterized and integrated into three-terminal "spintronic" devices.

BIBLIOGRAPHY

1. K. S. Novoselov, A. K. Geim, S. V. Morozov, D. Jiang, Y. Zhang, S. V. Dubonos, I. V. Grigorieva, A. A. Firsov, "Electric Field Effect in Atomically Thin Carbon Films," Science, vol. 306, pp. 666-669, Oct. 22, 2004.
2. A. K. Geim, K. S. Novoselov, "The Rise of Graphene," Nature Materials, vol. 6, no. 3, pp. 183-191, Mar. 2007.
3. A. K. Geim, P. Kim, "Carbon Wonderland," Scientific American, vol. 298, no. 4, pp. 90-97, Apr. 2008.
4. A. K. Geim, "Graphene: Status and Prospects," Science, vol. 324, pp. 1530-1534, June 19, 2009.
5. T. Seyller, A. Bostwick, K. V. Emtsev, K. Horn, L. Ley, J. L. McChesney, T. Ohta, J. D. Riley, E. Rotenberg, F. Speck, "Epitaxial Graphene: A New Material," Physical Status Solidi B, vol. 245, no. 7, pp. 1436-1446, June 2008.
6. C. Berger, Z. Song, X. Li, X. Wu, N. Brown, C. Naud, D. Miyou, T. Li, J. Hass, A. Marchankov, E. H. Conrad, P. N. First, W. A. de Heer, "Electronic Confinement and Coherence in Patterned Epitaxial Graphene," Science, vol. 312, pp. 1191-1196, May 26, 2006.
7. A. Reina, X. Jia, J. Ho, D. Nezich, H. Son, V. Bulovic, M. S. Dresselhaus, J. Kong, "Large Area, Few-Layer Graphenes on Arbitrary Substrates by Chemical Vapor Deposition," Nano Letters, vol. 9, no. 1, pp. 30-35, Jan. 14, 2009.
8. W. S. Hummers, R. E. Offeman, "Preparation of Graphitic Oxide," Journal of the American Chemical Society, vol. 80, no. 6, p. 1339, Mar. 20, 1958.
9. N. I. Kovtyukhova, P. J. Ollivier, B. R. Martin, T. E. Mallouk, S. A. Chizhik, E. V. Buzaneva, A. D. Gorchinskiy, "Layer By Layer Assembly of Ultrathin Composite Films From Micron-Sized Graphite Oxide Sheets and Polycations," Chemistry of Materials, vol. 11, no. 3, pp. 771-778, Mar. 1999.

10. D. W. Boukhvalov, M. I. Katsnelson, “Modeling of Graphite Oxide,” Journal of the American Chemical Society, vol. 130, no. 32, pp. 10697-10701, Aug. 13, 2008.
11. S. Gilje, S. Han, M. Wang, K. Wang, R. B. Kaner, “A Chemical Route to Graphene for Device Applications,” Nano Letters, vol. 7, no. 11, pp. 3394-3398, Nov. 2007.
12. C. Gomez-Navarro, R. T. Weitz, A. M. Bittner, M. Scolari, A. Mews, M. Burghard, K. Kern, “Electronic Transport Properties of Individual Chemically Reduced Graphene Oxide Sheets,” Nano Letters, vol. 7, no. 11, pp. 3499-3503, Nov. 2007.
13. S. Stankovich, D. A. Dikin, R. D. Piner, K. A. Kohlhaas, A. Kleinhammes, Y. Jia, Y. Wu, S. T. Nguyen, R. S. Ruoff, “Synthesis of Graphene-based Nanosheets via Chemical Reduction of Exfoliated Graphite Oxide,” Carbon, vol. 45, no. 7, pp. 1558-1565, June 2007.
14. M. Hirata, T. Gotou, M. Ohba, “Thin Film Particles of Graphite Oxide,” Carbon, vol. 43, no. 3, pp. 503-510, Mar. 2005.
15. I. Jung, D. Dikin, R. D. Piner, R. S. Ruoff, “Tunable Electrical Conductivity of Individual Graphene Oxide Sheets Reduced at ‘Low’ Temperatures,” Nano Letters, vol. 8, no. 12, pp. 4283-4287, Dec. 10, 2008.
16. E. W. Hill, A. K. Geim, K. Novoselov, F. Schedin, P. Blake, “Graphene Spin Valve Devices,” IEEE Transactions on Magnetics, vol. 42, no. 10, pp. 2694-2696, Oct. 2006.
17. M. Nishioka, A. M. Goldman, “Spin Transport Through Multilayer Graphene,” Applied Physics Letters, vol. 90, no. 25, pp. 252505(1-3), June 18, 2007.
18. A. H. Castro Neto, F. Guinea, N. M. Peres, K. S. Novoselov, A. K. Geim, “The Electronic Properties of Graphene,” Reviews of Modern Physics, vol. 81, no. 1, pp. 109-162, Jan.-Mar. 2009.
19. B. Partoens, F. M. Peeters, “From Graphene to Graphite: Electronic Structure Around the K Point,” Physical Review B, vol. 74, no. 7, pp. 075404(1-11), Aug. 15, 2006.

20. K. S. Novoselov, A. K. Geim, S. V. Morozov, D. Jiang, M. I. Katsnelson, I. V. Grigorieva, S. V. Dubonos, A. A. Firsov, "Two-Dimensional Gas of Massless Dirac Fermions in Graphene," Nature, vol. 438, pp. 197-200, Nov. 10, 2005.

21. M. I. Katsnelson, K. S. Novoselov, "Graphene: New Bridge between Condensed Matter Physics and Quantum Electrodynamics," Solid State Communications, vol. 143, no. 1-2, pp. 3-13, July 2007.

22. K. S. Kim, Y. Zhao, H. Jang, S. Y. Lee, J. K. Kim, Kw. S. Kim, J. Ahn, P. Kim, J. Choi, B. H. Hong, "Large-scale Pattern Growth of Graphene Films for Stretchable Transparent Electrodes," Nature, vol. 457, pp. 706-710, Feb. 5, 2009.

23. D. Schroder, Semiconductor Material and Device Characterization, 3rd ed., Hoboken, New Jersey: John Wiley and Sons, Inc., 2006.

24. S. Elliott, The Physics and Chemistry of Solids, West Sussex, England: John Wiley and Sons, Ltd., 1998.

25. Z. Jiang, Y. Zhang, Y. W. Tan, H. L. Stormer, P. Kim, "Quantum Hall Effect in Graphene," Solid State Communications, vol. 143, no. 1-2, pp. 14-19, July 2007.

26. C. Lee, X. Wei, J. W. Kysar, J. Hone, "Measurement of the Elastic Properties and Intrinsic Strength of Monolayer Graphene," Science, vol. 321, pp. 385-388, July 18, 2008.

27. S. Ghosh, D. L. Nika, E. P. Pokatilov, A. A. Balandin, "Heat Conduction in Graphene: Experimental Study and Theoretical Interpretation," New Journal of Physics, vol. 11, pp. 095012(1-19), Sept. 2009.

28. X. Wang, L. Zhi, K. Mullen, "Transparent, Conductive Graphene Electrodes for Dye-Sensitized Solar Cells," Nano Letters, vol. 8, no. 1, pp. 323-327, Jan. 2008.

29. P. Blake, E. W. Hill, A. H. Castro Neto, K. S. Novoselov, D. Jiang, R. Yang, T. J. Booth, A. K. Geim, "Making Graphene Visible," Applied Physics Letters, vol. 91, no. 6, pp. 063124(1-3), Aug. 6, 2007.

30. M. N. Baibich, J. M. Broto, A. Fert, F. Nguyen Van Dau, F. Petroff, P. Etienne, G. Creuzet, A. Friedrich, J. Chazelas, "Giant Magnetoresistance of (001)Fe/(001)Cr Magnetic Superlattices," Physical Review Letters, vol. 61, no. 21, pp. 2472-2475, Nov. 21, 1988.

31. E. Y. Tsymbal, D. G. Pettifor, "Perspectives of Giant Magnetoresistance," Solid State Physics, vol. 56, pp. 113-237, 2001.

32. A. Fert, H. Jaffries, "Conditions for Efficient Spin Injection from a Ferromagnetic Metal into a Semiconductor," Physical Review B, vol. 64, no. 18, pp. 184420(1-9), Nov. 1, 2001.

33. E. I. Rashba, "Theory of Electrical Spin Injection: Tunnel Contacts as a Solution of the Conductivity Mismatch Problem," Physical Review B, vol. 62, no. 24, pp. 16267-16270, Dec. 15, 2000.

34. J. Bass, W. P. Pratt, "Spin-diffusion Lengths in Metals and Alloys, and Spin-flipping at Metal/Metal Interfaces: an Experimentalist's Critical Review," Journal of Physics: Condensed Matter. vol. 19, no. 18, pp. 183201(1-41), May 2007.

35. N. Tombros, C. Jozsa, M. Popinciuc, H. T. Jonkman, B. J. van Weez, "Electronic Spin Transport and Spin Precession in Single Graphene Layers at Room Temperature," Nature, vol. 448, pp. 571-574, Aug. 2, 2007.

36. E. V. Castro, K. S. Novoselov, S. V. Morozov, N. M. Peres, J. M. Lopes dos Santos, J. Nilsson, F. Guinea, A. K. Geim, A. H. Castro Neto, "Biased Bilayer Graphene: Semiconductor with a Gap Tunable by the Electric Field Effect," Physical Review Letters, vol. 99, no. 21, pp. 216802(1-4), Nov. 23, 2007.

37. X. Li, X. Wang, L. Zhang, S. Lee, H. Dai, "Chemically Derived, Ultrasmooth Graphene Nanoribbon Semiconductors," Science, vol. 319, pp. 1229-1232, Feb. 29, 2008.

38. M. Y. Han, B. Ozyilmaz, Y. Zhang, P. Kim, "Energy Band-Gap Engineering of Graphene Nanoribbons," Physical Review Letters, vol. 98, no. 20, pp. 206805(1-4), May 18, 2007.

39. X. Liang, A. S. Chang, Y. Zhang, B. D. Harteneck, H. Choo, D. L. Olynick, S. Cabrini, “Electrostatic Force Assisted Exfoliation of Prepatterned Few-Layer Graphenes into Device Sites,” Nano Letters, vol. 9, no. 1, pp. 467-472, Jan. 14, 2009.

40. I. Forbeaux, J. M. Themlin, J. M. Debever, “Heteroepitaxial Graphite on 6H-SiC(0001): Interface Formation through Conduction-Band Electronic Structure,” Physical Review B, vol. 58, no. 24, pp. 16396-16406, Dec. 15, 1998.

41. U. Starke, C. Bram, P. R. Steiner, W. Hartner, L. Hammer, K. Heinz, K. Muller, “The (000l)-Surface of 6H-SiC: Morphology, Composition and Structure,” Applied Surface Science, vol. 89, no. 2, pp. 175-185, June 1995.

42. C. Berger, Z. Song, T. Li, X. Li, A. Y. Ogbazghi, R. Feng, Z. Dai, A. N. Marchenkov, E. H. Conrad, P. N. First, W. A. de Heer, “Ultrathin Epitaxial Graphite: 2D Electron Gas Properties and a Route Toward Graphene-Based Nanoelectronics,” Journal of Physical Chemistry B, vol. 108, no. 52, pp. 19912-19916, Dec. 30, 2004.

43. F. Varchon, R. Feng, J. Hass, X. Li, B. N. Nguyen, C. Naud, P. Mallet, J. Y. Veuillen, C. Berger, E. H. Conrad, L. Magaud, “Electronic Structure of Epitaxial Graphene Layers on SiC: Effect of the Substrate,” Physical Review Letters, vol. 99, no. 12, pp. 126805(1-4), Sept. 21, 2007.

44. S. Y. Zhou, G. H. Gweon, A. V. Fedorov, P. N. First, W. A. de Heer, D. H. Lee, F. Guinea, A. H. Castro Neto, A. Lanzara, “Substrate-Induced Bandgap Opening in Epitaxial Graphene,” Nature Materials, vol. 6, no. 10, pp. 770-775, Oct. 2007.

45. L. J. Cote, R. Cruz-Silva, J. Huang, “Flash Reduction and Patterning of Graphite Oxide and its Polymer Composites,” Journal of the American Chemical Society, vol. 131, no. 31, pp. 11027-11032, Aug. 12, 2009.

46. M. P. Levendorf, C. S. Ruiz-Vargas, S. Garg, J. Park, “Transfer-Free Batch Fabrication of Single Layer Graphene Transistors,” Nano Letters, vol. 9, no. 12, pp. 4479-4483, Dec. 9, 2009.

47. D. Eom, D. Prezzi, K. T. Rim, H. Zhou, M. Lefenfeld, S. Xiao, C. Nuckolls, M. S. Hybertsen, T. F. Heinz, G. W. Flynn, “Structure and Electronic Properties of

Graphene Nanoislands on Co(0001)," Nano Letters, vol. 9, no. 8, pp. 2844-2848, Aug. 12, 2009.

48. P. Sutter, M. S. Hybertsen, J. T. Sadowski, E. Sutter, "Electronic Structure of Few-Layer Epitaxial Graphene on Ru(0001)," Nano Letters, Vol. 9, no. 7, pp. 2654-2660, July 8, 2009.
49. A. Reina, S. Thiele, X. Jia, S. Bhaviripudi, M. S. Dresselhaus, J. A. Schaefer, J. Kong, "Growth of Large-Area Single- and Bi-Layer Graphene by Controlled Carbon Precipitation on Polycrystalline Ni Surfaces," Nano Reasearch, vol. 2, no. 6, pp. 509-516, June 2009.
50. D. V. Kosynkin, A. L. Higginbotham, A. Sinitskii, J. R. Lomeda, A. Dimiev, B. K. Price, J. M. Tour, "Longitudinal Unzipping of Carbon Nanotubes to form Graphene Nanoribbons," Nature, vol. 458, pp. 872-877, Apr. 16, 2009.
51. L. Jiao, L. Zhang, X. Wang, G. Diankov, H. Dai, "Narrow Graphene Nanoribbons from Carbon Nanotubes," Nature, vol. 458, pp. 877-880, Apr. 16, 2009.
52. G. Binnig, C. F. Quate, C. Gerber, "Atomic Force Microscope," Physical Review Letters, vol. 56, no. 9, pp. 930-933, Mar. 3, 1986.
53. G. Meyer, N. M. Amer, "Novel Optical Approach to Atomic Force Microscopy," Applied Physics Letters, vol. 53, no. 12, pp. 1045-1047, Sept. 19, 1988.
54. A.C. Ferrari, J. C. Meyer, V. Scardaci, C. Casiraghi, M. Lazzeri, F. Mauri, S. Piscanec, D. Jiang, K. S. Novoselov, S. Roth, A. K. Geim, "Raman Spectrum of Graphene and Graphene Layers," Physical Review Letters, vol. 97, no. 18, pp. 187401(1-4), Nov. 3, 2006.
55. L. M. Malard, M. A. Pimenta, G. Dresselhaus, M. S. Dresselhaus, "Raman Spectroscopy in Graphene," Physics Reports, vol. 473, no. 5-6, pp. 51-87, Apr. 2009.
56. D. Graf, F. Molitor, K. Ensslin, C. Stampfer, A. Jungen, C. Hierold, L. Wirtz, "Spatially Resolved Raman Spectroscopy of Single- and Few-Layer Graphene," Nano Letters, vol. 7, no. 2, pp. 238-242, Feb 2007.

57. J. Kedzierski, P. Hsu, A. Reina, J. Kong, P. Healey, P. Wyatt, C. Keast, "Graphene-on-Insulator Transistors Made Using C on Ni Chemical-Vapor Deposition," IEEE Electron Device Letters, vol. 30, no. 7, pp. 745-747, July 2009.

58. Wager, J. Class Notes. Semiconductor Devices II. Oregon State University, Corvallis, OR. Spring 2009.

59. M. Burghard, H. Klauk, K. Kern, "Carbon-Based Field-Effect Transistors for Nanoelectronics," Advanced Materials, vol. 21, no. 25-6, pp. 2586-2600, July 13, 2009.

60. F. Schedin, A. K. Geim, S. V. Morozov, E. W. Hill, P. Blake, M. I. Katsnelson, K. S. Novoselov, "Detection of Individual Gas Molecules Adsorbed on Graphene," Nature Materials, vol. 6, no. 9, pp. 652-655, Sept. 2007.

61. O. Leenaerts, B. Partoens, F. M. Peeters, "Adsorption of H_2O, NH_3, CO, NO_2, and NO on Graphene: A First-Principles Study," Physical Review B, vol. 77, no. 12, pp. 125416(1-6), Mar. 15, 2008.

62. W. H. Meiklejohn, C. P. Bean, "New Magnetic Anisotropy," Physical Review, vol.105, no. 3, pp. 904-913, Feb. 1957.

63. Y. Wang, X. Chen, Y. Zhong, F. Zhu, K. P. Loh, "Large Area, Continuous, Few-Layered Graphene as Anodes in Organic Photovoltaic Devices," Applied Physics Letters, vol. 95, no. 6, pp. 063302(1-3), Aug. 10, 2009.

64. S. M. Sze, K. K. Ng, Physics of Semiconductor Devices, 3rd ed., Hoboken, New Jersey: John Wiley and Sons, Inc., 2007.

65. G. B. Palmer, K. R. Poeppelmeier, T. O. Mason, "Conductivity and Transparency of ZnO/SnO_2-Cosubstituted In_2O_3," Chemistry of Materials, vol. 9, no. 12, pp. 3121-3126, Dec. 1997.

66. A. N. Banerjee, S. Kundoo, P. Saha, K. K. Chattopadhyay, "Synthesis and Characterization of Nano-Crystalline Fluorine-Doped Tin Oxide Thin Films by Sol-

Gel Method," Journal of Sol-Gel Science and Technology, vol. 28, no. 1, pp. 105-110, Aug. 2003.

67. M. D. Stoller, S. Park, Y. Zhu, J. An, R. S. Ruoff, "Graphene-Based Ultracapacitors," Nano Letters, vol. 8, no. 10, pp. 3498-3502, Oct. 8, 2008.
68. Y. Wang, Z. Shi, Y. Huang, Y. Ma, C. Wang, M. Chen, Y. Chen, "Supercapacitor Devices Based on Graphene Materials," Journal of Physical Chemistry, vol. 113, no. 30, pp. 13103-13107, July 30, 2009.
69. A. G. Pandolfo, A. F. Hollenkamp, "Carbon Properties and Their Role in Supercapacitors," Journal of Power Sources, vol. 157, no. 1, pp. 11-27, June 19, 2006.
70. J. S. Bunch, A. M. van der Zande, S. S. Verbridge, I. W. Frank, D. M. Tanenbaum, J. M. Parpia, H. G. Craighead, P. L. McEuen, "Electromechanical Resonators from Graphene Sheets," Science, vol. 315, pp. 490-493, Jan. 26, 2007.
71. L. Wang, K. Lee, Y. Sun, M. Lucking, Z. Chen, J. J. Zhao, S. B. Zhang, "Graphene Oxide as Ideal Substrate for Hydrogen Storage," ACS Nano, vol. 3, no. 10, pp. 2995-3000, Oct. 27, 2009.
72. S. Subrina, D. Kotchetkov, A. A. Balandin, "Heat Removal in Silicon-on-Insulator Integrated Circuits with Graphene Lateral Heat Spreaders," IEEE Electron Device Letters, vol. 30, no. 12, pp. 1281-1283, Dec 2009.
73. B. E. Deal, A. S. Grove, "General Realtionship for the Thermal Oxidation of Silicon," Journal of Applied Physics, vol. 36, no. 12, pp. 3770-3778, Dec. 1, 1965.
74. S. Wolf, R. N. Tauber, Silicon Processing for the VLSI Era (Volume 1 – Process Technology), 2nd ed., Sunset Beach, California: Lattice Press, 2000.
75. S. Ramo, J. R. Whinnery, T. V. Duzer, Fields and Waves in Communication Electronics, 3rd ed., Hoboken, New Jersey: John Wiley and Sons, Inc., 1994.
76. R. C. O'Handley, Modern Magnetic Materials - Principles and Applications, New York, New York: John Wiley and Sons, Inc., 2000.

APPENDIX A: Procedure for Synthesis of Graphite Oxide

Starting material: graphite powder (SP-1 grade 325 mesh)

- Pretreatment to fully oxidize graphite oxide (GO)
  - 50ml conc. H_2SO_4
    - 90C in 300mL beaker
    - add 10g $K_2S_2O_8$
    - add 10g P_2O_5
  - Stir until dissolved
  - Cool to 80 °C
  - Add 12g graphite
    - it will bubble should stop in <30 min
  - 80 °C for 4.5 hours
  - Stop heating
  - Dilute with 2L DI water
  - Leave overnight
- Filter and Wash
  - 0.2 micron nylon Millipore filter
  - DI water to remove acid traces
  - Dry in drying dish overnight in air
- Oxidation
  - 2L Erlenmeyer flask – may need to be bigger
    - 460mL H_2SO_4
    - 0 °C ice bath
    - add pretreated graphite and stir
    - slowly add 60g $KMnO_4$ keep below 10 °C
    - stir
  - 35 °C react 2 hours
  - Add 920ml distilled water
    - in 20-30mL aliquots to start
    - keep below 50 °C
  - Stir 2hr
  - Add 2.8L DI water
  - Add 50ml 30% H_2O_2
    - should be brilliant yellow and bubble
  - Settle for a day
  - Decant clear supernatant
  - Centrifuge remaining mixture
  - Wash
    - 5L 10% HCl
    - 5L DI water to remove acid
  - Dry in air
  - Dilute to a 2% w/w dispersion
  - 2 weeks dialysis
    - to remove remaining metal
  - Filter and dry to create "GO paper"
  - GO paper can be dispersed to single-layer platelets of desired concentration in DI by constant stirring for several weeks

Appendix B: Fabrication of Chrome Masks Using DWL

File Conversion:

1. Insert flash drive into USB port of computer above monitors, not the one on floor (Linux machine, connected to monitor on the left).
2. Click file-cabinet icon on bottom row (4th from left). "Dolphin" file manager opens.
3. Click "Volume" on left-hand side. Should now see contents of flash drive.
4. Find the file you wish to convert, right-click and copy
5. Click "Home" on left-hand side. Find the folder that corresponds to your design's filetype (GDSII, CIF, etc). Copy your file into this folder.
6. Close "Dolphin" and double-click the Gear icon to start conversion program
7. Click File → New Job. **Only 8 characters are allowed. Follow the agreed upon naming convention and update the spreadsheet/log book accordingly.**
8. Click the "Add" button, choose the correct data type and select your datafile.
9. Select the proper layer of your datafile, mirror, rotate, etc. then click "Create"
10. HIMT file gets created. Can click "Preview" to look at design
11. **Make sure that the write lens info corresponds to what's installed**. Also a good idea to take note of size of design (given in nm).
12. Good idea to click "Automatic Centering" to put (0,0) in design's geom center
13. Also **good idea to Mirror about the y-axis** (you flip the mask over when you use it), though not necessary for all designs
14. **Click "Expose Options" button and select Add 1 pixel**
15. Click "Complete Tasks" button. Save. When FTP transfer box pops up click "Transfer". Button will turn gray for a moment. When it returns to normal, your file has been transferred and you can close all open windows on the Linux machine.

Performing the Exposure:

1. Double-click the Happy Face icon (middle monitor) to open DWL66 software
2. **Make sure write-head info at top right corresponds to what is installed. Make sure IF:OK, and turn laser ON at least 3 minutes before write.**
3. Click Setup → New then "Create Map" (Use same name as job created on Linux machine). Click "Yes" to set environment to this job.
4. Click Setup → Exposure Map to determine number of fields and size (in microns). One design file can be written in each field.
5. Click Job → Make Job and the job spreadsheet appears.
   a. Enter "-1" in the "do" column if you want data written into the field.
   b. Click on "design" column, then go File → Designs (the File in the main menu, not the Edit Job menu). Click "Refresh" button to add most recently transferred file to list. Choose design to add to job spreadsheet.
   c. Enter appropriate values for Defoc and Energy (**values have been optimized for both 2mm - pneumatic and optical AF - and 10mm write head. See "exposure parameters" file on desktop**)
6. Save, and check on the top of the screen that the names of your .DWL, .MAP, and .FA files are all consistent.
7. Select optical or pneumatic autofocus (AF) by selecting from autofocus menu at top (optical AF cannot be used with 10mm write head)
8. Click Job → Run Job. A flowchart will appear
9. Click the "Load" button. The stage will come forward. Open the window

using the switch and position plate on the stage (PR side up) so that it is flush with the positioning pegs.

10. Turn on vacuum and check that vacuum area is set to size of plate.
11. Close window and click “OK” button on computer to move stage back to center. **Visually confirm that plate is under write-head.**
12. **Double-check that compressed air is available if pneumatic AF** (gauge on wall by door)
13. Click the “Focus” button. **Watch the z-value,** it should slow down and stop around 4735 (for 0.06” thick plates). **If it goes beyond 5000, hit cancel** or head can crash and be destroyed.
14. Click “Find Center” button. Box pops up when done, click “Yes”
15. If no further alignment is necessary, click “Expose” button

Post-Exposure Processing:

1. Fill glass dish (large enough to fit 4” square plate) with ~1/4” of PPD-455 developer from HTA Enterprises (Microchrome Technology). Fill a second dish with ~3/4” of 1MΩ de-ionized water.
2. Place exposed plate in **developer** (PR side up) and gently agitate for **~20 seconds**. Need enough developer to cover plate entirely.
3. Remove from developer and place in DI water to stop developing. Rinse with DI water and dry.
4. Empty developer to waste container, clean both dishes in sink room. Fill one dish with CEP-200 chrome etchant and the other with fresh 1 MΩ DI water.
5. Place plate in **etchant** for **~75 seconds**. Should be able to visually see when chrome clears (put white cloth/paper beneath dish and leave in acid until no “cloudiness” in mask).
6. Remove from acid and place in DI water to stop etching. Rinse with DI water and dry.
7. Neutralize acid and pour into waste container, clean both dishes in sink room. Fill one dish with PRS-100 photoresist stripper.
8. Place plate in resist **stripper** for **~2 minutes**, gently agitating. Rinse with DI water and dry.
9. Inspect under microscope. Photoresist may stick to small features. Chrome should be orange in color. PR will be red and appear scaly. If PR remains, put back in stripper and **gently rub surface of mask with cleanroom wipe**.
10. Dispose of resist stripper in waste container. Wash dish.

Note:

Mask blanks for this project were purchased from the Nanofilm Company. They are 4"x4"x0.06" and consist of chrome on soda lime with a 5300Å layer of AZ1518 photoresist.

Appendix C: Operational Procedure for Thermal Evaporator

Loading the Chamber:

1. The tool requires that the cold-trap be filled with liquid N2. Take a dewar from the lab to the Chem-Stores and fill from tank. Empty into funnel at rear of tool.
2. Tool should be in "idle" state: hi-vac valve closed, roughing valve closed, foreline valve open. Slowly open vent valve, **keeping an eye on foreline pressure gauge** (if it spikes, close vent valve and make sure hi-vac valve is closed all the way). If foreline pressure is solid, open N_2 tank to hasten vent process.
3. Continue vent until chamber reaches atmospheric pressure (you will hear the chamber "pop"). Raise bell jar using hoist (toggle switch on front panel up)
4. Remove shielding and load substrates and deposition materials.
    a. Substrates are affixed to a metal plate (using Kapton tape) and hung face-down at the top of the chamber.
    b. There are four electrodes at the bottom of the chamber (forming a triangle with one in the center). The center electrode is common, and current through the other three can be independently controlled at the front panel of the tool. Tungsten boats containing deposition materials are placed between electrodes appropriately.
5. **Ensure that shutter is operating correctly**. Shutter is controlled by box with toggle switch located to the right of the chamber. It is a 3-position switch and should normally be in the center position. To close shutter: click down once, then back to center. To open: click up once, then back to center. Shutter is actuated by applying current to one of two coils, creating a magnetic field which attracts a magnet attached to the shutter itself. If shutter is not working:
    a. Make sure magnets not stuck to the metal shielding
    b. Adjust the orientation of the wire coils

`

6. Put shutter in closed position (covering sample), replace shielding and use hoist toggle-switch to lower bell jar until it seats properly (**do not hit or pinch gasket** on any edges on the way down).

Chamber Evacuation:

1. **Close foreline valve** (clockwise is closed for all valves)
2. Slowly open roughing valve **keeping an eye on the foreline pressure**. Chamber pressure should start to fall, but if foreline pressure gets above 100 mTorr close the roughing valve and open the foreline valve (the **roughing and foreline valves should never be open at the same time**).
3. When the chamber pressure reaches $5*10^{-2}$ Torr, **close the roughing valve and open the foreline valve**. Slowly open the hi-vac valve **keeping an eye on the foreline pressure**. When the foreline exceeds 100 mTorr, close hi-vac valve and allow pressure to drop. You will eventually be able to open hi-vac valve all the way and the pressure gauge will bottom out at 1*10-4 Torr.
4. **Wait five minutes** and turn on the ion gauge:
    a. Press "CHAN" button on gauge controller four times to cycle through channels to the channel for the ion gauge. The display should say "OFF".
    b. Pres the "EMIS" button once to turn on the gauge. The chamber pressure will be displayed. Wait until desired pressure is reached.

Deposition:

1. Once desired pressure attained **turn off ion gauge** (press “EMIS” button)
2. Enter the values of density and acoustic impedance for your deposition material into rate monitor located on the top shelf of an equipment rack to the right of the evaporator:
    a. Press “ENTER” twice to get to the main menu.
    b. Use arrow buttons to select quantities and enter values using numeric keypad.
    c. Press “ENTER” after typing each value and press “ENTER” twice when finished.
3. Turn on breaker switch to electrode connected to boat containing material for first depositon. (note: **cooling water** should always be on, but check flow gauge by window) The power supplies are located at the bottom left of the front panel. The supply on the left powers the front electrode, the middle supply powers the rear left electrode, and the rightmost supply powers the rear right electrode (note: INT/EXT switch should be set to INT)
4. Slowly increase power to the electrode (about 10V every 30 seconds) keeping an eye on the rate monitor. When the desired rate is reached, open the shutter and zero the monitor (press the “ZERO” button. When desired thickness is achieved, close the shutter. Slowly ramp the power back down and turn off breaker switch.
5. Repeat for other materials if multiple layers are deposited.

Sample Removal:

1. After deposition, **close the hi-vac valve**. Tool is now in the “idle” state.
2. Slowly open vent valve, **keeping an eye on foreline pressure gauge** (if it spikes, close vent valve and make sure hi-vac valve is closed all the way). If foreline pressure is solid, open N_2 tank to hasten vent process.
3. Continue vent until chamber reaches atmospheric pressure (you will hear the chamber “pop”). Raise bell jar using hoist (toggle switch on front panel up)
4. Remove shielding, samples, and deposition materials

Leaving Machine:

1. Lower bell jar until it seats properly (**do not hit or pinch gasket** on any edges on the way down).
2. **Close foreline valve**
3. Slowly open roughing valve **keeping an eye on the foreline pressure**. Chamber pressure should start to fall, but if foreline pressure gets above 100 mTorr close the roughing valve and open the foreline valve.
4. When the chamber pressure reaches $5*10^{-2}$ Torr, **close the roughing valve and open the foreline valve**. This is the “stand-by” condition. The tool can now be walked away from.

Appendix D: Operational Procedure for Sputter Tool

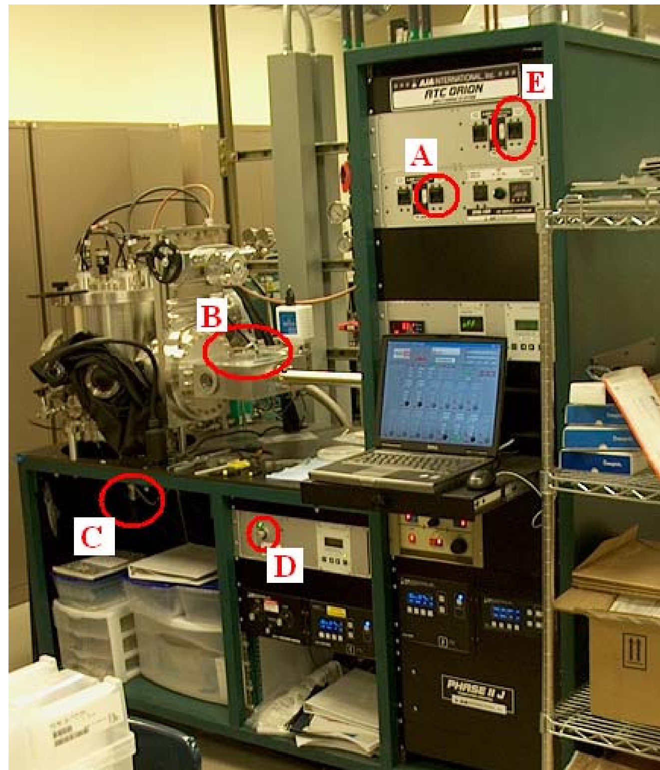

Figure 60. AJA ATC Orion Sputter System

Loading the Chamber:

1. To load the chamber, the load lock first has to be brought up to atmospheric pressure. This is done by closing the valve to the load lock pump and venting (using the switch marked A in figure 67).
2. Remove the lid to the load lock (B) and place samples inside the load lock chamber on the sample platform. A can of compressed air can be used to remove dust from sample just before placing into load lock. Replace the lid and re-establish vacuum in the load lock using switch (A).
3. **Wait until the pressure in the load lock reaches 5*10-5 Torr**. Open the isolation valve between the load lock and main chamber by turning the black wheel directly above the load lock.
4. Slide the sample into the main chamber using the magnetic translator (located behind the laptop screen in Figure 67).
5. Use the sample height adjustment knob (C) to raise the sample stage, lifting the sample platform off of the forks that are supporting it. **Watch through the view port making use of the desk lamp as you are doing this. Be careful not to raise the sample stage too high, bending the forks.**
6. Use the magnetic translator to retract the forks out from under the sample platform (now held suspended by the sample stage) and into the load lock.
7. Turn the black wheel to close the isolation valve**. Make sure it is closed all the way. You will hear it click as you continue to turn wheel after it is closed.**
8. The desired sample height can now be adjusted, as can substrate rotation using knob (D).

Chamber Evacuation:

1. At this point, the chamber should be evacuated to at least $5*10^{-5}$ Torr (otherwise it should not have been loaded with a sample). The chamber will continue to pump to $10^{-7} – 10^{-8}$ Torr if one were to wait several days.
2. The only reason to bring the chamber up to atmospheric pressure (other than maintenance) is to change targets. In this case, the switch marked (E) in Figure 67 is used to turn the main chamber pumps on and off.

Changing Targets:

1. To change a sputter target, first bring the chamber to atmospheric pressure then open the lid to the main chamber by unscrewing the black handle and lifting. **Be careful not to pinch any wires or hoses.**
2. Loosen and remove the two large hex screws holding the ground shield assembly in place. The shutter will hang freely from the spring rod actuator and the ground shield can be removed and set aside. It should be pointed out that the tool has four cathodes, each capable of holding a sputter target. In Figure 68, the bottom left cathode is for magnetic 2” targets, the top right cathode can be given an RF bias and is for insulating 3” targets, and the other two cathodes are given DC biases and are for conducting 3” targets.
3. Loosen and remove the four smaller hex screws holding the target clamping ring into place over the target. Remove the target along with clamping ring (and spacer ring and copper mesh if used). **Note that if the target is magnetic, it will be difficult to remove due to the attraction to the magnetron ring. Use the clamping ring to push the target to the edge of the cathode block. Push with your thumbs and use your fingers to support the cathode block.**
4. Center new target on cathode block and replace clamping ring and four hex screws. **Be sure to place a piece of copper mesh between the target and cathode block if necessary to help with heat transfer. If target is less than 0.25” thick, be sure to include an appropriately-sized spacer ring between the target and clamping ring to bring the total thickness to 0.25”.**
5. Replace the ground shield, hold shutter in place, and thread the two larger hex screws through both the shutter and ground shield and tighten.
6. Open the shutter (by clicking a green circular button on computer control program which will turn bright green when shutter is open). **Use an ohmmeter to ensure an open circuit between the target and the ground shield (or at least a resistance of a few MΩ)**. Close shutter.
7. Initiate pumping of main chamber using switch (E).

Deposition:

1. Deposition is initiated by clicking a button on the computer interface. Prior to deposition, a variety of parameters can be set. These include power, duration, substrate temperature, gas flow (which affects the operating pressure of processing gasses such as argon), ramp rates, and delays. The user can even automate recipes (say for depositing multilayer structures). Rates for different materials can be estimated using the tables at the end of this appendix
2. **It is important to ramp the power for 30 seconds for every 50 W of power in order to avoid thermal stress which could result in target cracking.**

3. Setting argon flow to 20 sccm (the maximum possible) and setting the high vacuum valve to the throttle position results in a chamber pressure of 3-4 mTorr which has been found to be adequate for striking a plasma in all cathodes except the RF cathode which has not been used by the author.
4. It is a good idea to visually confirm through the view port that a plasma exists and that the shutter opens, but one should quickly **close the shutter that covers the view port so that deposition material does not coat the glass**. This would render the view port useless and it would have to be removed and the material etched away to restore the transparency of the window.

Figure 61. AJA sputter tool with main chamber open

Sample Removal:

1. After a plasma has been struck and the shutter opened for the programmed length of time, the shutter will close and the high vacuum valve separating the main chamber from the turbo pump will open from its throttle position, evacuating the chamber of processing gasses.
2. **Make sure that the pressure in the load lock is less than $5*10^{-5}$**, then open the isolation valve between the load lock and the main chamber.
3. Turn off substrate rotation if on and **adjust the sample height to 43"** which is the required height for the forks to slide in properly.
4. Use the magnetic translator to slide the forks into the main chamber and under the sample platform**. Slide the forks in slowly and watch through the view port to be sure that the forks do not crash into anything.**
5. Use the sample height adjustment knob (C) to lower the sample stage, allowing the sample platform to rest on the forks.
6. Use the magnetic translator to slide the sample platform out of the main chamber and into the load lock.
7. **Close the isolation valve by turning black wheel. Make sure it is closed all the way. Hear it click.**
8. Bring load lock up to atmospheric pressure by using switch (A). Remove load lock lid and take samples out of load lock. Replace load lock lid and re-establish vacuum in the load lock by using switch (A) again.

Leaving Machine:

1. Once the sample has been retrieved from the load lock and vacuum is established both in the load lock and the main chamber, the system can be walked away from.
2. **Double check to make sure that substrate rotation is turned off as is the desk lamp**

Power (%)	Time (sec)	Thickness (Å)*	Rate (Å/sec)
5	600	330±47	**0.55±0.08**
8	600	600±64	**1.00±0.11**
10	600	824±44	**1.37±0.07**
13	600	1031±15	**1.72±0.03**
15	600	1241±30	**2.07±0.05**
20	600	1576±28	**2.62±0.05**
25	600	2137±81	**3.56±0.14**
30	600	2573±58	**4.29±0.10**

* Thickness measured by profilometer, Ar pressure ~4mTorr, height=43, temperature=OFF, rotation=50

Table 6. Experimental sputter rates for copper target in 3" DC cathode

SPUTTER YIELD RATES (~DEPOSITION RATES) RELATIVE TO COPPER

Al	0.77	Ge	1.10	Sb	3.96
Al2O3	0.16	Ir	0.66	Si	0.38
Ag	2.24	Mo	0.51	SiC	0.39
Au	1.90	Mn	1.07	SiO2	0.49
Be	0.19	Nb	0.48	Sm	1.21
Bi	1.76	Ni	0.70	Su	1.41
C	0.05	Os	0.54	Ta	0.46
Co	0.62	Pb	3.76	Th	0.90
Cr	0.65	Pd	1.41	Ti	0.41
Cu	1.00	Pt	0.97	U	0.81
Dy	1.27	Rb	4.89	V	0.41
Er	1.08	Re	0.57	W	0.42
Fe	0.52	Rh	0.97	Y	1.023
GaAs	1.83	Ru	0.71	Zr	0.70

NOTE: The comparative rates shown above indicate the efficiency with which these materials will be sputtered relative to Copper when bombarded by Argon ions under perfect conditions. They do not consider factors such as temperature limitations of the target material, native oxides which may form on target material surfaces, shunting of magnetic field lines by magnetic material targets, etc. and should be used accordingly.

Table 7. Sputter rates for materials relative to copper (from AJA manual)

Material	Power (%)	Time (sec)	Thickness (Å)	Rate (Å/sec)
CoFe	**10**	600	190±40	**0.32±0.06**
CoFe	**15**	600	370±30	**0.62±0.05**
CoFe	**20**	600	430±40	**0.72±0.06**
CoFe	**25**	600	500±40	**0.83±0.06**
CoFe	**30**	600	530±50	**0.88±0.08**
CoFe	**35**	600	600±30	**1.00±0.05**
CoFe	**40**	600	700±50	**1.17±0.08**
CoFe	**45**	600	710±20	**1.18±0.03**
NiFe	**20**	600	440±55*	**0.73±0.09**
NiFe	**25**	600	531±46	**0.89±0.08**
NiFe	**30**	600	708±27	**1.18±0.05**
NiFe	**35**	600	796±23	**1.33±0.04**
NiFe	**40**	600	894±43	**1.49±0.07**

Table 8. Experimental sputter rates for magnetic targets in 2” DC cathode